Advances in Magnetics

A Closer Look Into Magnetism: Opportunities With Synchrotron Radiation

Hermann A. Dürr[1], Thomas Eimüller[2], Hans-Joachim Elmers[3], Stefan Eisebitt[1], Michael Farle[4], Wolfgang Kuch[5], Frank Matthes[6], Michael Martins[7], Hans-Christoph Mertins[8], Peter M. Oppeneer[9], Lukasz Plucinski[6], Claus M. Schneider[6], Heiko Wende[4], Wilfried Wurth[7], and Hartmut Zabel[2]

[1]BESSY GmbH, Berlin, Germany
[2]Ruhr-Universität Bochum, Germany
[3]Inst. f. Physik, Universität Mainz, Mainz, Germany
[4]Fachbereich Physik and Center of Nanointegration, Universität Duisburg-Essen, Germany
[5]Inst. f. Experimentalphysik, Freie Universität Berlin, Germany
[6]Inst. f. Festkörperforschung IFF-9, Forschungszentrum Jülich, D-52425 Jülich, Germany
[7]Universität Hamburg, Hamburg, Germany
[8]Fachhochschule Münster, Münster, Germany
[9]Physics Department, Uppsala University, Sweden

The unique properties of synchrotron radiation, such as broad energy spectrum, variable light polarization, and flexible time structure, have made it an enormously powerful tool in the study of magnetic phenomena and materials. The refinement of experimental techniques has led to many new research opportunities, keeping up with the challenges put up by modern magnetism research. In this contribution, we review some of the recent developments in the application of synchrotron radiation and particularly soft X-rays to current problems in magnetism, and we discuss future perspectives.

Index Terms—**Antiferromagnetic materials, anisotropy, biomolecules, coplanar transmission lines, electron storage rings, ferrimagnets, ferromagnetic thin films, Heusler alloys, magnetic domains, magnetic clusters, magnetic imaging, magnetic molecules, magnetic moments, magnetization dynamics, photoemission spectroscopy, PEEM, resonant magnetic scattering, spin dynamics, spin polarization, sum rules, synchrotron radiation, X-ray absorption spectroscopy, X-ray holography, X-ray microscopy, X-ray magnetic dichroism, X-ray scattering, X-ray magnetooptics.**

I. Introduction

THE interaction between polarized light and magnetically ordered systems was first noted more than 150 years ago by Michael Faraday (1846) [1]. In terms of their magnitude, the magneto-optical Faraday and Kerr rotations observed in the visible range of the electromagnetic spectrum may be examples for relatively subtle effects. Nevertheless, these magneto-optical phenomena are widely employed nowadays, often using laser illumination. On the one hand, magneto-optical spectroscopy and microscopy have become invaluable tools in the study of both magnetostatic and magnetodynamic issues [2], [3]. On the other hand, they also form the physical basis for the magneto-optical branch in high-density digital storage and audio recording technology [4].

The light generated in synchrotron radiation facilities has a very broad energy spectrum ranging from the infrared up to hard X-rays. This opens many opportunities to study magnetism with excitation energies beyond the visible range. Following up spin-polarized photoemission studies with laboratory sources in the 1970s [5], probably the first spin- and momentum-resolved photoemission studies using synchrotron radiation were carried out on nickel [6], initiating a development that tremendously progressed our understanding of the electronic origin of magnetism. In this type of experiment, photoelectrons from the valence electronic states are excited by photons of about 50–100 eV energy, their spin-polarization revealing clear information about the majority and minority spin states and the magnitude of the exchange splitting of these states. Involving sophisticated electron spin detection schemes, however, these spin-polarized approaches still remain a topic for a specialist community only.

A major breakthrough in the application of synchrotron radiation to magnetism was achieved at the end of the 1980s by the theoretical prediction and experimental discovery of magnetic linear (XMLD) and circular dichroism (XMCD) in X-ray absorption [7]–[10]. This discovery marks a transition in a twofold sense. First, the magnetic state from a sample could now be deduced on the basis of simple measurements of an intensity signal, rather than an elaborate spin polarization analysis. Second, the resonant character of the X-ray excitation linked the magnetism to individual elements or specific chemical states. In a way, XMCD and XMLD may be seen as the high-energy counterparts to the original magneto-optical effects discovered by Faraday and Kerr.

In the wake of the discovery of X-ray magnetic dichroism, soon a wealth of refined and novel experimental and theoretical

Manuscript received June 09, 2008; revised September 19, 2008. Current version published January 30, 2009. Corresponding author: C. M. Schneider (e-mail: c.m.schneider@fz-juelich.de).

Color versions of one or more of the figures in this paper are available online at http://ieeexplore.ieee.org.

Digital Object Identifier 10.1109/TMAG.2008.2006667

approaches unfolded. Milestones mark magnetic dichroism in the angular distribution of photoelectrons (MDAD) in the soft X-ray and vacuum ultraviolet region [11]–[13], magnetodichroic electron and X-ray microscopies [14]–[16], X-ray resonant magnetic scattering (XRMS) [17], nuclear resonant magnetic scattering (NRS) [18]–[20], and magnetodichroic X-ray holography [21]. Most of these techniques have already become "work horses" in the current experimental investigations of modern magnetic materials and magnetism on the nanoscale.

In the following, we will review some recent developments in this field, which have become possible by the improvement in quality and availability of synchrotron radiation. The remainder of this paper is organized as follows. In the second section, we will briefly comment on the challenges in magnetism, which motivate the use of synchrotron radiation in studies of magnetic systems. The third part reviews the general principles of the generation and the salient features of synchrotron radiation. In the fourth section, we discuss applications of synchrotron radiation to recent problems in magnetism. As a full account of these applications will go beyond the scope of this review, we limit ourselves to a selection of the most prominent applications and effects. The final section is devoted to some future perspectives.

II. Challenges in Magnetism

In order to work out the application potential of synchrotron radiation in the study of magnetic systems, it is useful to briefly sketch the current challenges in magnetism. Magnetism is characterized by an interplay of interactions on very different length scales. This interaction also gives rise to magnetic structures on different length scales ranging from magnetic domains in the 100 μm regime down to noncollinear spin structures on the nanometer scale such as vortex cores. Recent years have seen a trend towards smaller and smaller magnetic structures stimulating the interest in the magnetic properties of quantum wires and quantum dots, clusters, molecules, or even single atoms arranged on a template. Major issues are, for example, the role of the dimensionality in the existence and type of long-range magnetic order and the impact of geometrical boundary conditions on the formation of specific spin structures. With respect to the electronic structure, the interplay of exchange interactions—particularly in chemically diverse systems—and the resulting spin and orbital magnetic moments as well as the magnetic anisotropies are of very fundamental interest for our microscopic understanding of magnetism.

The second major topic in magnetism concerns the *time scale*, which may range from data retention times of 10 years down to exchange dominated excitation processes in the femtosecond regime. At present, great interest is devoted to dynamic processes taking place on short and ultrashort time scales. They are intimately connected to the question how fast a given magnetic system can be reversed. In order to explore this limit it is mandatory to understand the microscopic processes governing energy and angular momentum transfer. Presently, a magnetization reversal can be achieved by external (Oersted) fields, by spin-polarized currents, and also by illumination with ultrashort laser pulses. Each mechanism creates specific excitations in the magnetic system. These range from precessional motion and spin waves on the fast (picosecond) scale to electron-hole pairs and Stoner excitations in the ultrafast (femtosecond) regime.

A third driving force in magnetism is the field of spintronics, i.e., the understanding and exploitation of spin-dependent transport processes. In addition to the aspects of short length and time scales, spintronics introduces also the issue of chemical complexity, caused by an extremely broad materials basis. The systems explored in the search for new spin-dependent functionalities range from simple ferromagnets to ternary metallic compounds, from silicon to dilute magnetic semiconductors, and from binary transition metal oxides to perovskites. Disentangling the complicated interplay of electronic interactions in these materials is a first step towards understanding their magnetic behavior and the role of the individual constituents for spin-dependent coupling and transport effects. On the one hand, spintronics is also considered to pave a way to solid-state based quantum information processing. Therefore, molecular systems, such as endohedral fullerenes or molecular magnets, are also extensively investigated. On the other hand, spintronics and magnetism may find soon applications in biology and medicine for diagnostic and therapeutic purposes, which also brings biological and magnetic systems closer together.

Addressing the various challenges associated with small length scales, short time scales, and chemical diversity in magnetism asks for a refined set of experimental approaches, which must be able to yield detailed information on the interactions, magnetic moments, or excitations. The use of synchrotron radiation is conveniently providing these approaches, as we will discuss in the remainder of this review.

III. Synchrotron Radiation

A. General Properties

An electrically charged particle in motion which undergoes an acceleration will dissipate energy via electromagnetic waves, according to the fundamental laws of electrodynamics. As long as the motion takes place at a velocity v significantly lower than the speed of light c, the radiation pattern follows a dipolar characteristics ("doughnut"-shape) with the maximum power emitted perpendicular to the direction of acceleration. This angular dependence changes significantly, when the charge moves at relativistic speed, i.e., $v \approx c$. The Lorentz transformation between the moving reference frame of the charge and the rest of the system changes the emission characteristics from a dipole into a very narrow emission cone perpendicular to the acceleration vector and along the velocity vector. In a synchrotron the electron or positron is revolving on a circular orbit, i.e., the charge is subject to a radial acceleration and the emission of the (synchrotron) radiation is confined to the forward tangential direction.

The properties of this radiation can be quantitatively calculated on the basis of the Lippmann-Schwinger equation. The light is emitted as a continuous spectrum up to a so-called "cut-off" frequency ω_c, which is determined by the maximum kinetic energy E_e of the orbiting charge. If one assumes the electron moving on a circular orbit due to a magnetic field B in a so-called bending magnet, the "cut-off" or critical frequency becomes [22]

$$E_c = \hbar\omega_c = \frac{3e\hbar B\gamma^2}{2m} \tag{1}$$

with $\gamma = E_e/(mc^2)$. This means for some realistic value of the magnetic field $B = 1.3$ T in a bending magnet and a kinetic energy of $E_e = 2$ GeV the cut-off energy takes a value of $E_c = 3460$ eV. Thus, the photon energies provided by this bending magnet radiation reach already far into the X-ray regime.

Due to the relativistic motion of the electron, the photons are emitted into a narrow angle $\theta = 1/\gamma$ in the forward direction. For the conditions chosen above, the emission angle is less than 1 mrad. As a consequence, the photon flux emitted from a bending or dipole magnet into this cone is very high, typically more than 10^{10} s^{-1} for an energy interval or bandpass of $\Delta\omega/\omega = 0.1\%$.

A quantity which is very useful to compare the properties of different synchrotron sources is the brightness $\mathcal{B}$, which denotes the photon flux P from a unit source area ΔA into a unit solid angle $\Delta\theta$, i.e.,

$$\mathcal{B} = \frac{P}{\Delta A \cdot \Delta\theta}. \tag{2}$$

If $\mathcal{B}$ is taken only for a limited bandwidth $\Delta\lambda/\lambda$ of the radiation (usually $\Delta\lambda/\lambda$ is set to 0.1%), one obtains the spectral brightness or brilliance $\mathcal{B}_\lambda$. Note that with these definitions both $\mathcal{B}$ and $\mathcal{B}_\lambda$ increase when reducing ΔA and $\Delta\theta$, which becomes important when discussing insertion devices (see Section III-B).

As a further feature the radiation has a well-defined polarization characteristics. The light emitted within the orbital plane is fully linearly polarized, with the electric field vector $\vec{E}$ oriented parallel to the orbital plane. The light emitted off-plane, however, has in general an elliptical polarization. By choosing the appropriate emission angle, a degree of circularity may be achieved as high as 90%. By accepting the radiation above or below the orbital plane, one may conveniently switch the direction of the circularity [23].

The acceleration of the electrons and the compensation of the radiative energy loss in the storage ring is achieved by microwaves. The coupling of the electrons with the microwaves naturally leads to a temporal pattering into electron "bunches." As a consequence, synchrotron radiation has a well-defined time structure, consisting of sharp light pulses with typical widths of a few picoseconds to several 10 ps, depending on the operation mode of the synchrotron. The separation Δt of the individual pulses can be very conveniently chosen by the filling pattern of the storage ring and ranges from a few nanoseconds up to almost a microsecond.

The quantity coherence measures the phase alignment of the light's electric field vectors. Transverse or spatial coherence describes the degree to which the waves are in phase across a light beam at any instant. If one considers a source of extension d which emits light into an angle θ, the transverse coherence depends on the wavelength λ as [24]

$$d \cdot \theta = \lambda/\pi. \tag{3}$$

Therefore, with a proper collimation and energy filtering even an incoherent source can supply partially coherent radiation, which is well-known in conventional light optics. The longitudinal or temporal coherence describes the degree to which the phase relations between the waves are preserved as the light propagates. The transverse coherence length ℓ_c of a synchrotron radiation beam is given by the wavelength and the bandwidth as [24]

$$\ell_c = (\lambda/2) \cdot (\lambda/\Delta\lambda). \tag{4}$$

with the coherent spectral flux $\mathcal{F}_c$

$$\mathcal{F}_c = \mathcal{B}_\lambda \cdot (\lambda/2)^2 \tag{5}$$

being directly proportional to the brilliance. In other words, a reduction of source size and emittance angle increases the coherence of the radiation. These relationships are the keys to understand the coherence characteristics of the various synchrotron sources.

In summary, synchrotron radiation provides a unique combination of

i) wide-range tunability,
ii) high brightness,
iii) variable polarization,
iv) well-defined time structure,
v) high degree of coherence.

B. Synchrotron Light Sources

In the beginning, synchrotron radiation was provided as a parasitic effect in high-energy experiments. The first dedicated synchrotron light sources—the so-called second generation—became available at the beginning of the 1970s. In these sources, the light was mostly generated in bending magnets, as described above.

A much higher brilliance of the radiation can be achieved by means of magnetic insertion devices of the wiggler or undulator type, which are placed in a straight section of the storage ring in between the bending magnets. These insertion devices are periodic magnetic structures, in which the electrons are forced on trajectories with multiple bends. The emission of the light at the individual bends may superimpose along the forward direction incoherently (wiggler) or coherently (undulator), causing a very high photon flux in a narrow energy window $\Delta\lambda/\lambda$ (harmonic) in the latter case. In addition, also the opening of the emission cone shrinks to $\theta = 1/(\gamma\sqrt{N})$ with N being the number of periods in the undulator. The first 3rd generation light sources, making extensive use of these insertion devices went into operation in the middle of the 1990s and represent the current standard. A simple planar undulator, in which the electrons undulate only in one plane produces linearly polarized light, with the electric field vector E_x lying in this plane. With more sophisticated magnet designs as realized, for example, in elliptical undulators the light polarization can be almost continuously varied between orthogonal linear (E_x, E_y) and opposite circular states $E_{\sigma+}$ and $E_{\sigma-}$ (Fig. 1). The efficient use of undulators requires a very narrow (typically of the order of 10 μm) and stable electron beam. As an added value, the source spot of the light emission becomes very small, too. In combination with the small angular spread of the radiation also the transverse and longitudinal degree of coherence increases, as can be easily derived on the basis of (4), (5). With some additional spatial filtering through pinholes, the degree of coherence becomes large enough to allow

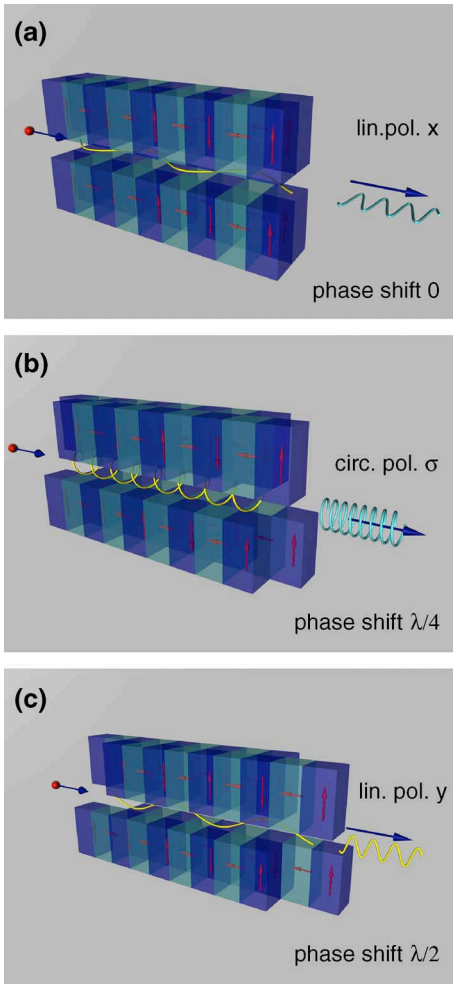

Fig. 1. Functional principle of an elliptical undulator. By shifting the magnet benches with respect to each other, the electrons are forced on different undulating trajectories, thereby providing synchrotron radiation of linear (a), (c) and circular (b) polarization states.

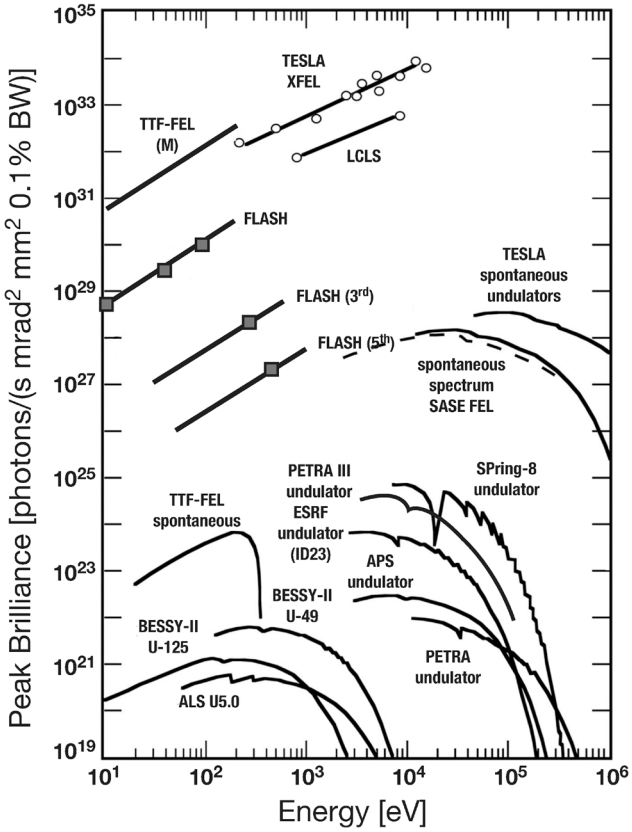

Fig. 2. Calculated peak brilliance of the synchrotron radiation provided by different insertion devices at the 3rd generation storage ring facilities ALS (Berkeley), APS (Argonne), BESSY-II (Berlin), ESRF (Grenoble), SPring-8 (Tsukuba), PETRA-III (Hamburg). For comparison, also the expected values for the existing and future free-electron laser sources FLASH and XFEL (both Hamburg), and LCLS (Stanford) are given. Experimental values for FLASH for the first, third and fifth harmonic are indicated by squares.

for first experiments making use of this property, even for applications in magnetism [21].

A further increase of the peak brilliance and the coherence of the synchrotron radiation is expected from the free-electron lasers (FEL) sources. In contrast to the storage ring concept, a free-electron laser comprises in most cases a linear accelerator, which feeds the electron beam into a dedicated undulator. During the passage of the electrons through the undulator, the electrons emit radiation, which travels together with the electron bunches and strongly interacts with them. This interaction leads to a further substructuring of the bunches into "micro-bunches" with a well-defined phase relation. As a result, these micro-bunches emit intense radiation of less than 100 fs pulse width [25], [26]. Taking into account the different time structure of storage ring and FEL radiation, the *peak brilliance* (brilliance normalized to the photon pulse width) increases between four and eight orders of magnitude in the latter device (Fig. 2). In addition, the phase relation leads to a high coherence of the radiation. The stochastic nature of the emission process can be partially avoided by additionally coupling a strong ultrashort laser pulse into the undulator ("seeding"), which interacts with the electrons, thereby stimulating the light emission. First experiments at FEL's are now becoming possible, and will soon also be addressing problems in magnetism.

IV. Spectroscopy of Magnetic Systems

The electronic structure and particularly the interaction of electronic states in a material system is at the very heart of magnetism. In order to characterize the relation between the electronic structure and magnetism—specifically in modern magnetic materials—various spectroscopic approaches are involved. By addressing the valence electronic states much can be learned about the electronic bonds and interactions between neighboring atoms. Investigating the more localized core levels with soft X-rays yields information about the magnitude and orientation of the magnetic moments on an element-selective basis. On the other hand, the detection scheme provides convenient access to the surface or bulk aspects of magnetism. Whereas the detection of photoelectrons or the total electron yield is usually quite surface sensitive, a photon-in/photon-out scheme as in absorption or reflection experiments allows for a higher bulk sensitivity.

A. Spin-Resolved Valence Electronic States

The electronic and magnetic functionality of a layer stack in spintronics is mostly determined by the interfaces. This is particularly true in spin-dependent tunneling through an insulating

barrier, as the spin-polarization and symmetry of the electronic states at the ferromagnet/insulator interface have a crucial influence on the spin scattering during the transport process. In this context, the valence band structure at the interface of the single crystalline system MgO(001)/Fe(001) has moved into the focus of current research in spintronics, because it evidently dictates the performance of state-of-the-art magnetic tunneling junctions (MTJs). Today, MTJs based on single crystalline Fe/MgO or Co/MgO systems provide the highest achievable tunneling magneto-resistance (TMR) ratios [27], [28]. The progress compared to amorphous MTJs is related to a symmetry-related attenuation of the electronic wave functions contributing to the tunneling process. For the Fe(001)/MgO(001)/Fe(001) system along the Δ-direction, wave functions with Δ_1 spatial symmetry suffer the lowest attenuation, compared to the wave functions with Δ_2, $\Delta_{2'}$ and Δ_5 spatial symmetry. Due to the particular band matching at the Fermi level in these MTJ structures, this symmetry dependence can be converted into a spin-controlled functionality. When iron is utilized as an electrode, a spin-dependent conductivity can be established, because only the majority spin character $(\uparrow)$ for wave functions with Δ_1 symmetry is accessible at the Fermi level. Thus, for an antiparallel magnetic alignment of the two iron electrodes, tunneling electrons linked to the Δ_1 wave functions will be reflected at the counter iron electrode, resulting in a much higher resistance than the one obtained in the parallel orientation of the two magnetic electrodes. These findings were theoretically predicted by Butler and Mathon [29], [30] who assumed an idealistic situation of a chemical non-interacting Fe/MgO interface that is atomically sharp and well-ordered. Obviously, in a realistic system the interface properties will deviate from this assumptions, evoked e.g. by structural disorder or electronic interaction at the interface. It is thus not surprising, that the first experimental studies showed drastically reduced TMR ratios compared to theory [31]–[33], and the results achieved initiated vivid discussions about the influence of the interfacial morphology and bonding conditions.

Valence band photoelectron spectroscopy is a powerful tool to study the electronic structure in a symmetry- and wave vector-resolved manner. In a spin-resolved version, it is ideally suited to address the electronic and magnetic states at heteromagnetic interfaces. Recently, detailed spin-polarized valence band photoemission spectroscopy experiments were performed to clarify the modifications in the electronic band structure of MgO/Fe(001) introduced by different interfacial stoichiometries [34]. For this purpose, three different samples classes were prepared representing a stoichiometric, under-oxidized and over-oxidized interface. Special emphasis was laid onto the chemical characterization of the MgO/Fe interface. Besides Auger electron spectroscopy, the degree of Mg and Fe oxidation was supervised by probing the chemical induced shifts of the Mg 2p and Fe 3p core levels, thereby using a low photon energy of 88.3 eV to ensure high surface sensitivity. A detailed description of the preparation procedure and experimental geometry is given in [34].

A comparison with the spin-resolved photoemission spectra taken from a clean Fe(001) film reveals the modifications evoked by the different interfacial bonding conditions (Fig. 3). The chosen photon energy of 34.2 eV and the experimental geometry allowed one to address the two initial electronic states (Δ_1 and Δ_5) near the Fermi level, which are the most relevant

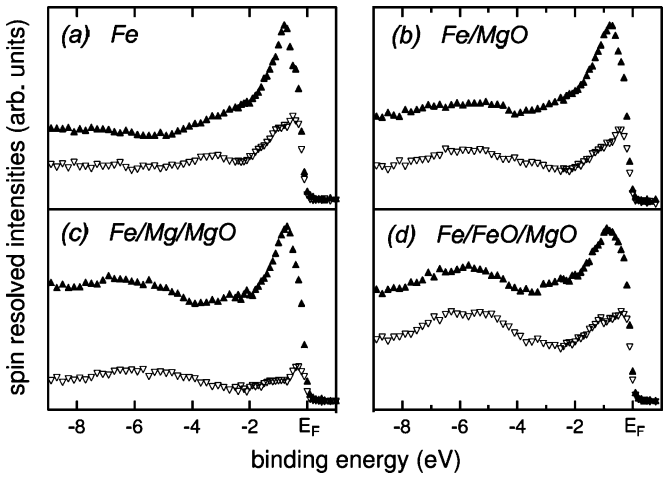

Fig. 3. Spin-resolved photoemission spectra for normal emission ($k_{||} = 0$) from (a) Fe(001), (b) Fe(001)/MgO, (c) Fe/Mg/MgO and (d) Fe/FeO/MgO. ▲ denotes majority spin electrons ($\uparrow$), ▽ denotes minority spin electrons ($\downarrow$). After [34].

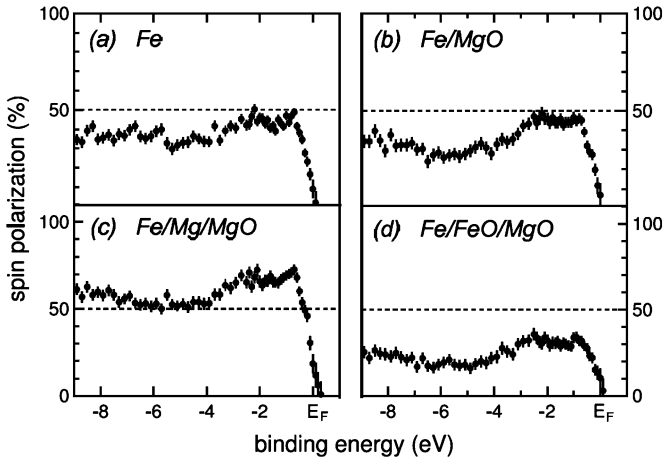

Fig. 4. Spin polarization spectra for the systems (a) Fe(001), (b) Fe(001)/MgO, (c) Fe/Mg/MgO and (d) Fe/FeO/MgO. The dashed lines serve as a guide for the eye. The respective photoemission spectra are displayed in Fig. 3. After [34].

ones for the electronic transport process in Fe/MgO based TMR junctions. In addition, due to the small escape depth of the photoelectrons, the experimental parameters ensured a high surface/interface sensitivity. The photoemission spectra of the uncovered iron electrode are dominated by two peaks, one located at (-0.4 ± 0.2) eV and the other at (-0.9 ± 0.2) below the Fermi level. They are related to direct transitions from initial Fe(001) $3d$ bulk states, originating from $\Delta_1^{\uparrow}$ and $\Delta_5^{\downarrow}$ symmetry bands. For uncovered Fe films, a positive spin polarization of about 40% to 50% in an energy interval from -2 eV to E_F was observed (Fig. 4).

Upon deposition of an ultrathin stoichiometric MgO layer, spectral contributions in the range of about -3.5 to -8.5 eV binding energy manifest in the photoemission spectra, originating from the oxygen $2p$ levels. The excited photoelectrons assigned to this direct transition are unpolarized and thus reduce the total spin polarization measured in this energy region [Fig. 4(b)]. Due to the band gap of MgO (7.6 eV for bulk MgO), it is still possible to observe the direct transitions originating

from iron $\Delta_1^{\uparrow}$ and $\Delta_5^{\downarrow}$ symmetry bands at the Fermi level, provided that the photo-excited electrons can still penetrate the MgO layer. For the calculation of the electronic transport properties in MTJ's an electronically non-interacting Fe/MgO interface is assumed [30], so the Fe interface layer behaves virtually the same as a free Fe surface layer. The photoemission spectra support the theoretical finding at least for the $\Delta_1^{\uparrow}$ and $\Delta_5^{\downarrow}$ bands. The photoemission data [Figs. 3(a) and (b)] display no peak shift in binding energy and the spin polarization change at the Fermi level [Figs. 4(a) and (b)] remains unaffected.

For the under-oxidized interface, however, the experiments reveal a strong change. The spin polarization close to the Fermi level increased to a value of 70% [Fig. 4(c)]. This strong enhancement can be ascribed to a relative change of the spectral contributions originating from the $\Delta_5^{\downarrow}$ state and the Fe 3d $\Delta_1^{\uparrow}$ initial states [Fig. 3(c)]. In the corresponding samples an excess of Mg atoms with two unbound valence band electrons exists at the interface. To discuss the possible origin of this strong electronic modification, the situation may be compared to point defects in bulk crystalline MgO, keeping in mind that the actual excess of Mg in our samples is much higher ($\mathrm{Mg}^{2+}/\mathrm{Mg}^{0} \sim 0.5$). These point defects are called oxygen vacancy states or F-centers and are known to generate highly localized defects states in the band gap [35]. Scanning tunneling spectroscopy and microscopy (STS/STM) experiments on ultrathin MgO(001) films determined the ground state of these localized defect states just about 1 eV below the Fermi level [36]. Theoretical studies by Gibson and Klein [37], [38] predicted that these localized oxygen vacancy states have a Δ_1 like symmetry character. Based on these results in bulk crystalline MgO, the argumentation may be now expanded to the much higher oxygen vacancy concentration existing at the interface of the under-oxidized samples in such a way, that the oxygen vacancy states may interact with each other and form a defect band of Δ_1-like symmetry. The observed enhancement of spin polarization close to E_F may be explained by a hybridization of the defect band and the Fe 3d $\Delta_1^{\uparrow}$ valence band. A theoretical treatment of the Fe/MgO interface with a high density of oxygen vacancies would be needed to confirm this interpretation.

The opposite behavior is found at the over-oxidized interface. Here, the spectral weight of direct transitions originating from the Fe $\Delta_1^{\uparrow}$ state is suppressed compared to the Fe 3d $\Delta_5^{\downarrow}$ state [Fig. 3(d)]. As a result the spin polarization is reduced to about 30% [Fig. 4(d)]. This experimental finding can be explained by a partial oxidation of Fe atoms at the interface. The over-oxidized Fe/MgO interface was theoretically treated by Zhang *et al.* [39] who predicted a strong decrease of Δ_1 majority density of states within the interface. The suppression was ascribed to an augmented redistribution of electrons into in-plane bonds between interfacial iron and oxygen atoms, positioning the oxygen atoms in the bcc hollow-sites of the interfacial iron layer. An additional experimental evidence for the modified chemical bonding between Fe and O can be derived from the spin-resolved photoemission spectra, which depicted a distinct spin-splitting in the O $2p$ spectral features of about 0.4 ± 0.1 eV [Fig. 3(d)]. The spin-splitting is a result of a spin-dependent hybridization of Fe $3d$ wave functions with the O $2p$ states.

These results demonstrate that spin-polarized valence band photoemission spectroscopy experiment allows a sensitive monitoring of the electronic modifications evoked by the altered chemical interface conditions. The spin-sensitive approach is a valuable tool to compare experimental data of the interfacial electronic structure and theoretical modeling. In the future, a closer cross correlation between theoretical photocurrent calculations and spin-resolved photoemission spectroscopy may even offer a possibility to design the electronic interface conditions to further improve spin-dependent electronic transport properties in spintronic devices.

In addition to explicit spin-resolution, magnetic sensitivity in photoemission can also be achieved by exploiting various magnetic dichroism effects. These can be utilized in a conventional photoemission experiment, in particular, when the experimental setup offers the possibility of controlling the polarization of the synchrotron light. Dichroic effects can be observed both in core levels and valence bands, with the initially discovered magnetic circular dichroism in photoemission [11] followed by a similar effect using linearly polarized [40] and even unpolarized [41] light.

Magnetic linear dichroism (MLD) at the Fe 3p levels provides a particularly strong signal. It was therefore employed as a complementary evidence in another recent spin-polarized study of the MgO/Fe(001) system [42]. These results can serve as an example on how dichroic effects can be used in the future studies of novel thin film structures. MLD data are typically obtained by measuring angle-resolved photoemission spectra of core levels for the sample magnetized into opposite directions. However, the effect can be also observed in valence bands [13].

We refer to [42] for experimental details, but in short the experiments were performed with p-polarized light, at normal emission geometry using a hemispherical photoemission analyzer in angle-resolved mode with $\pm 1^{\circ}$ angular acceptance. The sample preparation was done *in situ*, with the Fe films being deposited onto Mo(001) by electron beam evaporation, and the MgO overlayers being grown from pieces of stoichiometric MgO single crystals put into a tungsten crucible and heated by electron beam bombardment. The goal of the study was to establish whether an interfacial FeO layer is present in stoichiometric MgO/Fe(001) films prepared in this way.

At a photon energy of 128 eV, one can simultaneously excite both, the Fe $3p$, and the Mg $2p$ levels. These core levels are located at binding energies of 53 eV and 51 eV, respectively and, although quite close, they still offer the possibility of monitoring the two different materials during the formation of the interface. The core level data are displayed in Fig. 5, where results concerning the growth and annealing of MgO layers on top of Fe(001) surface are shown. The left panel presents mostly dichroic averaged spectra (continuous lines), while the right panel shows the corresponding dichroism spectra (open and closed circles), in an expanded view emphasizing the smaller region around the Fe $3p$ levels.

Comparing the spectra from the clean Fe(100) surface [Fig. 5(a)] to the ones exposed to 1 Langmuir of molecular oxygen [Fig. 5(b)], the appearance of a shoulder on the high binding energy side of the spectrum is evident. This shoulder feature, best seen in the right panel of Fig. 5, is typical of the reaction of oxygen with Fe and indicates the formation of Fe oxide [43]. In agreement with the valence band observations, this shoulder does not display any dichroism, indicating the formation of an unpolarized surface oxide after only 1 L of

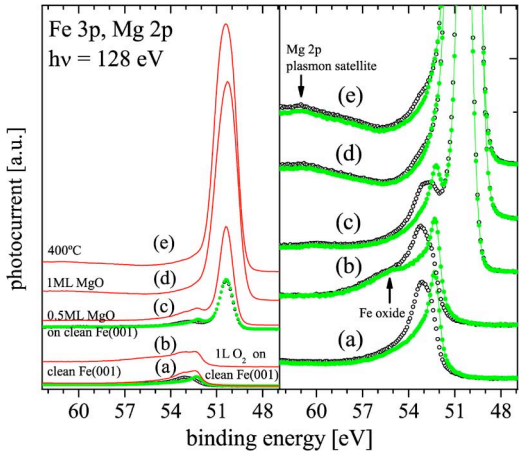

Fig. 5. Fe $3p$ and Mg $2p$ core level normal emission energy distribution curves at $h\nu = 128$ eV; (a) clean Fe(001), (b) Fe(001) exposed to 1 Langmuir of molecular oxygen, (c) 0.5 ML MgO/Fe(001) deposited on clean Fe(001), (d) 1 ML MgO/Fe(001), (e) previous films annealed to 400°C for 5 min. In the left panel the sum of spectra from the sample magnetized in opposite directions are plotted. The right panel shows the same spectra as on the left, but renormalized to magnify the Fe $3p$ contribution. Open and filled circles represent spectra from the sample magnetized in opposite directions. All spectra were measured at room temperature.

oxygen exposure to the clean Fe surface. Most importantly, when MgO is deposited on clean Fe(001) instead [Fig. 5(c)], there is no indication of this feature in the spectra. On the contrary, the curvature of the relevant part of the core level spectrum remains clearly positive for 1 ML MgO coverage, which is an evidence that no FeO layer is present at the stoichiometric MgO(100)/Fe(100) interface.

At higher MgO deposition, the Fe $3p$ emission becomes rapidly obscured by the much more intense Mg $2p$ levels [Figs. 5(c), (d)] but the Fe dichroism remains strong, which indicates a highly polarized Fe substrate in contact with the MgO overlayer. It is also useful to note that while the Fe dichroism is very strong, no sign of any dichroism is detected under the Mg peak (the full dichroic spectra are shown in the left panel for the case 0.5 ML MgO, as an example). This again tends to confirm the weak interaction between Fe and MgO at the interface.

For the thicker films where no Fe signal remains, there is no additional Mg $2p$ line related to metallic Mg. According to one study ([44]) such a metallic feature would be expected to appear at 2 eV lower binding energy from the main $2p$ line of MgO and its complete absence is therefore a further confirmation of the good stoichiometry of these films. In agreement to what was found in the valence band study, when annealing MgO/Fe(100) interface to 400°C [Fig. 5(e)] there is little change in the core level with only the shape of the Mg $2p$ spectra becoming slightly more symmetrical. Additionally, upon annealing the 1 ML MgO/Fe(001), a new small feature, which is barely visible in the room temperature-deposited MgO, clearly appears at 10.7 eV above the Mg $2p$ binding energy but, quite independently of the precise interpretation, the observed sharpening of the features indicates a structural reordering of the MgO layer induced by annealing.

B. Element-Selective Studies of Magnetic Moments

The investigation of element-specific magnetic properties is an essential task for the understanding of magnetic interactions, which in turn is crucial for the development of modern magnetic and spintronic devices. The bestowal of the Nobel prize in Physics in 2007 to P. Grünberg and A. Fert [45] for the discovery of the giant magnetoresistance (GMR) effect stresses this point very clearly. The GMR effect was discovered in layered magnetic structures of Fe and Cr [46], [47], which exhibit a particular magnetic coupling—the interlayer exchange coupling [48] leading to a magnetic ground state with antiparallel orientation of the magnetization in neighboring layers. These prototype systems can be studied element- and shell-specifically utilizing the X-ray magnetic circular dichroism (XMCD) technique and much has been learned about magnetic coupling and proximity effects in layered systems in this way.

1) XMCD Sum Rules: After the theoretical prediction of the XMCD effect by Erskine and Stern [49] in 1975 it took more than a decade for the first experimental realization [9]. The theoretical development of the so-called XMCD sum rules [50], [51] boosted its use enormously. The reason is that by means of these sum rules the spin and orbital magnetic moments can be determined from the integrated XMCD signal. Nowadays, scientists in various fields like physics, chemistry and biology apply the XMCD technique as a standard tool for the analysis of magnetic properties (see e.g. [60], [65]). However, this standard use also carries some danger: In the original works on the derivation of the analysis procedures, i.e., the sum rules [50], [51] or the multipole-moment analysis [66] various assumptions and consequently the limits of these analysis procedures are stated. If these limits are ignored, the analysis yields erroneous results as will be discussed below.

Within these limits the spin moment μ_S and orbital moment μ_L are determined by the sum rule procedure (for details see also e.g. [52]–[60]) at the $L_{2,3}$ edges by the following integrals:

$$\mu_L/\mu_B = -\frac{2N_h}{N}\int (\Delta\mu_{L_3} + \Delta\mu_{L_2})\,dE, \tag{6}$$

$$\mu_S/\mu_B = -\frac{3N_h}{N}\int (\Delta\mu_{L_3} - 2\Delta\mu_{L_2})\,dE + 7\langle T_z\rangle \tag{7}$$

where $\Delta\mu_{L_3} = \mu^+_{L_3} - \mu^-_{L_3}$ is the XMCD difference of the X-ray absorption coefficients for right and left circularly polarized X-rays at the L_3 edge. Additionally the integrated spectrum for the unpolarized radiation $N = \int_{L_3+L_2}(\mu^+ + \mu^- + \mu^0)dE$ and the number of unoccupied d states N_h enter into the equations given above. By the expectation value of the magnetic dipole operator $\langle T_z\rangle$ the asphericity of the spin magnetization is considered. The influence of this term on the XMCD can be identified for instance by angular dependent measurements [61]. Interestingly, the sum rules work astonishingly well as it is demonstrated e.g. for the ferromagnets Fe, Co and Ni [55], [59], [62] which indicates that the assumptions made in the sum rule derivation are justified—at least for these elements.

The application of the integral sum rules is exemplified for the $L_{2,3}$-edge XMCD signal of a bulk like Ni-film as shown in Fig. 6. To determine the orbital moment μ_L the entire XMCD signal has to be integrated (marked area) as described by (6). The integral is depicted by the dashed line and the constant value indicated by the arrow is used to calculate μ_L. To analyze the spin moment μ_S the L_2 edge contribution has to be subtracted from the L_3 edge one. Hence, these two contributions have to be separated. The resulting integral is given by the solid line and

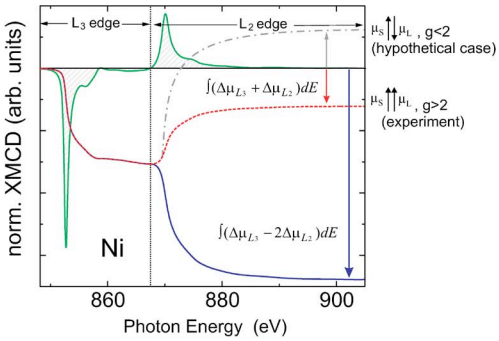

Fig. 6. XMCD difference for a bulk-like Ni film and the XMCD integrals which are necessary for the application of the integral sum rules (figure taken from [65]).

from the value marked with the larger arrow the spin moment is calculated. An advantage of this analysis procedure is that from these integrals an investigation of the relative orientation of the spin to the orbital moment is directly possible: Since both values of the integrals exhibit the same sign a parallel alignment of μ_S to μ_L is revealed from Fig. 6. From this relative orientation an estimation of the g-factor is possible by the relation $\mu_L/\mu_S = (g-2)/2$ as discussed in [63], [64]. For the Ni-case discussed here $g > 2$ can be concluded because of the parallel alignment of μ_L and μ_S. This is in agreement with the expectation according to the third Hund's rule since a parallel alignment of the orbital and the spin moment is expected for more than half-filled shells. Strictly speaking the application of Hund's rules are only valid for atoms, however, the prediction of the relative orientation of μ_S to μ_L by the third Hund's rule is correct for various solids (see e.g. [65]). An antiparallel alignment is expected for the lighter elements of the $3d$ transition metals as for example V. In this case the integral of the entire XMCD signal would cross the zero line as depicted schematically by the hypothetical dot-dashed line which corresponds to $g < 2$.

2) XMCD From Magnetic Biomolecules: The power of the XMCD technique is now illustrated for the analysis of the magnetic coupling of magnetic bio-molecules (Fe-porphyrins) to a ferromagnetic film. To realize the vision of molecular nanoelectronics a fundamental understanding of the interaction of the molecules with surfaces is essential and this holds, of course, also for the molecular spintronics counterpart. Fe-octaethylporphyrin (OEP) molecules with monolayer (ML) coverage on epitaxially grown Ni and Co films on Cu(100) were chosen to serve as a prototype system [67], [68]. Since 1 ML Fe-OEP corresponds to an effective Fe coverage of ~1/100 ML a highly sensitive technique like XMCD is required to pick up the magnetic signature.

The monolayer of the Fe-OEP molecules is prepared *in-situ* by sublimating Fe-OEP-chloride (Fig. 7) at 485 K. The substrate is a 15 ML Ni film, which was epitaxially grown on a Cu(100) single crystal. Further experimental details can be found in [67]. The X-ray absorption spectra (XAS) for right and left circularly polarized X-rays and the corresponding XMCD spectra are presented in Fig. 7. Here, the advantages of the XMCD technique become obvious: since the absorption edges of the different elements are well separated, the magnetic properties of the Fe atoms in the molecule can be studied separately

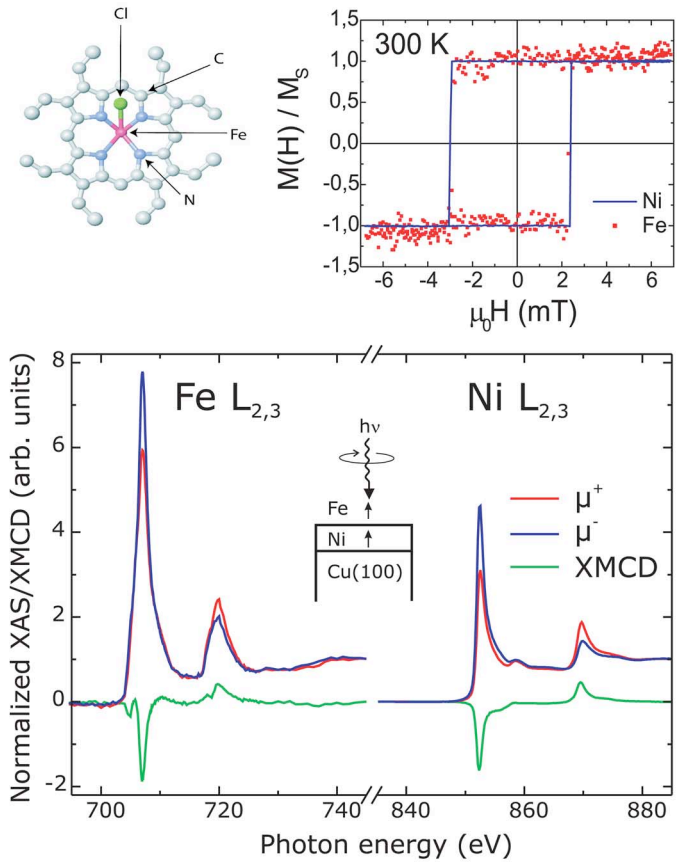

Fig. 7. Top left: schematic illustration of the Fe-OEP-chloride molecule. Top right: element-specific hysteresis curves of the Fe atom (filled squares) and Ni (full line) obtained by the L_3 edge XMCD maxima of Fe OEP on Ni/Cu(100) at 300 K. Bottom: normalized X-ray absorption coefficients for right and left circularly polarized X-rays $\mu^+(\mathrm{E})$ (red) and $\mu^-(\mathrm{E})$ (blue) and XMCD (green) at the $L_{2,3}$-edges of the central Fe atom of the OEP molecule and the Ni film (300 K, 10 mT). The inset depicts the orientation of the sample to the incident X-rays. The arrows for Fe and the Ni film show the alignment of the spins. After [67].

from the underlying Ni film by investigating the respective $L_{2,3}$ edges. The edge jumps (signal to background ratios) are scaled to unity. Therefore, the Fe edge jump had to be scaled up by about three orders of magnitude relative to the Ni edge jump. This is because of the dramatically different coverages ($\mathrm{effective\,Fe\,coverage} :\sim 1/100\,\mathrm{ML} \leftrightarrow \mathrm{Ni\,coverage} : 15\,\mathrm{ML}$). This is the reason for the larger noise for the Fe spectra. But because of the use of an undulator setup even fine structures can be resolved in the dichroic spectra. Thereby, the magnetic polarization of the individual Fe orbitals can be investigated. Additionally, the X-ray absorption spectra at the N and C K-edges (not shown) were measured versus the X-ray incidence angle, which showed the molecules to lie flat on the surface. This allows for a magnetic coupling of the paramagnetic molecules to the ferromagnetic Ni film. Such a coupling is indeed revealed by the XMCD spectra: The existence of a clear Fe XMCD signal at 300 K in a small applied field of 10 mT demonstrates that the Fe moments in the molecule are ordered by the Ni film. This coupling is of ferromagnetic nature as can be seen by the same sign of the XMCD signals at the Fe and Ni $L_{2,3}$-edges and the identical element specific hysteresis loops.

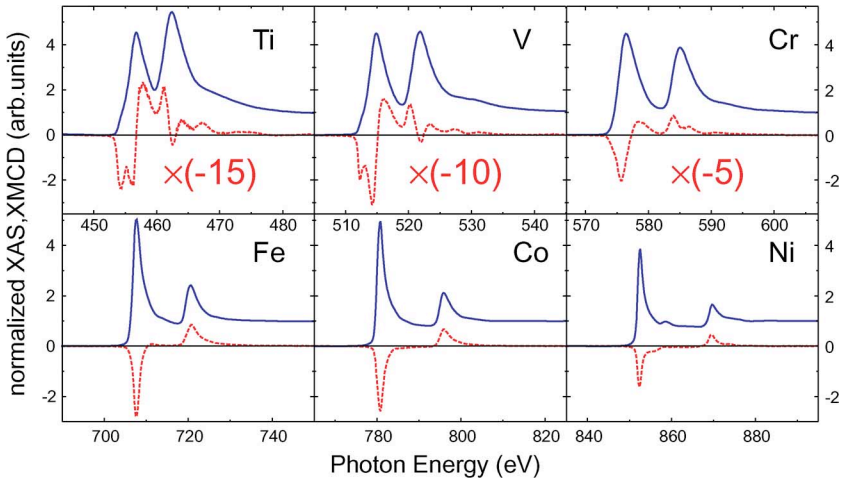

Fig. 8. Normalized isotropic spectra (solid lines) and corresponding XMCD spectra (dotted lines) for the light $3d$ transition metals in the upper panel in comparison to the heavy $3d$ ferromagnetic transition metals Fe, Co and Ni in the lower panel at the $L_{2,3}$ edges. The XMCD spectra for the light $3d$ transition metals are obtained for Fe/light $3d$/Fe(110) trilayers, whereas the Fe, Co and Ni spectra are recorded for bulk-like films on Cu(100). The direction of the magnetization for the light $3d$ metals is defined with respect to the one of Fe in the trilayer. For a clearer presentation of the systematics, the sign of the Ti, V and Cr XMCD spectra was changed (please note the negative enlargement factors). Taken from [70].

Interestingly, density functional theory calculations demonstrate that this coupling is due to an indirect 90° exchange mechanism via the N atoms [67]. From the sum rule analysis we determine an effective Fe spin moment (including the magnetic dipole term $\langle T_z \rangle$) from experimental XMCD data at 70 K (not shown) of $\mu_S^{eff}(\mathrm{Fe}) = 0.45 \pm 0.1\ \mu_B/\mathrm{hole}$ [68]. The XAS at the Fe $L_{2,3}$-edges indicates that Fe is in a divalent state. This yields an effective Fe spin moment of $\mu_S^{eff}(\mathrm{Fe}) \approx 2\ \mu_B$ which is consistent with an intermediate spin state [68].

3) Limits of the Sum Rule Analysis: The second example addresses the limits of the standard analysis procedures for XMCD spectra in the case of layered magnetic structures in order to illustrate the danger of misinterpretation. In the ultrathin limit magnetic moments in light $3d$ transition metal (TM) elements (Ti, V, Cr) can be measured, but the standard analysis procedures fail to yield reliable quantitative values [65], [69]–[71]. Only by the help of *ab initio* calculations the spin and orbital moments can be determined reliably. An instructive case study is provided by Fe/[light $3d$ TM]/Fe trilayers, where the Fe layers have bulk-like properties, whereas the spacer layers (Ti, V, Cr) have thicknesses in the ultrathin limit, i.e., 1–3 atomic layers. Often these spacer layers are treated as nonmagnetic in the literature. For the ultrathin limit, however, this is not correct—the proximity to Fe leads to finite magnetic moments, which should show up as a sizable $L_{2,3}$-edge XMCD. To achieve a systematic understanding the results for Ti, V, and Cr interlayers are compared to the XMCD spectra of bulk-like films of the ferromagnets Fe, Co and Ni in Fig. 8. The clear XMCD signals reveal that indeed spin moments (aligned antiparallel to the Fe moments) can be determined for the light $3d$ elements. These originate from induced moments due to hybridization (Ti,V) or from uncompensated moments in the layer-wise antiferromagnet Cr.

Although the XMCD spectra are nearly free of noise the application of the standard analysis procedures by means of the sum rules and the multipole-moment analysis yield erroneous quantitative results. By comparison to *ab initio* calculations and neutron scattering experiments the induced spin moment in V, for example, is wrong by a factor 5 ([65]). The reason is the change of the L_3 to L_2 intensity ratio along the $3d$ series as it is obvious in Fig. 8. Since these intensities enter into the moment determination, difficulties in the sum rule analysis can be expected. For the light $3d$ elements Ti, V and Cr this ratio is in the regime of 1:1, whereas the ratio becomes about 2:1 (statistical branching ratio) for the ferromagnets Fe, Co and Ni.

A recent work by Scherz *et al.* showed that the core hole couples the two excitations (L_3 and L_2 edges) [72]. Within a double-pole approximation the matrix elements of the unknown exchange-correlation kernel could be extracted from the experimental branching ratios [72]. These results illustrates how the standard procedures for the XMCD analysis can fail and that they should not be applied without careful consideration. In the above case, the ground state properties of these systems could only be determined by the help of *ab initio* calculations. An additional problem occurs when analyzing the $5d$ moments in rare earths at the $L_{2,3}$ edges. For these systems the transition matrix elements are spin-dependent—a fact, which is ignored in the standard analysis procedures. This may even lead to a wrong sign for the $5d$ moments when the sum rule analysis is applied. Therefore, a generalized form of the sum rules is needed, which takes into account the spin dependence of the transition matrix elements [58].

C. Thin Film Heusler Phases

The element-selectivity of XMCD spectroscopy is not only a virtue in the study of thin film systems. It has also enabled a much better understanding of the specific properties of complex magnetic alloys and compounds. This can be very nicely demonstrated by investigations of ferromagnetic Heusler phases, which more than 100 years after their discovery [73] have recently experienced a renewed interest. The potential applications of these materials has stimulated increasing scientific work in this field. Ferromagnetic half-metallic properties of Heusler alloys of the type $\mathrm{Co_2YZ}$ as predicted by ab-initio calculations [74], [75] make them promising materials for next generation spin electronics [76]. Recent experimental progress

confirms the large potential of these alloys [77]–[82]. An additional technical application of Heusler alloys arises from the shape memory effect found for alloys derived from Ni_2MnGa revealing a huge magnetically induced length change of up to 10% [83], [84]. Potential applications for shape memory alloys include actuators and magnetocaloric devices on a nanoscale [85], [86].

Heusler alloys are compounds with the stoichiometric composition X_2YZ ordered in a $L2_1$-type structure. A Heusler alloy consists of two different transition metals X and Y and a main group (nonmagnetic) element Z. For tuning material properties the sublattices are in general occupied by a random distribution of two different transition metals, e.g. $Co_2(Cr_{0.6}Fe_{0.4})Al$, thus forming quaternary compounds. The magnetic moments of Heusler alloys are distributed among the various constituents. For a thorough understanding of the magnetic properties of Heusler alloys an element-specific spectroscopic experiment capable to measure individual elemental properties is essential and XMCD is ideally suited for this task. In addition to the determination of element-specific magnetic spin and orbital moments using the sum rule evaluation one can exploit the spectroscopic information offering a view on the local unoccupied density-of-states (LDOS) function.

The tailoring of the magnetic and electronic properties of Heusler alloys for individual applications provides the main future challenge. In this field XMCD will play a major role as a bridging method between theory and experiment. Beyond the characterization of bulk properties of Heusler alloys their magnetization variation at interfaces becomes increasingly important when Heusler alloys are implemented in nanoscopic devices. Using different detection techniques for the X-ray absorption, bulk, and interface properties can be determined separately.

For half-metallic Heusler alloy films deviations of interface properties from their bulk properties are a severe obstacle for their implementation in magnetic sensor devices, e.g., the preparation of the AlO_x barrier of a TMR device requires the deposition of a metallic Al layer on the Heusler alloy surface of a thin film as a crucial first preparation step [78], [79], [82]. Previous experiments already revealed decreased magnetization values at the interface of Heusler alloys [87]–[89]. In order to explain the deviating interface properties, a simultaneous XAS detection via the total electron yield (TEY) providing an information depth of 0.8 nm–2.5 nm and via the bulk-sensitive XAS transmission (TM) can be employed. A direct comparison of these signals will then sensitively reveal discrepancies between electronic properties at the interface and in the core of the films.

Fig. 9 shows TEY and TM XAS obtained simultaneously for two differently prepared $Co_2(Cr_{0.6}Fe_{0.4})Al$ films [90]. The $Co_2(Cr_{0.6}Fe_{0.4})Al$ film on $Al_2O_3(11\bar{2}0)$ (sample I) reveals a poor atomic order as it was deposited at low temperature on the bare substrate. The poor order is reflected by the comparatively small extra peak A at about 3.8 eV above the L_3 edge. Peak A stems from a Co $3d$—Al $2p$ hybridized state occurring exclusively in fully $L2_1$ ordered unit cells [92]. The implementation of a buffer layer on the MgO substrate and an additional annealing step leads to an increased atomic order of the $Co_2(Cr_{0.6}Fe_{0.4})Al/MgO$ film (sample II) [93] indicated by an increase of peak A [Fig. 9(a)].

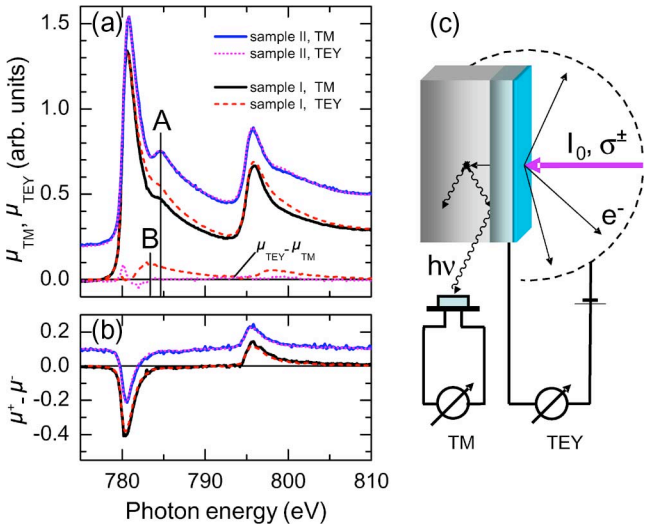

Fig. 9. (a) XAS measured at 300 K by total electron yield (TEY) and transmission (TM) for two $Co_2(Cr_{0.6}Fe_{0.4})Al$ film samples. Sample I is a 110-nm-thick $Co_2(Cr_{0.6}Fe_{0.4})Al/Al_2O_3(11\bar{2}0)$ film capped by 6 nm Al at 480 K. Sample II is a 100-nm-thick $Co_2(Cr_{0.6}Fe_{0.4})Al/Fe/MgO(100)$ film capped by 4 nm Al at 320 K. XAS spectra shifted for clarity. The difference spectra $\mu_{TEY}-\mu_{TM}$ are indicated by the dashed (red, sample I) and dotted (pink, sample II) line. (b) Corresponding XMCD spectra. (c) Sketch of the experimental set-up. See also Ref. [90].

Any difference between Co $L_{3,2}$ TM and TEY XAS indicates structural deviations at the interface. The difference of the TEY- and TM spectra of sample I reveals an additional peak B at 2.5 eV above the L_3 maximum [dashed red line in Fig. 9(a)]. This peak is characteristic for the formation of a stoichiometric CoAl compound [94], [95]. The higher Al coordination for Co in CoAl in comparison to $Co_2(Cr_{0.6}Fe_{0.4})Al$ shifts the hybridization state to lower energies. Because CoAl is paramagnetic, this solid state reaction leads to a decreased XMCD signal at the interface. This explains the observed decrease of 20% of the interface magnetization [88]. The comparison of TEY and TM XAS for sample II signalizes that low-temperature deposition of Al avoids the formation of CoAl. The almost equal XMCD signals for sample II indicate that the Co magnetic moment at the interface and in the core of the film are similar. An interesting pronounced difference between TEY and TM XAS signals of sample II remains at the onset of the absorption maximum. This difference reflects a shift of the unoccupied density-of-states maximum at the Al-interface closer to the Fermi edge [90].

The phase transition from the cubic $L2_1$ structure to a tetragonally distorted martensitic (MS) phase below T_m is a precondition for the occurrence of the magnetic shape memory effect in Ni_2MnGa [83], [84], [96], [97]. The understanding of the origin of this phase transition is of utmost importance for the development of electronic devices exploiting the shape memory effect. Ab-initio calculations [98]–[100] show a change of the electronic structure at T_m, essentially involving Ni-derived minority d-states. States with Ni $3d_{z^2}$ and $3d_{x^2-y^2}$ symmetry, that are degenerate in the cubic state, split up in the tetragonal phase. An experimental test of ab-initio calculations is difficult, because these changes are usually very tiny. According to the comparatively large structural change in Ni_2MnGa Ayuela *et al.* [100]

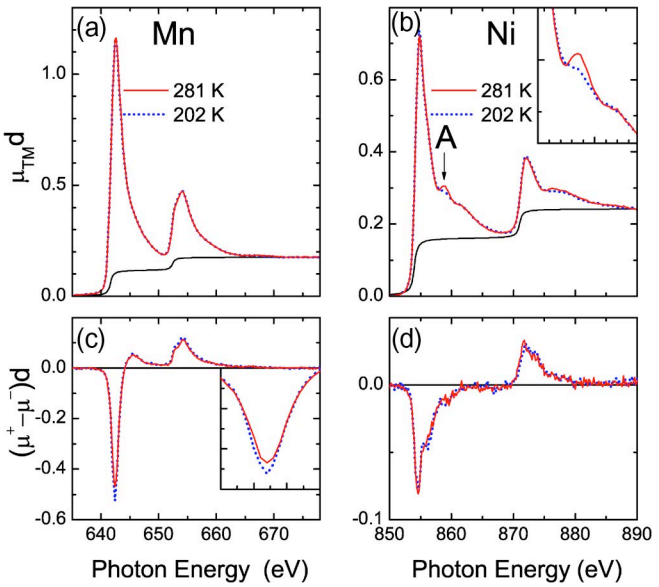

Fig. 10. Absorption coefficient times thickness, $\mu_{TM}d$, of X-ray light transmitted through a 83 nm Ni_2MnGa (110) film on $\alpha - Al_2O_3$ at the Mn (a) and Ni (b) $L_{2,3}$ edge. The inset in (b) emphasizes the difference of feature A above and below T_m. XMCD signals, $(\mu^+ - \mu^-)$ for Mn (c) and Ni (d). The inset in (c) shows the L_3 maximum revealing the temperature induced decrease of the Mn XMCD signal. Taken from Ref. [91].

predicted that the subtle band structure modification at the MST should lead to experimentally observable changes of the X-ray absorption (XAS) spectra.

XAS spectra of the Mn and Ni $L_{2,3}$-edges are shown in Fig. 10 for $Ni_2MnGa(110)/Al_2O_3(11\bar{2}0)$ [91]. Figs. 10(c) and (d) show the corresponding XMCD signals. The intensity of the feature A in the Ni absorption signal [indicated in Fig. 10(b)] clearly depends on the structural phase. While this peak is well pronounced for $T > T_m = 275$ K it is nearly suppressed for $T < T_m$. The observed increase of A at T_m is in full agreement with the theoretical prediction by Ayuela *et al.* [100]. Changes at T_m in the Mn $L_{3,2}$ spectra are hardly measurable. This is expected in the case of $c/a < 1$ where the Fermi level lies in a position at which there is almost an equal LDOS of majority and minority t_{2g} states. In the case of $c/a > 1$ larger changes of the LDOS would be caused by hybridization because the atoms become closer in the ab-plane. Thus the XAS result is in favor of $c/a < 1$ [91].

The second important ingredient of the magnetic shape memory effect is the presence of a strong uniaxial magnetic anisotropy exceeding the energy density needed to drive the twin boundaries in the MS phase. The magnetic anisotropy is caused by the spin-orbit interaction and thus directly related to the orbital magnetic moment [101]–[103].

The orbital to spin moment ratio for Ni amounts to $\mu_{orb}/\mu_{spin} = 0.15$ in the MS phase and decreases to 0.05 at room temperature [91]. An increased Ni orbital moment in the MS state is expected because of the lower symmetry of the corresponding crystal field. The observed value is significantly larger than the value of bulk Ni (0.1). The Mn orbital moment is negligibly small (<0.01) for both phases. Therefore, the magnetic anisotropy is exclusively caused by electronic states located at the Ni atom.

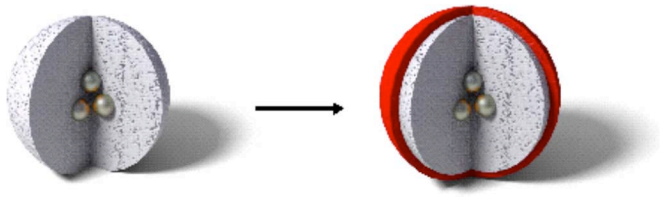

Fig. 11. Schematic illustration of magnetic silica spheres coated with an outer shell of gold.

The Ni and Mn spin moments do not vary significantly at T_m with values of $\mu_{spin}/N_h = 0.17\ \mu_B$ for Ni and $\mu_{spin}/N_h = 0.355\ \mu_B$ for Mn [91]. Considering the different values for N_h for Ni (1.3) and Mn (4.3) and also a correction factor for Mn of 1.5 because of the jj mixing, the ratio between Mn and Ni moment is roughly a factor of 10, in agreement with ab-initio theory [98], [100].

These examples show that the careful analysis of interface-related and bulk-sensitive XAS signals will provide considerable progress in the understanding and tailoring of the electronic structure of Heusler alloys with respect to dedicated applications.

D. Magnetic Nanoparticles and Clusters

The power of the XMCD spectroscopy approach to the study of magnetic molecules has been already discussed in Section IV-B. The technique has also been successfully employed in the investigation of single molecule magnet crystals [104]–[107]. However, two other interesting classes of nanomagnetic structures, where XMCD has contributed much to our current understanding of magnetic properties, comprise core-shell nanoparticles and clusters. In both cases the surface-to-volume ratio is very high and a significant modification of the average magnetic properties must be expected. The main challenge lies in separating the surface or core-shell interface magnetic contributions from the bulk response.

1) Magnetic Core-Shell Particles: Magnetic core-shell nanoparticles may be defined as particles which contain a core of material A with a diameter of 3 to 50 nm and a shell of material B with a thickness of 1 to 25 nm (Fig. 11). Materials A and B may consist of one or more elements and at least one of both materials should be ferro-, ferri-, or antiferromagnetic, while the other one may be para- or diamagnetic. Examples are Fe_3O_4@Fe that is Fe_3O_4 at (or around) a Fe core [108], CoO@Co [109], CoO@Ag [110], SiO_x@Co [111], $CdTe@SiO_x@FeO_x$ [112], among others [113]–[120]. The core may even be free of material, i.e., the particle can be hollow [121], [122]. Particles may have the shape of rods, spheres, platonic solids (e.g. icosahedra) or cubes [123], where at least one dimension is limited to below 100 nm [114], [123]–[128]. Many types of hybrid particles with different bi- [112], [120], [129] and multifunctionalities have been synthesized this way and can be regarded as tailored building blocks for macroscopic materials combining specially designed optical, dielectric, mechanical, and magnetic properties. Examples include magnetic and luminescent functionality as well as magnetic and catalytic activity.

Unfortunately, the word "nanoparticle" has been used in different contexts in the literature like, for example, for particles, capsules, tubes or rods with sub-micron or micron dimensions.

The realm of magnetic nanoparticle physics is on the 3 to 100 nm length scale, which is above the size of cluster physics where one observes quantum phenomena, and below the size range where effects of surface layers become negligible. Such particles can be prepared by different wet-chemical approaches [130]–[132] and gas-phase condensation techniques with well-defined sizes and shapes. Colloidal core-shell particles always are covered by an additional layer of usually organic molecules to stabilize them in the solvent. The role of theses ligands has often been neglected in the interpretation of magnetic data of colloidal particles. They effectively constitute an additional shell yielding this way a multishell nanoparticle.

Measurements of magnetic properties of nanoparticles require size-fractionized, i.e., monodisperse, ensembles. An ensemble of usually billions of particles has been defined as monodisperse when a statistically relevant size and shape distribution analysis yields a size or volume variation of less than $\pm 20\%$ meaning that an ensemble of monodisperse 6 nm particles contains particles with 7.2 and 4.8 nm particles. This in turn means that the total number of atoms in ideal spherical particles with fcc structure varies between 6000 and 18 000 atoms and the percentage of surface atoms varies between 32 and 24%. This can be compared to the behavior of a magnetic thin film, where it is well-known that an 8 monolayer film with 2 surface and 6 core layers (25% surface atoms) shows a very different magnetic response than a 6 monolayer film (33% surface atoms) [133]. An additional even bigger inhomogeneity lies in the temperature dependent temporal response of nanoparticles. Due to the small magnetostatic energy of the nanomagnet the direction of the magnetization is thermally unstable and fluctuates in time. This behavior depends in an exponential fashion on the particle's magnetic anisotropy K_{eff}, volume V and the temperature T. It is characterized by a "blocking temperature" T_b below which the magnetization M is thermally stable over the duration of the magnetic measurement [134]. In an ensemble measurement the magnetization of smaller particles may fluctuate so quickly that over the time window of the measurement only bigger particles dominate the effectively measured magnetization and magnetic anisotropy while the signal of the small particles is negligible. Consequently, monodispersity in shape and size is not sufficient for magnetic particles. "Magnetic monodispersity" of an ensemble of "monodisperse" particles requires truly uniform sizes and shapes of all particles, or at least a much narrower size distribution than given by the definition of the geometrical or mass "monodispersity." This problem is even enhanced for core-shell type particles.

Measurements which integrate over billions of particles yield an averaged magnetic response which in the worst case may be dominated by very few "large" (micrometer sized) particles which may have escaped the attention of the structural X-ray or electron microscopist. Hence, to interpret magnetic measurements of nanoparticle ensembles in a reliable way a "magnetically monodisperse" particle ensemble must [65] be synthesized, and its size and shape distribution must be well defined. Consequently, the initial challenge is to synthesize "magnetically monodisperse" core-shell particles. Such a goal is extremely difficult—maybe impossible—to achieve. Nevertheless, by innovative chemical and physical synthesis techniques the monodispersity in nanoparticle production has been continuously improved.

Synchrotron-based element-specific techniques like X-ray absorption spectroscopy (XAS) [65] including near edge and extended energy regions (NEXAFS, EXFAS) and X-ray magnetic circular dichroism (XMCD) have proven extremely valuable to identify the inhomogeneous distributions of magnetic moments in bimetallic nanoparticles and core-shell particles. To investigate the intrinsic magnetism the organic ligand shell and residual oxide layers which influence the magnetic response must be removed, and the technical aspect of saturation correction and sampling depth in electron yield for spherical particles must be properly taken into account [135], [136]. An illustrative example has been given for Co nanoparticles. Here, the combination of high resolution transmission electron microscopy (HR-TEM) with nm resolved elemental specificity and XAS confirmed the existence of an polycrystalline oxide layer despite the "protective" oleic acid ligand layer [109], [110]. The controlled removal of the ligand and oxide layer by an in-situ plasma process showed that the extremely high ratio of orbital-to-spin magnetic moment initially measured for the untreated "Co" particles [137] was due to the presence of uncompensated Co^{2+} ions in an oxidic environment [109], [138]. Combining Ferromagnetic Resonance with XMCD in the electron yield mode and the high-resolution structural analysis by HR-TEM it was even possible to arrive at a quantitative model for the number of interface magnetic moments at the inner Co/CoO and outer CoO/vacuum interface.

Similarly, inhomogeneities in bimetallic particles complicate the analysis. Taking the case of the chemically well-ordered $L1_0$ crystal structure of FePt [139] it is evident that the different facets of an icosahedra [140] may consist of pure Fe, pure Pt or mixed Fe/Pt surfaces. Similarly, $\mathrm{Fe}/\mathrm{FeO}_x$ particles can be regarded (Fig. 12). Where is the iron atom located which is in contact with oxygen? It may be present at the surface or in the interior. Element-specific analysis by XAFS and XMCD using the surface sensitive electron yield or the bulk sensitive fluorescence yield detection can help to identify surfaces enriched by one or the other element, if the particle is bigger than 10 nm [141], [142]. Such studies represent the state of the art, since they are based on an extremely careful preparation of the organometallically or gas-phase synthesized particles involving the following steps:

a) synthesis and multiple centrifugation of colloidal nanoparticles to reduce the size-distribution well below 5%
b) the controlled deposition of a two-dimensional layer on an area of at least the diameter of the synchrotron beam
c) the imaging of the size and shape of the two-dimensional island by scanning or transmission electron microscopy
d) the in-situ removal of oxides and organic ligands before the synchrotron measurement in a low energy hydrogen plasma
e) in-situ chemical analysis by XAFS
f) magnetic or structural investigations by XMCD or EXAFS as a function of temperature, magnetic field, orientation of the sample with respect to the synchrotron beam and the magnetic field and the magnetic history of the sample, i.e., zero-field cooled and field-cooled state

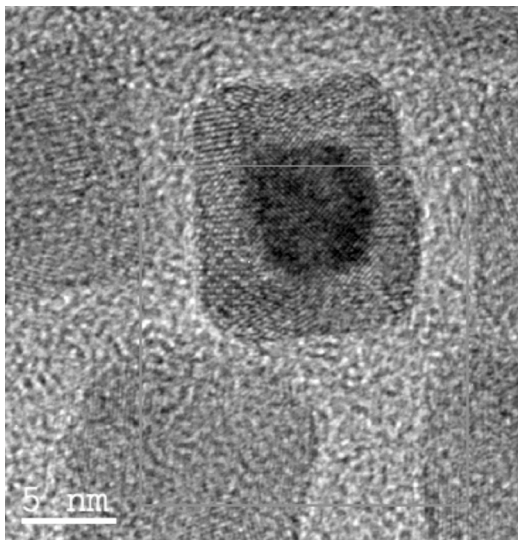

Fig. 12. Bright field transmission electron microscopy image of a single Fe oxide@Fe core-shell nanocube [108]. The outer cube edge is 10 nm and the brighter oxide shell thickness is around 2.5 nm thick.

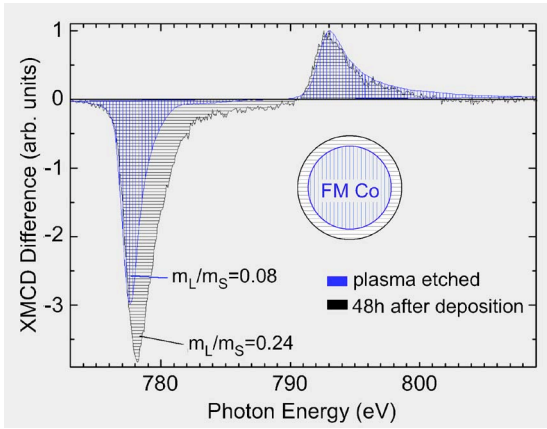

Fig. 13. XMCD spectra at the $L_{3,2}$ edges of Co nanoparticles before (parallel shading) and after plasma removal of the CoO shell. Spectra were normalized to the L_2 edge. As discussed in [109] the Co^{2+} ions at the surface and the interface between the Co core and the 2 nm thick antiferromagnetic CoO shell are the origin of the measured strongly enhanced ratio of the orbital-to-spin momentum $\mu_L/\mu_S = 0.24$. After reduction of the oxide the ratio $\mu_L/\mu_S = 0.08$ of fcc Co with an enhanced metallic surface contribution is measured.

One should note that steps a) to d) are crucial steps to remove unwanted surface contamination and to assure that magnetic dipolar interactions can be properly accounted for by determining the distribution of mean distances between particles. It has been shown that the shape of hysteresis loops of a Co nanoparticle sub-monolayer (coverage 80%) depends on the shape and size of the two-dimensional island shapes and separations [143]. Furthermore, the soft plasma treatment developed by H.G. Boyen *et al.* [141], [142] has the advantage to reduce oxide layers while keeping the number of metal atoms constant. This must be distinguished from a cleaning procedure using high energy (>100 eV) ion etching by Ar ions. In Fig. 13 the X-ray magnetic dichroic spectra are shown for the CoO@Co shell@core structure of the as prepared Co particles and of the ones after in-situ online rf-plasma cleaning. The change of the intrinsic magnetic properties is evident in form of the strong reduction of the ratio of orbital-to-spin magnetic moment when the oxide is removed, or, in other words, the Co^{2+} ions in the CoO shell are reduced to the metallic state. Similar behavior has been reported for colloidal FePt particles [144]. After the in situ plasma treatment residual hydrogen in the nanoparticles can be identified by certain features in the near edge region of absorption edges of $3d$ transition metals and removed by moderate annealing.

Summarizing this part one can state that preparation techniques have become available that allow the investigation of well-defined colloidal core-shell particle ensembles in the ligand-covered, surface oxidized state and in the clean metallic state free of unwanted surface modifications by element-specific synchrotron techniques [144].

The future challenge in magnetic core-shell particle characterization, however, is the observation of an element-specific magnetic response with nanometer spatial and nanosecond temporal resolution. Ideally, the spectroscopic and magnetic response of a single particle should be addressed. Several technical developments have been started in this direction which are covered in other sections of this review. Such studies have been partially successful on isolated Co nanoparticles where locally resolved absorption spectra have been recorded which qualitatively allow the distinction of different chemical spectroscopic responses of different particles [145]. However, a quantitative analysis has not been demonstrated yet. Even more difficult is the quantitative analysis of the magnetic moments in individual particles which still remains a goal out of reach today. A very interesting perspective arises by teaming up the synchrotron approach with analytical transmission electron microscopy, where already a number of interesting "proof-of-principle" studies have been performed on individual nanoparticles. Exit wave reconstruction techniques have been demonstrated allowing the determination of the separation of individual atomic columns with sub-angstrom resolution [146]–[148] and element specificity, which could allow the three-dimensional tomographic imagery of individual atoms in binary metal nanoparticles. Phase contrast techniques have been demonstrated which yield a magnetic contrast [149], [150] on the nm length scale and may be applicable to individual particles.

The dynamic magnetic properties of nanoparticle ensembles have been studied by ferromagnetic resonance (FMR) in the Gigahertz regime [134], and FMR techniques approaching 30 nm lateral resolution using a scanning tunnelling microscopy approach have been described [151]. With respect to synchrotron radiation first results on element-specific FMR detection [152]–[156] have been published and one may realistically hope that future developments will allow the imagery and element-specific investigation of dynamic and static magnetic properties of individual and dipolar coupled core-shell nanoparticles in the frequency and time domain with a spatial resolution on the 10 nm scale.

2) Magnetic Clusters: The second interesting class of magnetic nanoparticles comprises transition metal clusters. Small clusters are ideal systems to study emergent physical properties from atoms to solids. Experimentally they can be prepared with a precise number of constituents and consequently their physical properties can in principle be determined as a function of size. Furthermore, they present tractable systems for high-level

theoretical treatment which allows for in detail comparison of experimental results and theoretical predictions.

Typically one can identify two size regimes where the size-dependence of physical properties shows a rather different behavior. For "large" clusters physical properties evolve more or less monotonically towards their respective bulk values. This behavior is a consequence of the size dependence of the average coordination of the constituents and hence is closely related to the size dependence of the "surface-to-bulk" ratio of the clusters. In contrast, for "smaller" clusters one often observes non-monotonic changes of physical properties. This size regime which is the regime of so-called quantum-size effects is entered when the cluster size is comparable to the dimensions of the quantum mechanical wave functions relevant for a specific physical property. Consequently the transition between the two regimes depends on the material as well as the specific physical property.

While studies on isolated clusters are most interesting from a fundamental point of view, in view of possible applications studies of the size dependence of physical properties such as magnetism of clusters embedded in matrices or supported on a substrate are extremely important. Of course for these systems the interaction of the clusters with the surrounding environment has to be taken into consideration as an important parameter.

In the following we are going to discuss magnetic properties, i.e., magnetic moments, of small transition metal clusters (iron, chromium, cobalt) in a size regime below 20 atoms supported on ferromagnetic substrates (iron and nickel). These properties have been studied using X-ray absorption spectroscopy close to the transition metal $L_{2,3}$-edges with circularly polarized X-rays. The element specific magnetic moments have been determined exploiting sum rules in X-ray magnetic circular dichroism, i.e., the difference in X-ray absorption for right- and left-circularly polarized X-rays [157].

The mass selected transition metal clusters were generated using a UHV-cluster source [158] and deposited in-situ onto ultrathin ferromagnetic iron and nickel layers epitaxially grown on a Cu(100) surface. The ultrathin ferromagnetic films multilayers were prepared by evaporating the metals from a high purity sheet onto the clean copper crystal. The cleanliness and the quality of the films was checked with X-ray photoelectron spectroscopy (XPS) and low energy electron diffraction (LEED), respectively. Subsequently the ultrathin metal films in the thickness range of $\sim$3–5 monolayers (ML) for iron and $\sim$20 ML for nickel were magnetized perpendicular to the surface plane using a small coil. The magnetization of the metal films was monitored by recording Fe or Ni $2p$ XMCD spectra.

Before cluster deposition argon multilayers were frozen onto the metal surfaces at temperatures below 30 K. A layer thickness of $\sim$10 ML of Argon was used to ensure soft landing conditions [159] and the kinetic energy of the clusters was below 1 eV/atom. After depositing the clusters into the argon buffer layers, the remaining Argon was desorbed by flash heating the crystal to $\sim$80 K. It has been shown [159] that this procedure leads to deposition without fragmentation of the clusters. Low sample temperatures in the range of 30 K and low coverages of 3% of a monolayer were used to prevent cluster-cluster interaction. Every step of the preparation has been checked using X-ray Photoelectron Spectroscopy (XPS) and/or X-ray Absorption Spectroscopy (XAS). The measurements have been carried out at a base pressure $p < 3 \times 10^{-10}$ mbar. The X-ray absorption signal has been measured using the Total Electron Yield (TEY), i.e., the sample current.

For small iron clusters ($n_{\mathrm{atom}} = 2$–9) in contact with a nickel substrate ferromagnetic coupling of the clusters to the substrate has been observed [161], [162]. Theory predicts two-dimensional structures for these small supported clusters [163]. The analysis of the XMCD results reveals that the spin magnetic moments and the orbital magnetic moments of the iron clusters are enhanced compared to the respective values for iron bulk and surface. While the spin moments decrease nearly monotonically from the iron dimer to the $\mathrm{Fe_9}$-cluster and depend linearly on the average coordination of the iron atoms [163], the orbital moments show strong fluctuations as a function of size. Furthermore, the relative enhancement compared to bulk for the orbital moments is much stronger than for the spin moments. A detailed understanding of the behavior of the orbital moments requires explicit inclusion of correlation effects in electronic structure calculations [164].

Chromium on iron is a prototypical case for coupling between an anti-ferromagnet and a ferromagnet. Experimental studies on chromium atoms and clusters in the size range from 2 to 13 atoms supported on iron addressed the early stages of the magnetic coupling between chromium and iron [165]. Fig. 14 gives an example of the XMCD signals observed at the Cr edges. Theory shows that due to the competing intra-cluster and cluster-substrate exchange interactions which favor anti-ferromagnetic coupling within the cluster as well as between cluster atoms and substrate atoms complex noncollinear spin structures become important. For the chromium dimers the cluster-substrate coupling surprisingly leads to ferromagnetic chromium clusters which are anti-ferromagnetically coupled to the iron substrate. Addition of a third chromium atom leads to stabilization of an anti-ferromagnetically coupled collinear state for the trimer. Already for tetramers and pentamers the competing exchange interactions favor non-collinear spin structures where also the spin arrangement of the substrate atoms close to the clusters is affected. For even larger clusters experimentally a strong decrease of the average spin moment per chromium atom is observed indicating the increasing importance of anti-ferromagnetic coupling within the clusters.

It has been found experimentally that cobalt clusters supported on platinum show particularly high orbital moments and a very high magnetic anisotropy [166] which makes them interesting candidates for nanomagnetic applications. Therefore, several recent studies focus on pure cobalt clusters and cobalt-platinum alloy clusters supported on ferromagnetic substrates in an effort to disentangle the influence of substrate interaction and platinum coordination. The pure cobalt clusters supported on iron show an increase of the orbital moments from the single atom to the cobalt trimer. This behavior which is in contrast to the observations for cobalt on platinum is also found in the calculations for the same system and indicates the importance of cluster-substrate interaction [167]. In addition, the successive addition of platinum atoms to cobalt clusters is found to lead to very interesting non-monotonic changes in the orbital moments as a function of platinum coordination of the cobalt atoms [168].

In the short discussion above we have tried to exemplify the very intriguing magnetic properties of small deposited transition metal clusters. It is important to stress that to understand

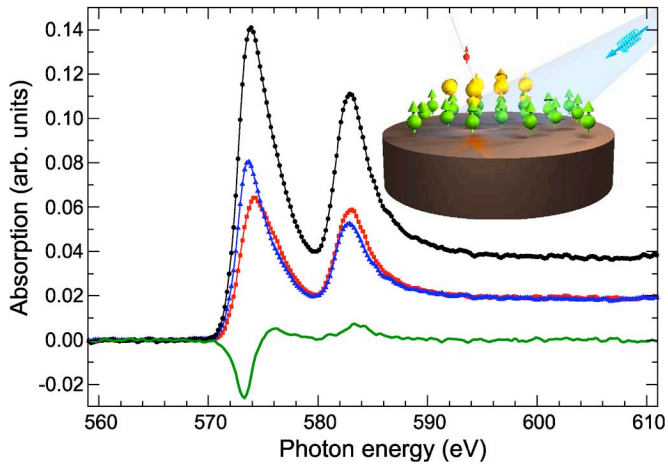

Fig. 14. X-ray absorption spectra of Cr_3-clusters on an iron substrate taken with two different helicities of the incoming X-rays (red and blue) together with the sum (black) and difference (green) spectra. The total Cr amount on the surface corresponds to only 3% of a monolayer coverage.

magnetic properties of size selected clusters in contact with surfaces in detail, experiments are required which determine spin- and orbital moments independently such as X-ray magnetic circular dichroism since quite often the size dependence of spin and orbital moments is very different. For small clusters every atom counts therefore mono-sized clusters have to be investigated. For the understanding of the evolution of the magnetic properties and especially the complex spin structures involved strong theoretical support is absolutely mandatory.

V. X-Ray Magnetic Scattering From Magnetic Thin Films, Multilayers, and Lateral Structures

X-ray magnetic circular dichroism, in particular, it's photon-in/photon-out variant belongs to a whole group of phenomena, the entirety of which is termed X-ray magneto-optics. It includes dichroic effects with circularly and linearly polarized light, and more exotic effects, such as magnetic birefringence and the Voigt effect (see Section V-B).

A. Resonant Magnetic Scattering

An X-ray magneto-optical approach, which is ideally suited to study layer stacks and multilayered samples is X-ray resonant magnetic scattering (XRMS). It combines the depth-resolving power of conventional X-ray reflectivity with the element-sensitivity and magnetic response of X-ray circular magnetic dichroism (XMCD). By observing the difference in the specular reflectivity for the two magnetization directions parallel and antiparallel to the photon helicity of circularly polarized X-rays in energy scans across the L or M-edges of $3d$ or $4f$ magnetic elements, respectively, one can derive the magnetization profile of a ferromagnetic thin film. This was explored by Kao and coworkers in the early nineties [17], [169] and has since been demonstrated convincingly for a number of single thin films and multilayers [170]–[173]. Applications to spintronic materials are discussed in [174]–[176].

1) Theoretical Background: An appropriate theoretical formalism to quantitatively treat XRMS is given by scattering approaches. Phenomenologically the X-ray scattering amplitude of an atom can be written in the form

$$f(\mathbf{q},\omega) = f^0(\mathbf{q}) + f'(\omega) + if''(\omega) \tag{8}$$

where $f^0(\mathbf{q})$ is the atomic form factor, i.e., the Fourier transform of the charge distribution, f', f'' are the real and imaginary parts of the dispersion corrections, and $\mathbf{q} = (4\pi/\lambda)sin(\theta)$ is the scattering vector. The dispersion corrections are energy dependent and take their extremal values at the absorption edges. If only dipole transitions are considered, the total elastic X-ray scattering amplitude can be written as [281]:

$$f = \left(\boldsymbol{\epsilon}_f^* \cdot \boldsymbol{\epsilon}_i\right) F^{(c)} + i\left(\boldsymbol{\epsilon}_f^* \times \boldsymbol{\epsilon}_i\right)\cdot \mathbf{m} F^{(1)} + \left(\boldsymbol{\epsilon}_f^* \cdot \mathbf{m}\right)\left(\boldsymbol{\epsilon}_i \cdot \mathbf{m}\right) F^{(2)} \tag{9}$$

with

$$F^{(c)} = -r_e Z + F^{(0)} \tag{10}$$

$$F^{(0)} = \frac{3\lambda}{8\pi}\left[F^1_{-1} + F^1_1\right] \tag{11}$$

$$F^{(1)} = \frac{3\lambda}{8\pi}\left[F^1_{-1} - F^1_1\right] \tag{12}$$

$$F^{(2)} = \frac{3\lambda}{8\pi}\left[2F^1_0 - F^1_{-1} - F^1_1\right]. \tag{13}$$

The unit vector $\mathbf{m}$ is oriented along the direction of the local magnetic moment, which defines the quantization axis of the system, and $\boldsymbol{\epsilon}_{i,f}$ designate the initial and final polarization vectors. The functions $F^{0,1,2}$ are strongly energy dependent resonant strengths for the dipole transitions. The first term in (9) refers to nonresonant and resonant charge scattering. The second term is first order in the magnetization and yields a circular dichroic signal, whereas the third term is second order in the magnetization causing linear dichroism.

In XRMS experiments with circularly polarized light usually the so-called L-MOKE geometry is employed, where the sensitivity is to the in-plane magnetization projected parallel to the scattering plane. The leading magnetic contribution to scattering arises from the $F^{(c)}F^{(1)}$ interference term between resonant charge and magnetic scattering.

For determining the reflectivity with left and right circularly polarized light the refractive index is required, which is related to the scattering amplitude through

$$1 - n(\omega) = \frac{r_e \lambda^2}{2\pi}\sum_i \rho_i f_i(\omega, q = 0). \tag{14}$$

Here ρ_i is the number density of species i in the sample and $f_i(\omega, q = 0)$ is the corresponding scattering amplitude in the forward direction $\mathbf{q}_0 = \mathbf{q}_f$. The refractive index is commonly split into real and imaginary parts according to

$$n_\pm = 1 - \delta_\pm + i\beta_\pm = 1 - (\delta \pm \Delta\delta/2) + i(\beta \pm \Delta\beta/2) \tag{15}$$

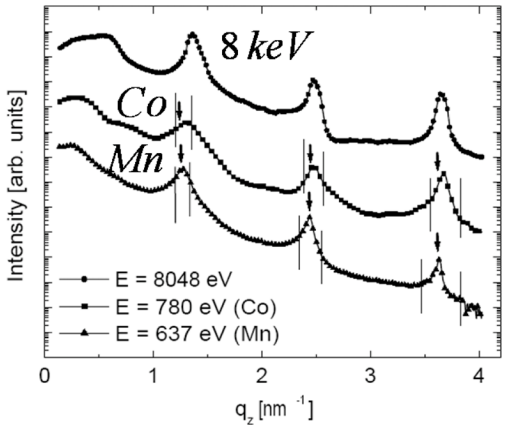

Fig. 15. Soft X-ray reflectivity from a Co_2MnGe/Au multilayer recorded with right circular polarized X-rays tuned to the L_3 absorption edges of Co and Mn. The top panel shows for comparison a reflectivity curve measured with nonresonant hard X-rays of 8 keV. (From Ref. [87]).

where δ and β are the dispersive and absorptive contributions, respectively, and $\Delta\delta$ and $\Delta\beta$ are the corresponding magnetic contributions to the refractive index. According to the optical theorem, the imaginary part β of the complex refractive index is directly proportional to the absorption coefficient μ : $\beta_{\pm} = \mu_{\pm}/(2q)$. Here q is the photon wave-vector and the index refers to right $(+)$ or left $(-)$ circular polarization. If the energy dependence of β is known, modified Kramers-Kronig relations can be employed, yielding the dispersive contribution δ to the refractive index.

Having the refractive index, XRMS allows for the determination of element-specific chemical and magnetic depth profiles of layered structures [172], [173], [178]. These profiles can be obtained by a quantitative analysis of specular reflectivity measurements, usually performed by numerical simulation. The calculation of the reflectivity needs a dynamical approach, as total and multiple reflection effects cannot be neglected in well defined films and multilayers. A matrix based formalism for magneto-optics with arbitrary magnetization direction has been developed by Zak *et al.* [179]–[181]. It offers the possibility to calculate the specular reflectivity without any restrictions to the geometry, assuming perfectly smooth interfaces. This theory was extended to allow for magnetic scattering from rough interfaces within the distorted-wave Born approximation by Lee *et al.* [182], [183].

For emphasizing the charge and magnetic contributions to the reflectivity, it is common practice is to plot the average sum $S = (I^+ + I^-)/2$ and the difference $A = (I^+ - I^-)$ as a function of the scattering vector or as a function of the energy, where I^+, I^- are the reflected intensities for right and left circularly polarized light. Assuming Born approximation, which is only justified for non-perfect multilayers and for scattering vectors far away from total reflection, these quantities have a straightforward physical interpretation, as pointed out by Kortright *et al.* [206]. The charge and magnetic complex atomic scattering factors may be written as $f_{c,m} = f_{1c,m} + if_{2c,m}$. Then the intensities in Born approximation can be expressed in the following form:

$$I^{+,-} = f_c^2 g_{c-c} + f_m^2 g_{m-m} \pm 2(f_{2c}f_{1m} - f_{1c}f_{2m})g_{c-m} \quad (16)$$

where $g_{c-c}, g_{m-m}, g_{c-m}$ are the charge-charge, magnetic-magnetic, and charge-magnetic correlation functions, respectively. In this expression the polarization factors in (9) are implicitly taken into account in the correlation functions. Thus the difference $A = 4(f_{2c}f_{1m} - f_{1c}f_{2m})g_{c-m}$ contains only the cross term with charge-magnetic cross-correlation and the sum $S = 2(f_c^2 g_{c-c} + f_m^2 g_{m-m})$ features the squared charge and magnetic amplitudes modified by their conjugated correlation functions. Furthermore, the intensity sum S using circular polarization is essentially the same as what one obtains for scattering with linear polarization [206].

In the following the XRMS method is exemplified by the discussion of recent work, including multilayers with Heusler alloys, dilute magnetic semiconductor films, and exchange biased magnetic heterostructures. Furthermore, in-plane correlations have been investigated by XRMS either for the investigation of magnetic domain structures and for the analysis of artificial lateral magnetic patterns.

2) Heusler Multilayers: As has been pointed out already in Section IV-C Heusler alloy films are presently of immense interest. The ferromagnetic order and the spin polarization relies on the ordered $L2_1$ structure with little tolerance for site disorder [186]. In spintronic devices, very thin films of Heusler alloys are used, bordering with nonmagnetic metals or with oxides for spin transport through quantum well potentials or through tunneling barriers, respectively. Thus, an important question to ask is to what extent the spin polarization in the Heusler alloy films is maintained up to the interface. To explore this question Grabis *et al.* [87] have grown Co_2MnGe/Au multilayers. They have recorded reflectivity curves using the ALICE system at BESSY II [187] with incident circularly polarized X-rays tuned to the corresponding L_2 and L_3 absorption edges of Co and Mn. The results are shown in Fig. 15 and are compared to nonresonant hard X-ray reflectivity data.

In the next step the scattering angles are fixed to one of the multilayer Bragg peaks and the incident photon energy is scanned across the region of the L_2 and L_3 absorption edges. These energy scans reveal the element-specific magnetic moment density profiles within the Co_2MnGe layers [87], [188].

Fig. 16 compiles the intensity sum $(I^+ + I^-)/2$ and the magnetically sensitive difference normalized by the sum, which is sometimes referred to as asymmetry, $(I^+ - I^-)/(I^+ + I^-)$, for the first three Bragg peaks at the Co $L_{2,3}$ absorption edges. These spectra are very rich in structure due to convolution of charge and magnetic intensity and therefore not easy to analyze. However, from the sign dependence of the asymmetry some straightforward conclusions can be drawn about the non-ferromagnetic layer thickness, as shown by model calculations in [87]. According to the asymmetry at the photon energy of 775 eV, which is $(+,-,+)$ for the first, second, and third order Bragg peak, respectively, one can conclude by comparison with model calculations that the non-ferromagnetic interlayer must

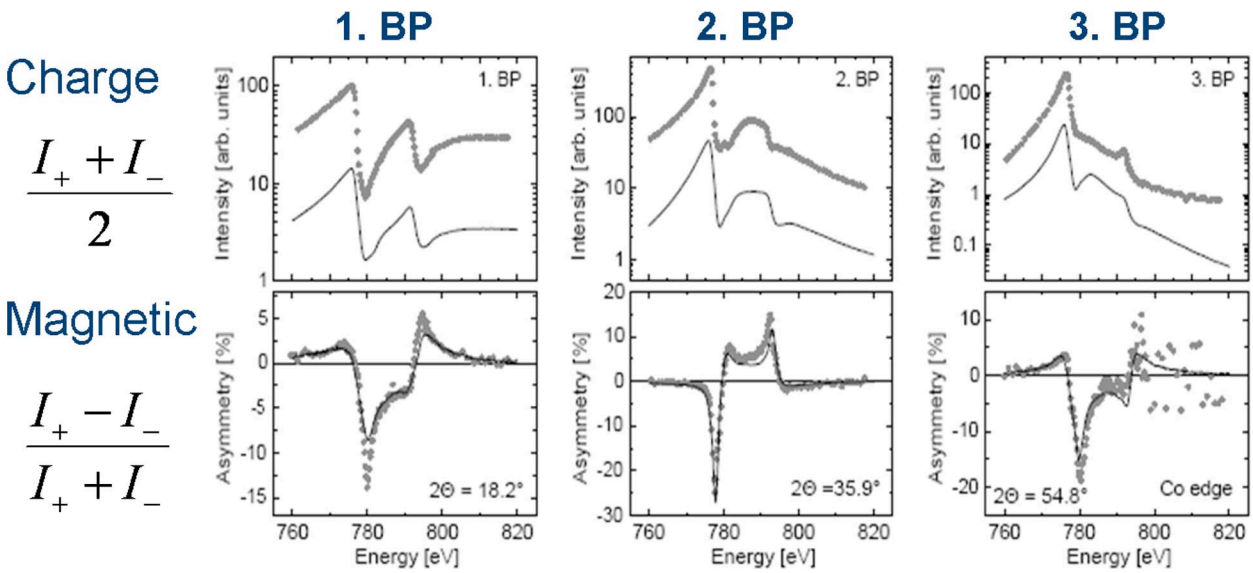

Fig. 16. Charge scattering and magnetically induced asymmetry for the first three Bragg peaks (BP) of the Co_2MnGe/Au multilayer measured close to the L_2 and L_3 resonances (From [87]).

have a thickness of about 1 nm. For a more refined estimate the energy-dependent intensities and asymmetries need to be modeled within a magneto-optical matrix formalism, as done for Co_2MnGe/Au in [87]. From this analysis Grabis *et al.* have found that the magnetic moment density profiles determined for Co and Mn are definitely different. Moreover, the magnetic profiles are more narrow than the chemical density profiles, indicative of reduced moments at the interfaces. For Co_2MnGe/Au multilayers at room temperature a non-ferromagnetic interface layer exists with a thickness of about 0.6 nm at the bottom and 0.45 nm at the top of the Co_2MnGe layers. Similar thicknesses of reduced magnetic moments have also been found in other Heusler multilayers with V spacer layers [177] and with Al_2O_3 and MgO tunnel barriers [189].

Magnetic multilayers have been studied in the past with XRMS methods for a number of reasons, the magnetization profile is one of them. Other issues are the interlayer exchange coupling and in particular the antiferromagnetic (AF) coupling across spacer layers. Tonnerre *et al.* [178] have studied a Ni/Ag multilayer, which shows antiferromagnetic coupling for a Ag spacer thickness of 11 Å. Tuning the circularly polarized incident beam to the $Ni - L_3$ edge, they observed in the diffraction pattern a Bragg peak at a q-value half that for the first Bragg peak from charge scattering. This is a clear sign for a doubling of the magnetic period compared to the chemical period. Doubling of the magnetic period due to antiferromagnetic order in magnetic multilayers has been seen before in neutron reflectivity experiments [190], [191], but this was the first time for XRMS. Subsequently a number or authors have studied AF coupled Co/Cu [171], [192], [193] and Fe/Cr multilayers [194], [195]. They have investigated, in particular, the field dependence of the half order and full order peaks using circular and linear polarized light tuned the respective L-edges of the magnetic layers. At the first Bragg peak a magnetic hysteresis is measured with circular polarization, which has the shape expected for a antiferromagnetically or biquadratically coupled multilayer and which corresponds exactly to the hysteresis measured by SQUID magnetometry. In contrast, at the half order position the hysteresis measured with circular or linear polarization has the shape of a GMR resistance [194]. This is typical for AF coupled superlattices, which cannot be determined with usual magnetometry measurements.

3) Magnetic Heterostructures and Spintronic Materials: The capability to analyze the magnetization profile into the depth of a layered heterostructure and to distinguish at the same time between different elements is of tremendous benefit for the analysis of exchange bias (EB) systems. EB systems consist of a ferromagnetic and antiferromagnetic layer, which share a common interface. After field cooling below the block temperature of the antiferromagnet, the magnetic hysteresis of the ferromagnetic layer becomes shifted by an exchange bias field, which is proportional to the F-AF interlayer exchange coupling and inversely proportional to the thickness and magnetization of the AF and F layer, respectively [255]. For reviews of the EB effect we refer to [197], [253], [254]. One important issue is the spin structure at the F/AF interface and the residual magnetization from uncompensated spins in the AF layer. Roy *et al.* have combined polarized neutron and resonant soft X-ray reflectivity to measure the depth profile of magnetization across the F-AF interface and inside the AF film of the Co/FeF_2 system [198]. In particular they have determined the profile of the pinned and unpinned magnetization within both layers. Close to the interface the unpinned moments in the AF layer are oriented antiparallel to the F layer and rotate antiparallel to the Co moments upon magnetization reversal. However, further away from the interface, all moments in the AF layer are pinned, which is required for providing an exchange bias effect. Using again XRMS methods and tuning to the Fe and Co edges of the Fe/CoO exchange bias system, Radu *et al.* [199] found in contrast to Roy *et al.* [198] that the uncompensated spins in the AF CoO layer have an orientation parallel to the Fe magnetization, but with a hysteresis that has a slightly higher

positive coercive field value at low temperatures than that of the Fe layer. These authors argue that the uncompensated spins are situated at the Fe/CoO interface and that they are responsible for the enhancement of the coercivity observed in the Fe layer with decreasing temperature. Without the uncompensated and rotatable spins at the interface the hysteresis of the Fe layer should be as narrow as for the unbiased Fe film. Most recently the magnetization profile of a perpendicular exchange coupled system was studied by Tonnerre *et al.* using soft X-ray resonant magnetic reflectivity [200]. The EB system investigated was a combination of an AF NiO/CoO multilayer with a ferromagnetic Pt-Co/Pt film on top. The sensitivity to the out-of-plane component of the magnetization vector arises from an off-diagonal term in the atomic scattering factor, which has a $\sin\theta$ dependence, where θ is the glancing incident angle to the film, indicating that sensitivity increases at higher θ values. Using this method the magnetization profile of Co from Co in the Co-Pt film and to Co in the oxide multilayer has been determined in the unbiased state and the magnetization profile has been determined. The complexity of the analysis is enhanced because of Co in this system being in a metallic and in a 2^+ ionic state [200].

Another important class of spintronic materials are dilute magnetic semiconductors where a small fraction of host cations are substitutionally replaced by magnetic transition metals [201]. Doped TiO_2 is one of the promising candidates for room temperature ferromagnetism. The element specific magnetic properties of Co-doped TiO_2 have recently been studied by Nefedov *et al.* [196]. The sample has the rutile structure and the doping was achieved by ion implantation with a dose of 1.50×10^{17} ions/cm^2. The magnetic state of the implanted Co ions was investigated using X-ray resonant magnetic scattering at room temperature. Fig. 17 shows the energy dependence of the scattered intensity at the Co $L_{3,2}$ edges for a fixed reflection angle of $2\theta = 8.2°$. A clear difference in the energy scan between the right and left circular polarized X-rays can be recognized, indicative for ferromagnetism at room temperature. In the lower panel of Fig. 17 is shown the asymmetry ratio. As the X-ray reflectivity from this sample has little structure, the asymmetry ratio is practically identical to the XMCD signal. It is well known that in the case of metallic films the resonant scattering peak consists of a single component. However, in Fig. 17 a fine structure of the Co L_3 peak at $E = 780$ eV can be recognized. This fine structure is similar to that observed before for CoO films and is indicative of Co being in a 2^+ ionic state on substitutional lattice sites in the TiO_2 host. The asymmetry can be used to record the magnetic hysteresis of the sample. This is shown in Fig. 18. The Co dopant exhibits the same square hysteresis as has been observed previously using magneto-optic Kerr effect. In addition it was observed that oxygen becomes polarized after Co implantation expressed by an albeit weak XMCD signal and a magnetic hysteresis that matches the Co hysteresis in shape and coercive fields. Thus it appears that the oxygen polarization is essential for the formation of a long range ordered ferromagnetic ground state in $Ti(Co)O_2$.

4) Lateral Magnetic Structures: In addition to the sensitivity of chemical and magnetic profiles normal to the film planes

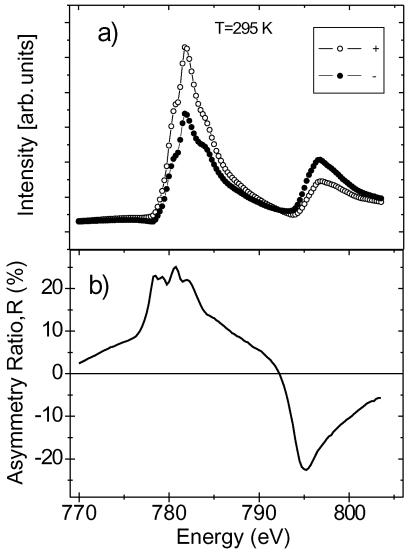

Fig. 17. (a) Energy dependence of scattering intensities at the Co $L_{3,2}$ doped by ion implantation in a host matrix of rutile TiO_2; (b) corresponding asymmetry ratio (XMCD signal) (from Ref. [196]).

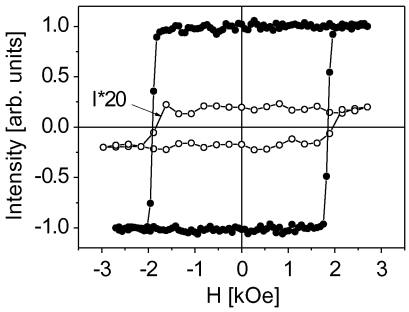

Fig. 18. Hysteresis curves measured at Co L (closed symbols) and O K (open symbols) edges at $T = 30$ K. The intensity of the oxygen signal has been multiplied by a factor of 50 for clarity. (From Ref. [196]).

and parallel to the scattering vector q_z, there is also much interest in gaining information on in-plane ordering and correlation lengths. There are two routes to this information: either the off-specular intensity is scanned in reflection mode, or the small angle scattering intensity is collected in transmission mode. In either case it is important that some component of the scattering vector points parallel the in-plane direction, q_x. In a transmission setup, as shown in Fig. 19, it is possible to obtain detailed information about the lateral heterogeneity of thin film systems, such as for example chemical and magnetic grain sizes and grain size distributions [202], [203], chemical segregation processes [204], nanoparticle arrays [206], magnetic domain structures [207], [209], [275], [283] and otherwise laterally nanostructured systems. The different scattering terms allow probing both, electron density variations as well as variations in the magnetic moment density. The resolution of the scattering studies is only limited by the wavelength, such that in the soft X-ray range heterogeneity on the length scale of a few nanometers up to one micrometer can be investigated [206]. However, this approach usually requires sample deposition onto Si_3N_{4-x} membrane substrates that are commercially available today, but do not allow easily the deposition of single crystalline thin films. Fig. 19

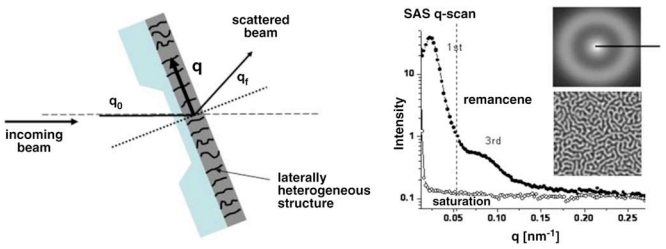

Fig. 19. Left: geometry for small angle resonant X-ray scattering in transmission geometry. The thin film sample (dark grey) has been deposited onto a Si_3N_{4-x} membrane substrate (light blue). The soft X-ray beam is coming in from the left and is scattered by the lateral heterogeneous nanostructures of the thin film. Notice that the scattering vector q lies within the film plane rather than perpendicular to it as common in reflection geometry. Right: small angle scattering data at the $Co - L_3$ absorption edge from perpendicular magnetic stripe domains. The lower inset shows a 5 μm^2 MFM image of the domain structure that was investigated by scattering. Upper inset: corresponding 2-D SAS intensity as detected with a CCD camera. The solid symbols in the $I(q)$ plot are a one dimensional radial scan through the diffraction ring at remanence as indicated by the black line in the CCD image. Open circles show the diffraction pattern In saturation. (From [208]).

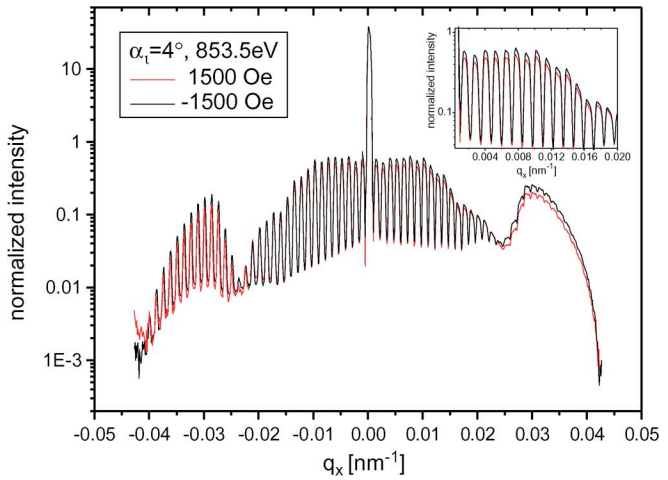

Fig. 20. In-plane q_x scan from a lateral periodic array of $Ni0.80Fe_{0.20}$ rectangular bars. The intensity modulation is due to the shape factor convoluted with the Yoneda wings [212].

shows in the left panel the schematics for small angle resonant magnetic X-ray scattering (SAS) in transmission geometry. In the present case this set-up was used for the analysis of Co/Pt nanostructures with perpendicular anisotropy, which develops in the remanent state a laterally periodic stripe domain structure. The upper right inset exhibits the two dimensional SAS intensity as detected with a CCD camera that was positioned behind the membrane sample. In the center the transmitted direct beam is visible, while the diffraction ring originates from the regular domain spacing. Here the radius of the ring is inversely proportional to the domain periodicity and the width of the ring is a measure for deviations from this periodicity (the sharper the ring the more well defined is the periodicity). The solid symbols in the intensity versus scattering vector q plot are a one dimensional radial scan through the diffraction ring at remanence as indicated by the black line in the CCD image. The q-range limit that has been probed by the CCD image is marked by a dashed line in the plot. However, the photo diode detector on a rotation arm provides access to radial profiles up to much higher q values and reveals 1st and 3rd order reflections from the domains. In saturation the diffraction ring vanishes, since all domains are annihilated and the sample becomes magnetically uniform with no SAS [202], [209].

Artificial lateral magnetic patterns have been studied by a number of authors using soft X-ray resonant magnetic scattering. In q_x scans Bragg reflections occur due to the in-plane periodicity. If the in-plane elements interact by magnetostatic stray fields, antiparallel alignment may occur, which is recognized by half order lateral Bragg peaks. Magnetic coupling in Co/Pt nanolines together with their AF coupling and evolution in a magnetic field was investigated by Chesnel *et al.* [211], magnetic multilayer reflection gratings were investigated by Michez *et al.* [210], and Remhof *et al.* studied periodic arrays of magnetic dipoles on a 5×5 μm square grid, measuring q_x Bragg peaks up to high orders and measuring the magnetic hysteresis at their diffraction orders [212]. The X-ray scan is shown in Fig. 20. Van Kampen *et al.* have investigated $Ni_{0.80}Fe_{0.20}/Al_2O_3$ multilayers shaped into an array of circular nanopillars [213]. The diameter and thickness of the magnetic islands and the Al_2O_3 spacer layer were chosen such that an antiferromagnetic coupling occurs in remanence. Nevertheless, half order peaks could not be discerned in $q_x - q_z$ scans, most likely due to a randomness in the staking sequence among the pillars.

Lateral periodic structures are just a special case of a highly ordered in-plane correlation function. The more general case are films and multilayers with an in-plane interfacial roughness with a less well specified and ordered height-height correlation. The distinction of structural roughness from magnetic roughness has been of much interest over the past years, and soft X-ray resonant magnetic scattering is a favorable method for the analysis of the magnetic roughness. This is mainly due to the fact that with soft X-rays the scattering angle is rather high and the q_x—range is large before it becomes obscured by the sample horizon. However, in contrast to spin flip neutron reflectivity, soft X-ray resonant magnetic scattering is never purely magnetic, the difference $I^+ - I^-$ always contains the charge-magnetic cross correlation. Nevertheless, detailed studies of the magnetic roughness have been performed in a number of works [87], [214]–[217], and it has in general been concluded that the charge-magnetic roughness is 'smaller' than the charge (or structural) roughness, meaning that the former has a longer in-plane correlation length. From a quantitative point of view this can be easily understood because the magnetic correlation of structural grains is enhanced by exchange coupling and demagnetization fields. While the charge-magnetic roughness is analyzed, in general, within the Born approximation, which may in most cases be sufficient for a qualitative analysis, Lee *et al.* have provided a description for the in- and out-of-plane correlation from magnetically rough interfaces based on the distorted wave Born approximation [182], [183].

Concluding, X-ray resonant magnetic scattering is a powerful method for the investigation of magnetic films and multilayers. Aside from the combination of depth dependence with

element-selective magnetic information, XRMS has some further important advantages. Its information depth is considerably larger than for XMCD, the latter one usually restricted to the top 2 nm, depending on the recording method, and it has a much higher spatial resolution into the depth of the layer and in the lateral direction, which is on the order of the wavelength used. Thus the spatial resolution reached by scattering is considerably higher than the one obtainable by X-ray microscopy or PEEM. Furthermore, as XRMS is a photon-in—photon-out scattering method, it is less surface sensitive than XMCD and can also be studied under non-UHV conditions. Moreover, the samples of interest can be measured at remanence as well as at high magnetic fields and magnetic hysteresis curves can be recorded without problems.

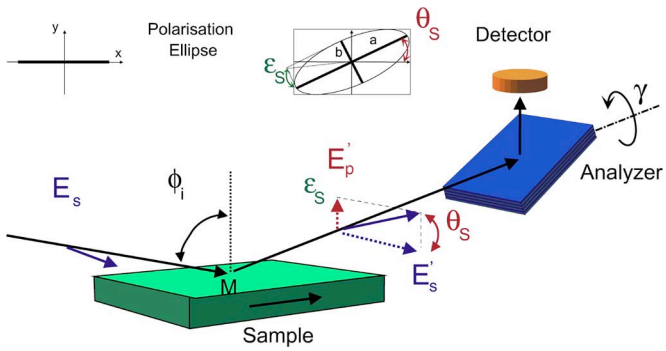

Fig. 21. Schematic set-up for soft X-ray polarimetry. The polarization state of the radiation after its interaction with the sample is determined through a rotatable analyzer element.

B. X-Ray Magneto-Optical Polarization Spectroscopy

The XRMS approach discussed above is just a special type of a variety of magnetically sensitive photon-in/photon-out spectroscopies, which may be grouped under the label of magneto-optical polarization spectroscopy. As already pointed out in the introduction, these magneto-optical (MO) phenomena have a long scientific history, starting with the discoveries of Michael Faraday. In 1845 he observed the rotation of the polarization plane of linearly polarized light upon transmission through a magnetic material, an effect which since has become known as the Faraday effect. Subsequent observations of various other MO phenomena using polarization detection, such as the Kerr and Voigt effects, were reported in the nineteenth century (see e.g. [218]). Building on this broad base of knowledge, MO polarization spectroscopy in the soft X-ray regime has emerged as a successful and complementary tool for the element-selective study of magnetic materials during the last few years, [219]–[221].

In the sequel of the early discoveries, the experimental procedure which was adopted mostly for MO measurements in the optical regime, did not simply measure the intensity—as in the example of XRMS—but rather involved a polarization analysis of the light after its interaction with a magnetic material. For a complete polarization analysis two optical elements, the polarizer and the analyzer, have to be rotated about the light axis, while the light intensity is recorded [222], [223]. Such an analysis provides the two defining quantities for the light's polarization state, namely, the intensity of the light and its phase. This information can be expressed by the four Stokes parameters S_0 (intensity), S_1, S_2 (degree of linear polarization with respect to planes which are rotated by 45° to each other) and S_3 (degree of circular polarization). The total degree of polarization is $P = (S_1^2 + S_2^2 + S_3^2)^{1/2}$. If the light is completely polarized $(P = 1)$ the polarization analysis can be performed by using only one optical element, the analyzer (see Fig. 21).

The Stokes parameters can be re-expressed as two angles, defining the tilt θ_s of the light's polarization ellipse and the degree of its ellipticity ε_s (see Fig. 21). From this data set the complex optical constants of the investigated material can be deduced directly and completely. Access to only one of these two MO quantities can be obtained by the widely used and technically simpler intensity measurement. The magnetic circular and linear dichroism (MCD and MLD) and their X-ray equivalents XMCD and XMLD are representatives of this approach.

While MO effects are usually small in the visible energy range, larger effects are observed in the X-ray range. In particular in the soft X-ray regime huge effects are found due to the resonant enhancement occurring at the $2p$ edges of $3d$-transition metals [10] and at the $4d$ edges of rare-earth elements [224]. Thus, the development of polarization sensitive techniques in the X-ray range opens up new avenues for element-selective investigation of magnetic materials, but it has turned out that this is not an easy task. In the hard X-ray range above 2.5 keV, diffraction from Si, diamond or graphite single crystals in Bragg or Laue-geometry is applied [225], [226]. But for the scientifically interesting soft X-ray regime the production of suitable optical elements is still a technological challenge. Presently, artificial multilayer (ML) systems with extremely small periods are used as polarization analyzers. These are working at the Bragg angle, which must be close to the Brewster angle near 45°. According to the Bragg equation the period thickness has to be matched to a small energy range of interest. This means that different MLs with appropriate period thicknesses have to be produced to cover the complete soft X-ray range. State-of-the-art systems comprise multilayers with a period thickness of about 1.1 nm [219], [223]. These are optimized for the Fe $2p$ edge, but can be operated even at higher energies up to about 850 eV, however, with a reduced performance. For energies around the $3d$ shells of rare earth elements MLs with an extremely small period around 0.7 nm have still to be developed.

Exploiting the X-ray Faraday effect the complete sets of MO constants of Fe, Co, and Ni have been determined experimentally across the $2p$ and the $3p$ edges [221], [227] and where found to confirm theoretical calculations [228]. Whereas the Faraday effect commonly refers to a transmission geometry, an analogous polarization effect observed in reflection is the longitudinal Kerr effect (L-MOKE) [229]. In this case, linearly s-polarized light interactions with the magnetization oriented within the scattering plane (Fig. 21). Upon reflection the changes of the polarization state are quantified θ_s and ε_s. If only the magnetically induced intensity changes of the reflected light are of interest, however, we recover the XRMS approach discussed in the previous section.

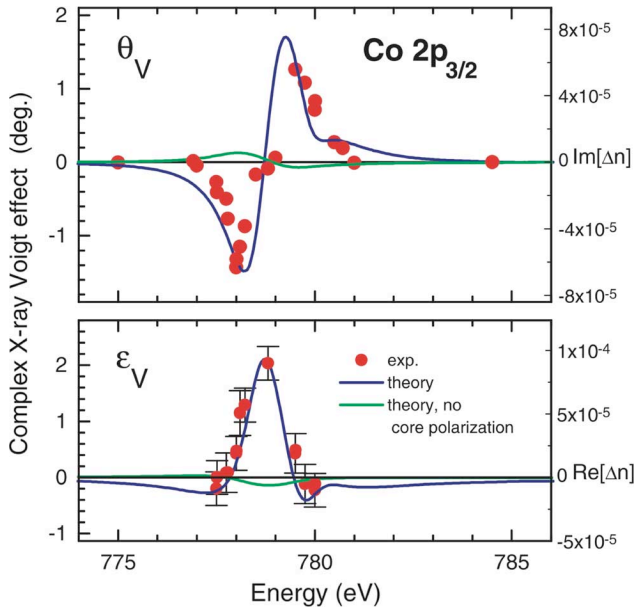

Fig. 22. Calculated and measured X-ray Voigt effect at the Co L_3-edge [220]. Top: experimental Voigt rotation θ_V (•) and calculated Voigt rotation (lines). The blue curve gives the Voigt rotation computed with core exchange splitting of the $2p_{3/2}$ core states, while the green curve shows the Voigt rotation obtained without core polarization. Bottom: likewise, but for the Voigt ellipticity ε_V. After [220].

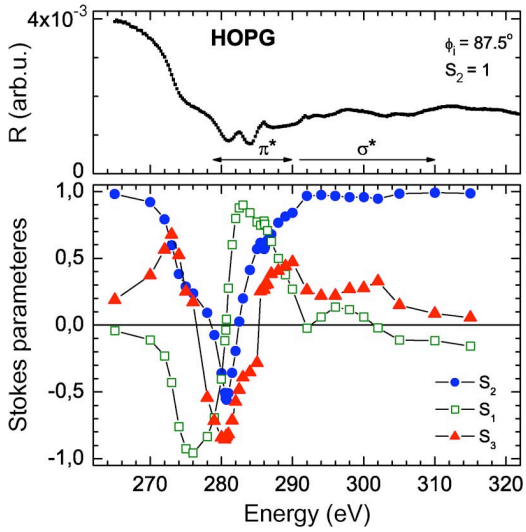

Fig. 23. Reflectivity (top) and measured Stokes parameters S_1, S_2, and S_3 (bottom) of the radiation reflected from graphite at the C K-edge [229]. The X-ray birefringence (or anisotropic scattering) is shown by the dramatic change of the Stokes parameters between 270 and 290 eV (From [232]).

A novel MO effect in the soft X-ray regime, which was discovered by means of the full polarization analysis, is the Voigt effect [220]. In the optical range, the Voigt effect is a only tiny effect which is proportional to M^2, where M is the sample magnetization. It is detected using linearly polarized light, which is at normal incidence to the surface, while the light's polarization plane is at 45° with respect to the in-plane magnetization direction. Upon transmission, the polarization plane rotates by the Voigt angle θ_V and the light acquires an ellipticity ε_V (Fig. 22). It can be shown that for cubic materials the Voigt effect is related to the magnetic birefringence in the index of refraction [230]

$$\theta_V - i\varepsilon_V \approx \frac{\omega t}{2ic}[n_{\|} - n_{\perp}] \tag{17}$$

where t is the thickness of the film, $n_{\|}$ and $n_{\perp}$ are two refractive indices corresponding to the propagation of electric field modes which have $E \parallel M$ or $E \perp M$, respectively. *Ab initio* calculations of the X-ray MO Voigt spectra revealed its interesting physical origin [220]. The Voigt effect appears primarily because of the core exchange splitting (CEX) of the $2p$ core levels, which is indeed a small splitting of the j_z sublevels by about 0.27 eV in Co. Calculations of the Voigt effect without the CEX yield a vanishing result. A second quantity, which largely determines the shape of the Voigt spectrum is the crystal field [231]. Interestingly, both quantities can be safely ignored for X-ray MO effects that are *linear* in M, such as the XMCD [231].

It should be noted, however, that polarization effects do not always have a magnetic origin. As an example, we have employed soft X-ray polarimetry to investigate nonmagnetic, grazing incidence scattering from graphite planes at the carbon K-edge [232]. The experiments revealed an unexpectedly large change in the Stokes parameters measured at the K-edge (see Fig. 23). The dramatic changes in the Stokes parameters imply that the X-ray radiation changes, upon reflection from graphite, from linear to circular polarization. The observed changes are unusually large and due to X-ray birefringence, which in turn is caused by the layered structure of graphite. It is noteworthy, first, that a similarly large effect does not exist in the optical regime, even though there optical birefringence is also present. Second, a plain detection of the intensity of the scattered radiation would not be capable of providing the same information as the Stokes polarimetry [232].

From the various examples it is obvious that among the available spectroscopies resonant magnetic reflectometry with circularly and linearly polarized X-rays on single layers as well as on MLs is a very promising spectroscopy, since the resonantly enhanced cross sections at absorption edges lead to large magnetic responses in the intensity (XRMS) and/or the polarization (polarization spectroscopies), which can easily exceed those observed in conventional XMCD absorption experiments [233]. The large dichroic effects observable in reflection over a wide range of incident angles as well as their structural sensitivity to layer thickness and interface roughness, designates these spectroscopies to be ideally suited for the study of magnetic depth profiles of magnetic films or MLs. It would be advantageous to combine resonant magnetic reflectometry with polarization analysis, because it permits the complete determination of the real and imaginary parts of the MO constants, something which is not possible by simple intensity measurements. In all reflection measurements, however, one always measures a combination of MO constants, therefore a polarization analysis is needed for the entanglement of the different contributions of the MO constants. A next practical step would thus be to establish X-ray Kerr effect measurements in longitudinal and polar geometry, which in addition could be combined to an X-ray vector magnetometry.

While the Kerr effect enables the investigation of ferromagnetic samples, the Voigt effect is a powerful tool to investigate antiferromagnetic samples, since it is quadratic in the magnetization. This has been shown for thin films in transmission [220]. Because most samples like industrial relevant antiferromagnetic devices cannot be investigated in transmission, however, the Voigt effect in reflection would be a promising technique with the strength of all above mentioned features of reflection spectroscopy. It has already been shown that buried antiferromagnetic layers could be successfully studied with resonant magnetic reflectometry [234], but this has not yet been combined with polarimetry.

Soft X-ray polarization spectroscopy may, furthermore, answer important questions concerning the occurrence of ferromagnetism in carbon [235], graphite, or in other materials like TiO_2. As has been outlined above, soft X-ray polarimetry has been applied already to nonmagnetic graphite and a certain care has to be exercised when interpreting the results in terms of magnetic and nonmagnetic contrast mechanisms.

VI. Magnetic Imaging

A ferromagnetic system is usually not homogeneously magnetized—except for very small particles below a critical size. It can lower its total energy by the formation of a domain structure, which may be strongly influenced by the shape of the sample, by defects or by strain. As a consequence, in most samples we will find a more or less complicated micromagnetic structure. This situation holds not only for ferromagnets, but for all kinds of magnetic systems. The formation and dynamic response of this micromagnetic structure is still a topic of fundamental research.

On the other hand, micromagnetism has an enormous technological relevance. Reliable switching of magnetic nanostructures from one remanent state to another is the basis of nonvolatile data storage on magnetic hard drives. The continuous push towards increased storage densities over the last fifty years of hard disk drive development has led to smaller and smaller magnetic bit sizes, which are now (in all three spatial dimensions) clearly in the nanometer regime. New concepts such as hard drive storage media with perpendicular anisotropy including exchange spring media, [236] patterned media, [237], [238] thermally assisted recording, [239], [240] and nonvolatile magnetic memories such as magnetic RAM (MRAM) [241] or solid state devices such as Racetrack Memory [242] promise to further reduce bit size and/or to add new functionality. The technological development is intimately coupled to material science questions and to understanding basic scientific questions on the magnetic interactions between individual nanostructures and within them, e.g. at internal interfaces of complex multilayer elements such as antiferromagnetically coupled media or exchange spring structures [243]. In order to improve the storage bit addressability, it is important to correlate the magnetic switching field of individual nanostructures with structural parameters such as defects, heterogeneities and overall bit geometry. Being able to "watch" nanomagnetic bits switch by high resolution magnetic imaging is clearly important in this context in order to address both fundamental and applied scientific questions.

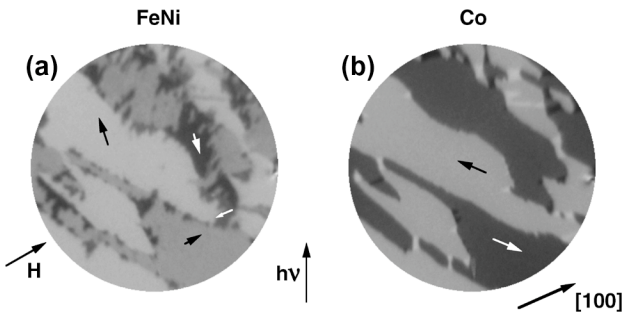

Fig. 24. Example of layer-resolved magnetic domain imaging by XMCD-PEEM. (a) and (b) show the magnetic domain images of the FeNi and the Co layer, respectively, of an FeNi/Cu/Co trilayer on FeMn/Cu(001) after application of an external magnetic field of 340 Oe in the direction indicated by "H".

Therefore, various magnetic imaging approaches employing XMCD as a magnetic contrast mechanism have become widely used during the last decade. Some of these can even be conveniently used to address the domain structure in antiferromagnets, which is otherwise accessible only by very few experimental techniques. X-ray magnetic linear dichroism provides a unique solution to this problem, as we will demonstrate below.

A. Magnetic Coupling in Layered Systems

Nearly all of the most exciting new discoveries in thin film magnetism are observed in multilayered structures in which two or more magnetic layers are separated by nonmagnetic or antiferromagnetic spacer layers. To obtain microscopic magnetic information about the different magnetic layers and their mutual interaction separately and in a simple way is thus crucial for the microscopic fundamental investigation of such structures. With XMCD-based techniques this is possible by selecting the photon energy corresponding to the elemental core-valence excitations. Lateral resolution can be obtained if photoelectron emission microscopy (PEEM) is used for the electron yield detection of X-ray absorption [14]. This allows the layer-resolved visualization of magnetic domain patterns at surfaces and in buried layers [244], [245].

An example of layer-resolved magnetic images, taken at an FeNi/Cu/Co trilayer deposited on FeMn/Cu(001) [246] is given in Fig. 24. The trilayers were grown by thermal evaporation on a Cu(001) single crystal substrate in zero external magnetic field. Domain images were acquired *in-situ* in the same ultrahigh vacuum system using an electrostatic Focus IS PEEM, which has been described in [244], [247], [248], and circularly polarized undulator soft X-ray radiation from BESSY. The images are presented as grayscale-coded absorption asymmetry for opposite helicities of the circularly polarized X-rays at the L_3 absorption maxima, i.e., the difference of absorption images acquired with opposite helicities divided by their sum.

Fig. 24 shows the layer-resolved magnetic domain structure after application of an external magnetic field of 340 Oe along the direction indicated by "H". Image (a) was obtained by tuning the photon energy to the Fe L_3 absorption edge, and thus represents the domain image of the FeNi top ferromagnetic layer, image (b) was acquired with the photon energy tuned to the Co L_3 absorption edge and shows the domain image of the

Co bottom ferromagnetic layer. The domains in the Co layer are mainly oriented along two opposite $\langle 110 \rangle$ directions as indicated by arrows, namely along $[1\bar{1}0]$ and $[\bar{1}10]$, corresponding to dark gray and lighter gray contrast, respectively. This pattern in the Co layer was not changed by the application of the 340 Oe external field. The domain image of the FeNi layer (a) shows a qualitatively similar pattern, but with different contrast. An analysis reveals that here the magnetization directions in the different domains are along the $\langle 100 \rangle$ in-plane directions, as indicated by arrows in some domains. The comparison with the domain image of the Co layer (b) shows that in most places the magnetization directions of the two magnetic layers include an angle of 45°. This is explained by a different anisotropy energy in the two layers, and a parallel interlayer coupling [246]. Because of the direction of the applied field H, the magnetization in the FeNi layer points mainly along [100] and [010].

The interesting point is that the positions of the domain boundaries of the Co layer are still visible in the FeNi image, where they are decorated by small domains with a darker contrast. This is an indication of a locally enhanced interlayer coupling at the domain walls of the Co layer. Such a local interlayer coupling has also been observed by XMCD-PEEM in Co/Cu/Ni trilayers, and is attributed to the interaction between the layers by the magnetostatic stray field emanating from the domain walls [249]. Such a micromagnetic coupling between magnetic layers across nonmagnetic spacer layers competes with the well-studied indirect oscillatory magnetic interlayer exchange coupling [250]–[252], and may play a crucial role for magnetoresistive applications of reduced lateral size.

The recent interest in the magnetic coupling between antiferromagnetic (AF) and ferromagnetic (FM) materials is motivated by the quest for fundamental insight into the phenomenon of exchange bias [253], [254]. This effect, the discovery of which dates back to the 1950s [255], manifests itself in a shift of the magnetization curve along the field axis. Nowadays the exchange bias effect is employed in a variety of devices, such as sensors or hard disk read heads, based on magnetic thin films [256], [257]. A detailed fundamental understanding of the magnetic AF-FM interaction, however, is still elusive. This is in part due to the insufficient characterization of the interface structure in the polycrystalline materials that are typically used to study exchange bias. In AF materials the direction of the atomic magnetic moments varies on the length scale of atomic distances, leading to zero net magnetization if averaged over a few lattice constants. Atomic-scale control and characterization of the AF/FM interface is thus essential for a fundamental understanding of the magnetic interaction between AF and FM materials.

Layer-resolved magnetic imaging of trilayers, in which two ferromagnetic layers are coupled across an antiferromagnetic layer, can deliver useful insight into the AF-FM coupling. Particularly useful for such studies are samples in which one or two of the layers are deposited as small wedges, suitable for imaging within the field of view of the microscope. This can be achieved by placing a slit aperture at a certain distance in front of the sample surface, and rocking the whole sample-mask assembly around an axis in the surface plane during film deposition, as described in [258]. In this way it is possible to access the thickness dependence of the coupling in a two-dimensional parameter space.

Fig. 25 shows an example of a trilayer on a Cu(001) substrate in which antiferromagnetic FeMn is sandwiched by two ferromagnetic layers, a Co layer at the bottom, and a Co/Ni hybrid layer at the top. Panel (a) shows a sketch of the wedge geometry. The thickness of the bottom Co layer increases from left to right up to 8 atomic monolayers (ML), and then stays constant. The thickness of the antiferromagnetic FeMn layer varies from bottom to top. Panel (b) shows the magnetic domain image of the as-grown Co bottom layer, panels (c) and (d) the domain images obtained at the Co and Ni absorption resonances, respectively, after deposition of the complete structure. Because both the bottom and top ferromagnetic layers contain Co, image (c) is a superposition of the magnetic domain patterns (b) and (d), while panel (d) represents the top layer only. Alternating regions of parallel and antiparallel coupling across the FeMn layer are indicated by couples of parallel and antiparallel arrows in (c). They alternate with a 2-ML period as a function of FeMn thickness, but also exhibit an interesting saw-tooth-like behavior on the thickness of the bottom Co layer. The latter represents the dependence on the interface morphology. It is modulated by the thickness, and hence the atomic layer filling, of the bottom Co layer.

From these measurements and supporting magneto-optical Kerr effect experiments, the following picture could be deduced [259]: First, to have a significant magnetic interaction between the ferromagnetic and the antiferromagnetic layers, steps of single atom height at the interface are required. Perfectly flat regions do not contribute. This follows from the absence of 90° coupling, which would otherwise be expected at FeMn thicknesses close to $n+0.5$ ML thicknesses with n an integer number [260]. Also the influence of the Co bottom layer thickness on the sign of the coupling is not compatible with flat regions being the dominant source of the antiferromagnet-ferromagnet coupling. Second, the coupling is higher if these monatomic steps are laterally confined at small islands. Larger islands or elongated steps lead to a weaker coupling. The coupling is mediated by uncompensated spins of the antiferromagnet at monatomic step edges at the interface. Uncompensated atomic moments at step edges are responsible for the magnetic coupling to the ferromagnet.

These results indicate that, in general, the interface coupling can be enhanced by the controlled incorporation of atomic-level roughness features with small lateral size. With the forthcoming advent of atomic-scale manipulation in nanotechnology, this may be a feasible way to controllably modify the coupling strength in ferromagnetic-antiferromagnetic systems.

B. Heteromagnetic Interfaces in Oxides

In the metallic interfaces discussed in the previous paragraph the electronic structure has a strongly itinerant character with direct exchange interactions. This situation changes, however, if a metal and an insulator or two insulators are brought into contact. In this context, oxides are particularly interesting, as this

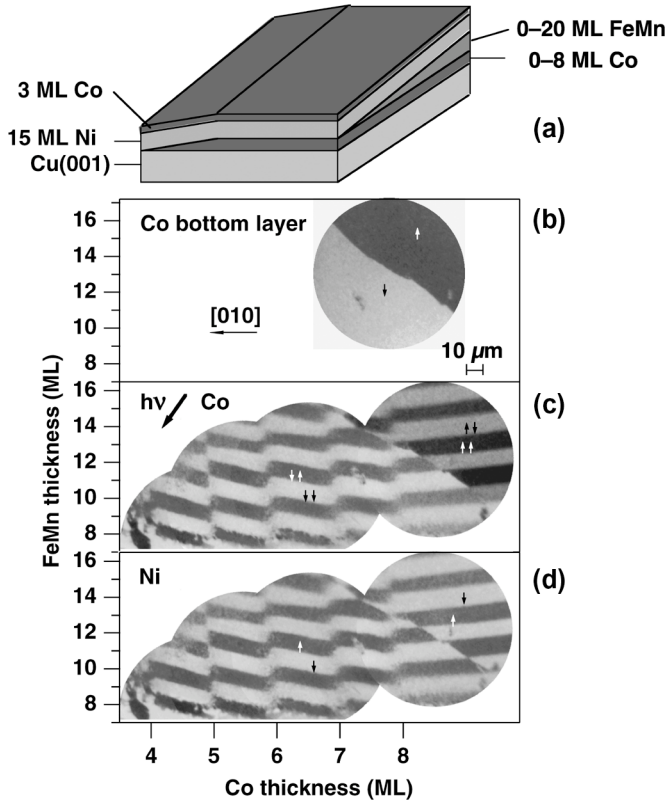

Fig. 25. (a): Geometry of a crossed double-wedge sample. Antiferromagnetic FeMn of varying thickness is sandwiched between ferromagnetic layers consisting of Co at the bottom and Co/Ni at the top. (b): Domain pattern of the Co bottom layer. Bright and dark regions correspond to magnetization direction down and up, respectively. (c): Element-selective domain image of the complete sandwich structure, acquired at the Co L_3 edge. Bright and dark regions result from a superposition of magnetization directions of Co in the bottom and top layer, indicated by couples of arrows. (d): Element-selective domain image of the top layer, acquired at the Ni L_3 edge. Bright and dark regions correspond to magnetization direction down and up, respectively.

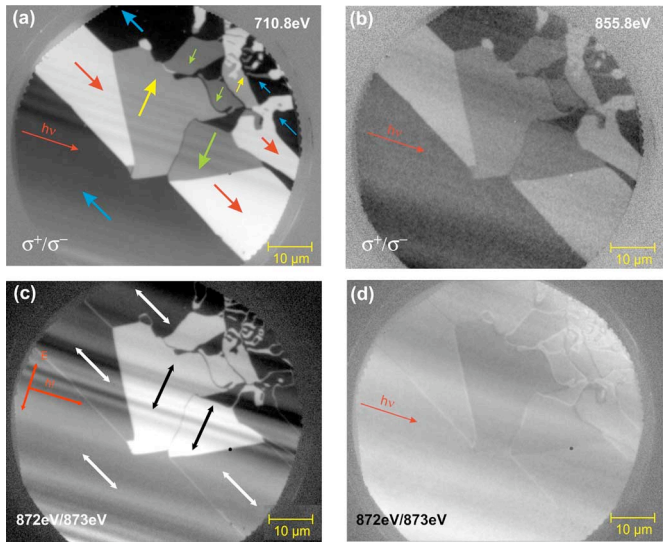

Fig. 26. Magnetic domain patterns in a 15 monolayer NiO film on top of a $Fe_3O_4(011)$ single crystal template. (a) Domain structure in $Fe_3O_4(011)$ obtained from XMCD at the Fe L_3 edge. (b) XMCD image at the Ni L_3 edge (comparing opposite light helicities σ^+ and σ^-), reflecting the induced ferromagnetic moments at the NiO side of the interface. (c) Antiferromagnetic domain pattern in NiO obtained with XMLD contrast and p-polarized light (electric field vector E indicated) at the Ni L_2 edge (comparing two photon energies corresponding to a multiplet splitting). (d) as (c), but acquired with s-polarized light. The similarity of the domain patterns in $Fe_3O_4(011)$ and NiO indicates a strong exchange coupling across the interface (From [267]).

materials class provides a large number of compounds with antiferromagnetic ordering and hence possible applications in spintronics. The strongly directional bonds and indirect exchange mechanisms in the oxides, however, give rise to an entirely different class of heteromagnetic interfaces with new and unexpected coupling behavior, which are only marginally explored up to date. A major obstacle on the way to a better understanding of these systems is in fact posed by the nature of an antiferromagnet, which—due to its vanishing net moment—is directly accessible only by a few techniques. As has been shown recently, XMLD is the method of choice for this purpose [8], [261].

Oxide thin films and thin film stacks are often grown at elevated temperatures. For this reason, fully oxidic interfaces are generally considered to be sharp and very stable, in contrast to metal-oxide interfaces, where redox reactions have to be taken into account. The system NiO/Fe_3O_4, which we will discuss in the following, combines a ferrimagnet (Magnetite) with an antiferromagnet (Nickel oxide). Previous studies have shown this combination to exhibit a sharp electronic transition [262], [263], implying a sharp structural interface, too. In the latter, a gradual disorder transition zone from oxide to metal may form [264], [265] if the interface cannot be passivated prior to deposition (see, e.g. [266]). In addition, this combination exhibits also a low lattice mismatch.

The magnetic contributions from ferri- and antiferromagnet can be conveniently separated by exploiting the XMCD and XMLD contrast mechanisms. Fig. 26 gives an example for a full set of data that can be acquired from such a system. The experiments have been carried out by means of photoemission microscopy, using a variable polarization undulator beamline (UE-56-SGM) at BESSY (Berlin) [267]. The XMCD contrast images taken at the Fe and Ni L_3 absorption edges, respectively, reflect the domain pattern in the Magnetite single crystal in the region close to the interface and a ferromagnetic contribution in the NiO film. It is known that the proximity of the ferrimagnet leads to a polarization in the antiferromagnet, which quickly decays away from the interface. In both images the contrast exhibits four distinct levels, which can be assigned to four in-plane magnetization directions marked by the arrows. These directions are consistent with the in-plane easy axes for the (011) surface of Magnetite.

The XMLD contrast from the NiO overlayer (15 monolayers thick) is more subtle. It is obtained by comparing difference images recorded at two slightly different photon energies (872 and 873 eV) corresponding to two multiplet-split states [268]. The resulting domain configuration is a replica of the XMCD pattern, however, with only two distinct contrast levels. The XMLD distinguishes only the alignment of the spins along a direction in space, but not the orientation, indicated by the bidirectional arrows in the figure. As a consequence opposite spin orientations will result in the same XMLD contrast level, even in a ferromagnet. At the domain walls, however, the spin alignment changes, giving rise to a line contrast between domains of the

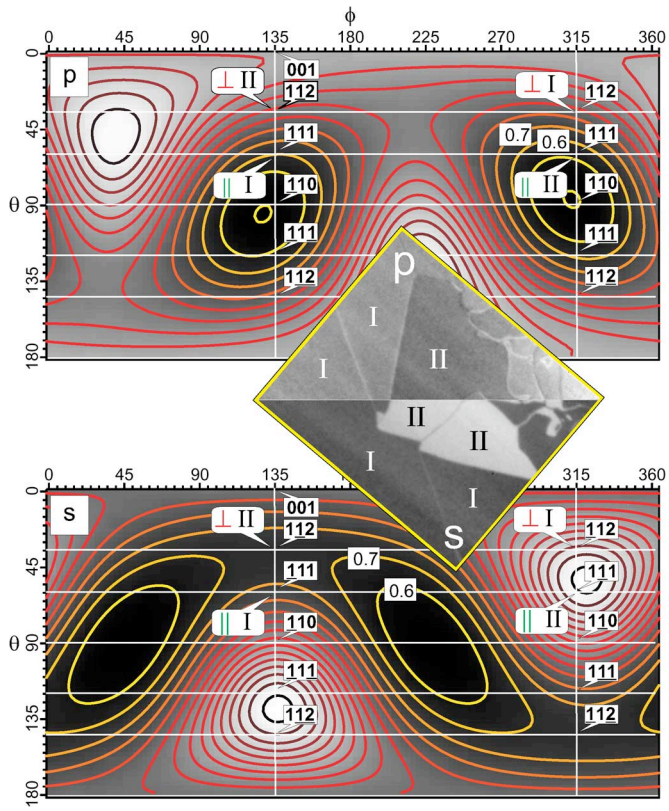

Fig. 27. Calculated XMLD contrast for all possible orientations of the spins in the NiO overlayer as given by the angles θ, ϕ for p- (top) and s-polarized (bottom) light. The inset gives the experimental XMLD domain patterns on a selected area of the sample surface, recorded with p- (top half picture) and s-polarized light (bottom half picture). The two types of domains (I and II) have orthogonal spin orientations. In addition, we have indicated the positions of high-symmetry crystalline axes. The contrast levels to be expected for collinear and spin-flop coupling are marked by $(\|)$ and $(\perp)$, respectively (from [267]).

same alignment. This line contrast is clearly visible in Fig. 26(c) and marks the position of the domain walls in the ferromagnet.

The ideal bulk-truncated (011) surface of NiO is spin-compensated, i.e., there is no residual magnetic moment in the lattice plane. For this situation theory predicts a 90°- or spin-flop coupling between the two magnetic constituents [269]. The situation depicted in Figs. 26(a) and (c), however, describes a *collinear* coupling between the ferro- and antiferromagnet, i.e., the spin orientation axis in the ferromagnet aligns parallel to the spin alignment directions in the antiferromagnet. The reason for this behavior may be sought in a deviation of the magnetic structure in NiO from the ideal bulk truncation. The data in Fig. 26(b) clearly show that the interfacial region in NiO has some residual ferromagnetic spin alignment caused by the proximity effect. In addition, the epitaxial strain imposed in the film by the nonzero lattice mismatch to the substrate may also lead to an alteration of the NiO spin structure in the interfacial region. In fact, the results of studies on the (001) and (111) oriented interfaces in the same material system suggest that magneto-elastic interactions in both the ferromagnet and antiferromagnet may not be negligible [270].

In order to arrive at the conclusion of collinear coupling in the case of $\mathrm{NiO/Fe_3O_4}(011)$ particular care must be taken in the interpretation of the XMLD contrast levels. From the images it can be seen that the contrast observed with p-polarized [Fig. 26(c)] and s-polarized light [Fig. 26(d)] is not only different in magnitude, but also changes sign. The reason for this strong variation of the XMLD contrast is the single-crystallinity of the sample, which requires the crystalline directions to be taken explicitly into account in the analysis. As a consequence, the XMLD signal depends on the relative orientation of light polarization, spin quantization axis in the antiferromagnet, and symmetry axes in the crystal. As has been pointed out recently, this situation asks for a detailed analysis of XMLD spectroscopic data recorded in different experimental geometries to unambiguously deduce the spin alignment in the antiferromagnet and a comparison to calculated spectra [271].

The result of such an analysis is depicted in Fig. 27, which compiles the calculated XMLD contrast levels for the experimental geometry (25° angle of incidence) and any arbitrary orientation of the spins in NiO (given by the two angles θ, ϕ) for p- and s-polarized light. In order to arrive at this contrast level map, in a first step two so-called fundamental spectra are calculated from ab-initio multiplet theories for the geometries $C_4^z \| \vec{S} \| \vec{E}$ and $C_4^z \| \vec{E} \perp \vec{S} \| C_4^x$, with the electric field vector $\vec{E}$, the spin axis $\vec{S}$, and two orthogonal cubic symmetry axes C_4^z and C_4^x, respectively. From these fundamental spectra the XMLD contrast map can be constructed using formalisms as described, for instance, in [271]. It is instructive to compare the two limiting cases of collinear $(\|)$ and spin-flop coupling $(\perp)$, which are marked in the graph, in a qualitative manner. If we take the contrast levels for the two orientations of the antiferromagnetic domains (I and II) for s-polarized light, for instance, spin-flop coupling $(\perp)$ should lead to type I (II) domains appearing bright (dark). The experiment obviously yields the opposite result, which provides a clear argument against spin-flop coupling. The results obtained for s- and p-polarization are much more consistent with the collinear coupling arrangement. This is confirmed by the quantitative analysis of the contrast levels for all domain orientations on this surface.

Finally, we are returning to the proximity effect discussed above. In Fig. 28, we show a compilation of XMCD microspectra from the $\mathrm{Fe_3O_4}(011)$ system. These have been extracted from image series taken as a function of photon energy across the $\mathrm{Fe}-L_{2,3}$ and $\mathrm{Ni}-L_{2,3}$ edges, exploiting the fact that opposite magnetization directions lead to an XMCD contrast inversion. The fine structure of the $\mathrm{Fe_3O_4}$ spectrum seen in Fig. 28(a) is well-known to be a consequence of an atomic multiplet splitting. The difference in signal height between domain sets I and II arises from the different projection of the magnetization vector onto the direction of light incidence. In the same way, the XMCD from the NiO-overlayer can be analyzed in order to locate the origin of the XMCD response. The spectrum at the Ni edges is characterized by single lines [Fig. 28(c)] and the signatures closely resemble the data of van der Laan for $\mathrm{NiFe_2O_4}$ [272]. Indeed, the formation of a $\mathrm{NiFe_2O_4}$ layer at the interface cannot be excluded, as the Ni ions have the same octahedral oxygen coordination and this phase can be obtained by a simple reconstruction of the sharp $\mathrm{NiO/Fe_3O_4}$ interface [273]. Comparing different thicknesses of NiO we find a strong signal at room temperature already

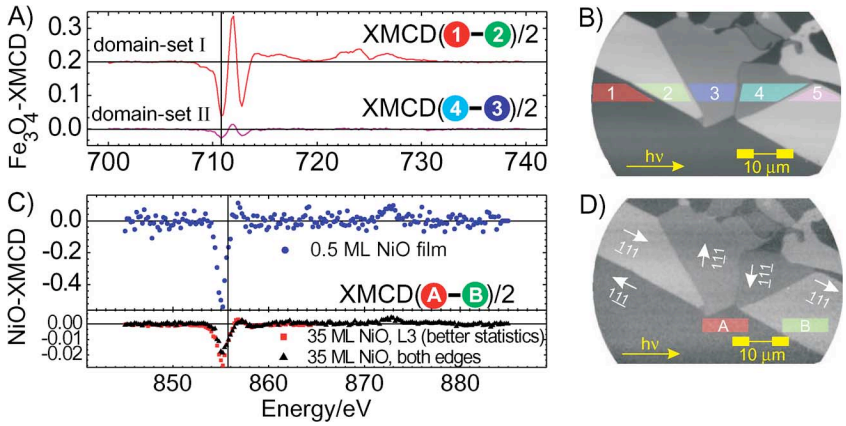

Fig. 28. XMCD microspectra from the $NiO/Fe_3O_4(011)$ system for the $Fe-L_{2,3}$ (a) and $Ni-L_{2,3}$ edge (c) derived from the regions of interest 1–4 and A, B as indicated in (b) and (d). In order to improve the signal/noise, spectra from opposite magnetization directions have been combined appropriately ([1–2], [3–4], $[A-B]$). In (c) also the XMCD spectra for two different NiO overlayer thicknesses of 0.5 ML and 35 ML are compared (From [267]).

at a coverage of 0.5 monolayers. Since the Néel temperature of such a thin NiO overlayer is far below 300 K [274], this ferromagnetic order must be entirely due to the proximity to magnetite. For the 35 ML film the situation is different, as the bulk of the film is antiferromagnetically ordered—confirmed by the XMLD results. Therefore, the XMCD signal stems from a residual ferromagnetic component at the interfaces (ferromagnetic defects in the bulk of the film can be ruled out as the overlayers are stoichiometric). Further analysis reveals the size of the Ni XMCD signal to be compatible with an interfacial ferromagnetic NiO layer of about 1.7 ML thickness.

These results suggest that the oxidic heteromagnetic system NiO/Fe_3O_4 forms a sharp interface with an ultrathin magnetic transition zone and can therefore be regarded as a model system for FM-AFM coupling phenomena. This example illustrates the wealth of information, that can be obtained from a heteromagnetic system using the various kinds of dichroic phenomena with circularly and linearly polarized light.

C. Nanomagnetic Structures

The photon-in/photon-out counterpart to photoemission microscopy may be seen in transmission X-ray microscopy. Its magnetically sensitive variant—magnetic transmission X-ray microscopy (MTXM)—uses mainly X-ray magnetic circular dichroism (XMCD) as a magnetic contrast mechanism. In the following, we will discuss the current status of this technique with a focus on magnetic imaging in the scanning mode.

High resolution MTXM, i.e., with a spatial resolution well below 100 nm, started in 1996 at the full-field transmission X-ray microscope (TXM) of the synchrotron source BESSY I in Berlin. With this setup magnetization reversal processes in thin out-of plane magnetized films [291]–[293] and magnetic nanostructures [294], [295] have been investigated. Later the technique was successfully implemented at a bending magnet beamline [296] of the Advanced Light Source (ALS) [297]–[313], including studies of in-plane magnetized samples [298], [302], imaging of bits in magneto-optical media with 25 nm lateral resolution [299], [301], and investigations of the magnetization dynamics in microstructures [309]. Beyond these studies which have been carried out in the full-field mode, also scanning transmission X-ray microscopes (STXM) have been employed for magnetic imaging. A first approach involved a linear undulator, the light of which was passed through a magnetic film acting as a Faraday circular polarizing filter [314]. Carrying out STXM at an elliptical undulator beamline [315], however, unfolds many new opportunities in MTXM [316]–[322], especially with respect to magnetization dynamics [316]–[320], highly sensitive detection schemes [317], [321], and XMCD spectromicroscopy [321], [322].

The sensitivity of MTXM scales with the XMCD contrast, which depends on the degree of circular polarization P, and the spectral resolution. Helical undulators provide intense, highly coherent X-rays with P ranging between 0.9 and 1 and are thus ideal sources for magnetic STXM. In TXM, however, the coherent undulator radiation causes disturbing interference fringes, which can only be avoided by sophisticated designs [323]. On the other hand, bending magnet radiation has a much lower degree of spatial coherence and is thus more favorable for TXM applications. As a limitation, the lower photon flux prevents the use of a crystal monochromator, having a ten times higher spectral resolution $E/\Delta E$ than the alternatively used zone-plate monochromator, see Table I. In addition, the necessary compromise between intensity and degree of circular polarization limits P to values between 0.6 and 0.8. Nevertheless, this is sufficient to resolve magnetic domains in films with an effective thickness of 2 nm and below in TXM. Even higher sensitivity can be reached in STXM, where $E/\Delta E$, P and the photon flux are superior. This and the ability to normalize images taken with left and right circularly polarized light without artifacts due to changes in the spatial distribution of the illumination allows a detection of very small magnetic signals. An impressive demonstration has been given recently by a study of proton irradiated carbon, where a magnetic moment of less than 10^{-3} Bohr magneton per atom was sufficient to provide magnetic contrast in STXM [321].

The spatial resolution in transmission X-ray microscopy is largely determined by the outermost width of the used micro-zone plate (MZP). State-of-the-art nano-lithography has been able to construct zone plates with a lateral resolution of better

TABLE I
COMPARISON BETWEEN TXM AND STXM AS OPERATED AT THE ALS. THE PARAMETERS OF THE XM-1 BENDING MAGNET BEAMLINE 6.1.2 AND THE STXM AT THE ELLIPTICAL UNDULATOR BEAMLINE 11.0.2 ARE LISTED. THE ABBREVIATIONS: OP, IP AND ∅ STAND FOR OUT-OF-PLANE, IN-PLANE AND DIAMETER, RESPECTIVELY

	TXM (XM-1)	STXM (BL 11.0.2)
spectral resolution	250 - 700	2500 - 7500
spectromicroscopy	hardly possible	well suited
degree of circular polarization	0.6 - 0.8	0.9 – 1
field of view	Ø∼10 −15μm	upto 4 mm^2
radiation dose	high	low
illumination	inhomogeneous	homogeneous
exposure time [$10\times10\mu$m^2]	1 - 10 s	700 s
exposure time [$10\times10\mu$m^2]	1 - 10 s	10 s
detector readout	1 s	< 50 ps
change time from op to ip	10 min	60 min
perpendicular magnetic field	±5 kOe	±0.7 kOe
horizontal magnetic field	±1 kOe	±1.3 kOe

than 15 nm [324]. Generally, it is easier to obtain nanometer spatial resolution in TXM where the sample is fixed, than in STXM where it has to be scanned. However, interferometric control of the MZP and the sample stages [315] enables about equally high lateral resolution in scanning and in full-field mode.

For time-resolved studies there is an important difference between the full-field and the scanning mode: TXM uses a two-dimensional detector, i.e., a CCD camera that has a readout time of about one second. In contrast, in STXM experiments a fast point detector can be used. Avalanche photodiodes are fast enough to detect single X-ray photons. Combined with high-speed electronics this allows pump-probe experiments in the normal (multi-bunch filling) mode of the ring even for samples having longer relaxation times than the repetition rate of the synchrotron pulses [325]. A large gain in available beamtime results from this approach, since at the ALS the two-bunch filling mode, which is necessary for pump-probe experiments in TXM [309], is only provided two times a year. This and other advantages of STXM, like the high sensitivity, recently boosted a number of studies on the dynamics of vortex cores in patterned magnetic systems [316], [318]–[320] and on current-induced switching of magnetic nanostructures [317].

Since the XMCD contrast is proportional to the projection of the magnetization on the X-ray propagation direction, out-of-plane magnetization components are probed, if the sample plane is perpendicular to the beam. By tilting the sample with respect to the optical axis also in-plane components can be detected. At the XM-1 beamline such a tilting is as easy as changing a sample and takes only a few minutes. In the STXM of beamline 11.0.2 the whole scanning stage has to be tilted and aligned again, which takes about one hour. An important feature of MTXM is the ability to study magnetization reversal processes by imaging in applied magnetic fields. This is possible, since MTXM is a photon-in/photon-out based technique, where applied magnetic fields do not disturb the magnetic imaging, in contrast to other high resolution techniques that detect electrons, like Lorentz microscopy, photoemission electron microscopy (PEEM), or scanning electron microscopy with polarization analysis (SEMPA). The size of applicable magnetic fields in MTXM is only limited by the available space around the sample stage. Currently, at the XM-1 magnetic fields with strengths of up to ±5 kOe and ±1 kOe can be applied perpendicular and in the sample plane, respectively. Since recently, magnetic fields of comparable strength (see Table I) can also be applied at the STXM of beamline 11.0.2. This enables measuring of element selective, local magnetization loops, as will be demonstrated in the following.

A multilayered $[\mathrm{Gd}(0.36\,\mathrm{nm})/\mathrm{Fe}(0.36\,\mathrm{nm})]\times50/\mathrm{Al}(8\,\mathrm{nm})$ system has been deposited on top of self-assembled silica spheres with a diameter of 330 nm. Fig. 29(a) shows an STXM image of the particles. A close-packed, hexagonal arrangement is visible in the area marked by a square. This region has been recorded both at the Fe L_3 absorption edge (707 eV) and at the Gd M_5 absorption edge (1190 eV). Images taken with left and right circularly polarized X-rays have been normalized in the XMCD images of Figs. 29(b) and (c), presenting the Fe and Gd magnetization, respectively. The reversal of the contrast is a sign for an antiparallel coupling between Fe and Gd magnetic moments. To study the details of this coupling scans along the line marked in 29(a) in were performed different external magnetic fields. This was done both at the Fe L_3 and at the Gd M_5 absorption edges and for both helicities of the X-rays. The resulting series of line-field scans is presented in 30(a), (b), (d), and (e). The recording time for each scan is less than two minutes. Figs. 30(c) and (f) show the respective XMCD contrast [325] at the Fe and Gd edges, respectively. In order to extract local magnetization loops of the nanocaps and the flat substrate, the signals in the areas marked by rectangles are averaged and plotted in Fig. 31. These loops reveal that the film on the flat substrate shows a Gd aligned state with an antiparallel coupling between Fe and Gd magnetic moments [322]. In contrast, the nanocaps possess an Fe aligned state for fields below 11 mT and above a canted state, where Fe and Gd moments are under an angle with respect to the field.

To summarize, in the first decade after its invention MTXM developed into a powerful tool for studying magnetization reversal processes and magnetization dynamics in thin films or nanometer sized magnetic systems in an element selective and quantitative way. In the soft X-ray regime the MTXM technique is currently performed at the TXM (beamline 6.1.2) and the STXM (beamline 11.0.2) of the ALS. Recently, first MTXM images have also been reported from the Swiss Light Source using the STXM at the PolLux bending magnet beamline [327]. The future of MTXM is bright, as a new STXM, dedicated for

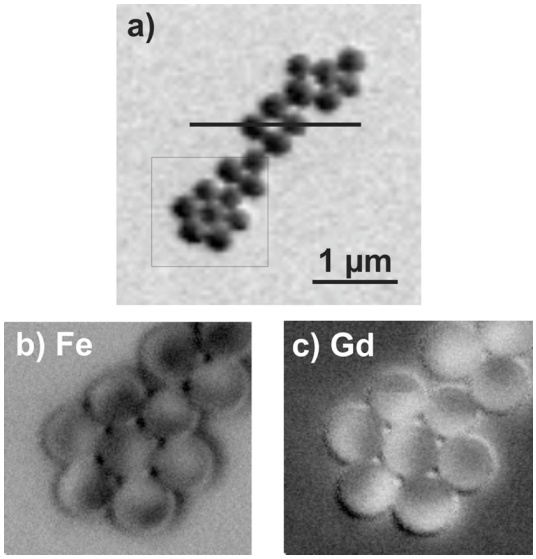

Fig. 29. Silica spheres with a diameter of 330 nm are covered with a Fe/Gd multilayer. a) Overview image. XMCD images of the marked region show magnetic domains of the nanocaps taken at b) the Fe L_3 absorption edge and c) at the Gd M_5 edge.

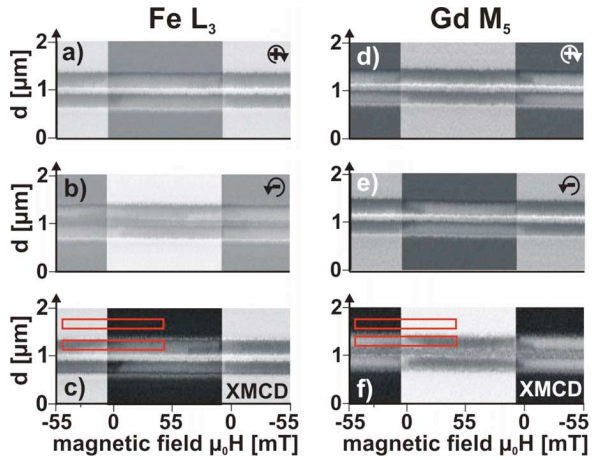

Fig. 30. A 2 μm long scan (ordinate) along the line marked in Fig. 29(a) is repeated at different magnetic fields $\mu_0 H$ (abscissa), ranging from -55 mT to 55 mT and back again to -55 mT. The figures at the left (right) column have been taken at the Fe L_3 (Gd M_5) absorption edge. Right circularly polarized X-rays were used for (a) and (d), left circularly polarized light for (b) and (e). The Fe and Gd XMCD contrasts are presented in (c) and (f), respectively.

magnetic imaging is currently being build at a helical undulator beamline of the German synchrotron BESSY II in Berlin and another one is planned at the French Synchrotron SOLEIL.

D. Lensless Imaging

In the application examples of synchrotron radiation so far, the brightness and the variability of the light polarization have played a major role. One has to keep in mind, however, that the radiation generated in third generation sources is already partially coherent. As is well-known from classical optics, coherent light enables a use of the phase information in an imaging process, for example, in holography. Exploiting the coherence

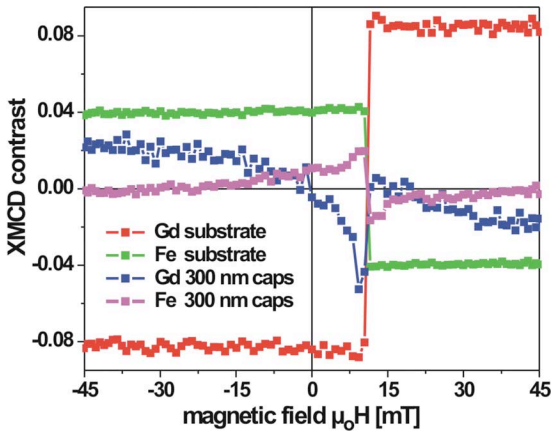

Fig. 31. Element selective magnetization loops. For clarity only one branch, measured from negative to positive magnetic field direction, is shown. The curves reveal different spin configurations of the Fe and Gd moments. A tilted state is observed at the nanocaps for magnetic fields above 11 mT [322].

of soft X-rays therefore opens up a pathway for novel experiments.

It was indeed shown recently that holography with soft X-rays is feasible and provides high resolution images of the local sample magnetization [275], similar to X-ray microscopies [276]. In this approach a coherent X-ray beam from a synchrotron radiation source is used to record a Fourier Transform Hologram (FTH), which leads to an image by means of direct Fourier inversion. This is achieved by lithographically defining a proximity X-ray mask structure directly on the sample to be studied, thus defining an object area (= field of view, FOV) and a suitable reference beam. A practical way to produce such a structure is by focused ion beam milling [275]. In practice, many object areas with respective references can be integrated in one sample and imaged during the same exposure, allowing a multiplexed data acquisition of entire sample arrays [279], [280]. So far, all soft X-ray FTH experiments are carried out in transmission geometry, with samples supported by thin membranes. Magnetic contrast is obtained by X-ray magnetic circular dichroism (XMCD) or X-ray magnetic linear dichroism (XMLD) by choosing a suitable X-ray polarization and resonant scattering conditions at an absorption edge of interest [281], e.g. by tuning the photon energy to the Co L_3 resonance in the examples presented in Fig. 32. As in all scattering-based imaging techniques, the spatial resolution is limited by the wavelength and the maximum recordable scattering angle (numerical aperture). With many suitable resonances (e.g. 2p levels of 3d transition metals) providing strong magnetic contrast in the 1 nm–2 nm wavelength regime, the spatial resolution today is in practice limited by (i) the coherent X-ray photon flux and (ii) the lateral size of the reference scatterer (which is directly proportional to the obtainable spatial resolution unless its shape/transmission is known). The holographic imaging approach using magnetic contrast via resonant X-ray scattering has the following characteristics, which make the spectro-holography well suited for domain imaging and magnetic switching studies on the sub 100 nm length scale.

i) Best lateral spatial resolution today: 30 nm–50 nm, [275], [287]. limited by the reference size and the scattering signal (which is in turn typically limited by the coherent X-ray flux).
ii) Element specificity coupled with penetration depths on the order of 1 μm, allowing to study buried structures. The image is a projection through the sample [277].
iii) High imaging sensitivity due to vibration insensitivity thus allowing long exposure/integration times (e.g. the magnetic moment of 2 nm thick Co layers in a 250 nm thick structure can be resolved).
iv) Ability to apply magnetic and electric fields during the measurement.
v) Local magnetization and topography can be separated in the images using the polarization/geometry dependence of XMCD or XMLD.
vi) Flexible sample environment due to lack of technique dictated space constraints around the sample; in particular sufficient space to place/rotate bulky magnets around the sample or to realize variable temperature conditions.
vii) Sample and reference multiplexing is possible allowing to study entire sample series under identical conditions [279], [280].
viii) The FOV has to be lithographically predefined, enabling correlative microscopy with other techniques but preventing to change the FOV during the measurement.
ix) The sample has to have sufficient soft X-ray transmission, i.e it has typically to be thinner than 1 μm and free standing or on a (e.g. Si_3N_4) membrane.
x) Both amplitude and phase contrast is accessible simultaneously [282].
xi) The transmission geometry is particularly well suited to study magnetic materials with perpendicular anisotropy using circularly polarized X-rays.

Examples for magnetic domain images recorded by FTH at BESSY are presented in Fig. 32. In panel (a), three images out of a switching sequence of a $[\mathrm{Co}\ 12\ \text{Å}/\mathrm{Pt}\ 8\ \text{Å}]_{50}$ multilayer are presented [283]. A series of images along a hysteresis loop allows to follow the domain evolution during magnetization reversal. The switching behavior of magnetic multilayers on a monolayer of polystyrol nanospheres of approximately 110 nm diameter was studied in the images selected for panel (b) [284], [285]. The magnetic multilayer composition is $[\mathrm{Co}\ 3.5\ \text{Å}/\mathrm{Pd}\ 8\ \text{Å}]_8$, i.e., the depth integrated Co thickness amounts to 2.8 nm. Due to the existence of the mask, the holographic images of the switching behavior can be unambiguously correlated with SEM images of the sample topography. As a result, the structure-function relationship (e.g. influence of shape, size, or relative orientation of the nanostructures on their switching behavior) can be investigated in great detail [286]. The images in panel (c) are part of a switching study on prototype structures for lithographically patterned magnetic data storage media, consisting of 50 nm $\times$ 50 nm square magnetic multilayer structures $[\mathrm{Co}\ 4.5\ \text{Å}/\mathrm{Pd}\ 9\ \text{Å}]_{10}$ on a 100 nm pitch. The spatial resolution in the magnetic images obtained by spectro-holography is 30 nm [287].

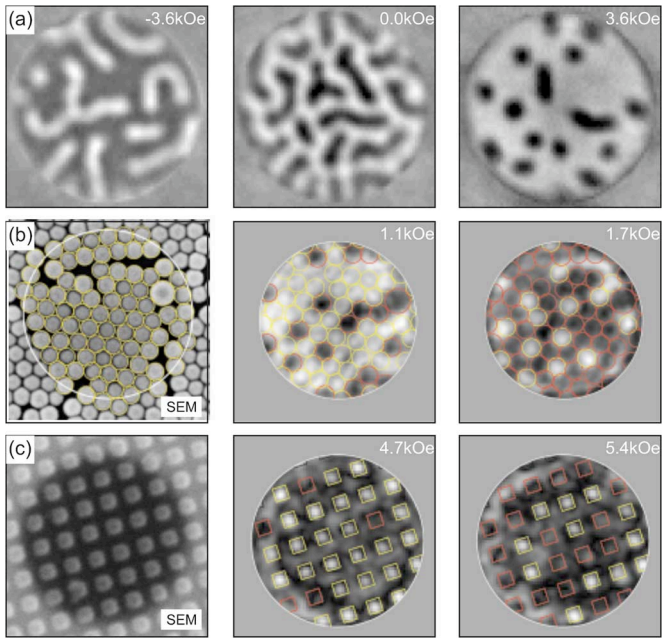

Fig. 32. Greyscale magnetization maps obtained by spectro-holographic imaging. (a) Part of a switching sequence of a $[\mathrm{Co}\ 12\ \text{Å}/\mathrm{Pt}\ 8\ \text{Å}] \times 50$ multilayer with perpendicular anisotropy, recorded in applied external fields (from [283]). The circular FOV is 1.5 μm. (b) Magnetic multilayers on polystyrene nanospheres ($\mathrm{diameter} \approx 110\,\mathrm{nm}$) are seen in SEM (left) and their magnetic switching behavior is imaged holographically. The circular FOV is 910 nm (from [286]). (c) Prototype patterned storage medium consisting of 50 nm squares on a 100 nm pitch. Left: SEM, middle and right: spectro-holographically obtained switching patterns in remanence after the indicated field had been applied (FOV diameter 910 nm) (from [287]). The overlays in panels (b) and (c) are derived from the SEM images and allow a clear correlation between the nanostructure topography as seen in SEM and the magnetization map as seen in holography. The greyscale within the FOV of the holographic images corresponds to the projection of the magnetization onto the sample normal.

While in the examples Fig. 32 "slow" dynamics driven by external fields has been investigated (as is relevant for storage applications), one should point out that the need to integrate the sample with a micro- and nanostructured mask is compatible with the definition of micro-strip lines, micro-coils etc. as part of this mask. As a result, magnetic pump-probe experiments can be realized to access picosecond dynamics of repetitive magnetic relaxation processes with the probing characteristics listed above, which may be an interesting complement to PEEM studies (see below) as they would allow one to study buried structures.

As an interference-based technique dependent on coherent photon flux, X-ray holography will benefit tremendously from the free electron laser based X-ray sources under construction worldwide today. Because the available coherent photon flux will be increased many orders of magnitude over what is available at storage ring based synchrotron sources today, significantly improved spatial resolution and sensitivity can be expected. Furthermore, the sub-100 fs pulsed nature of these sources will make holographic snapshot imaging possible, as a single pulse has sufficient coherent photons to generate an image [278]. In this way, femtosecond dynamics will become accessible, provided that the problems of sample damage due to the intense FEL radiation can be overcome or circumvented,

so as to allow for a repeated imaging of the same sample.[1] The prospect of being able to take "femtosecond still pictures" with possibly sub-10 nm resolution is particularly intriguing in order to image the spontaneous magnetization in the absence of external fields. In this way, it may e.g. become possible to directly observe locally correlated areas of fluctuating spins, such as "the dance" of spin blocks at magnetic phase transitions [288]–[290].

VII. Time-Resolved Studies of Magnetism

The dynamic behavior of a magnetic system covers an extremely broad range of more than 20 orders of magnitude. A technically defined value for the data retention time in a magnetic storage system is 10 years. On the other end of the time scale we have microscopic processes dominated by the exchange interaction on a time scale of femtoseconds. In between lies a wealth of different dynamical phenomena ranging from magnetic creep, through domain nucleation and domain wall motion to spin waves and precessional movements of the magnetization.

The fundamental mechanisms governing the magnetization dynamics on the nano- and picosecond timescales are still only partially understood. An intense research activity in this field is directed towards the ultimate speed limits of magnetization reversal and alternative switching strategies, for example, by employing spin-polarized currents or intense photon fields. The knowledge on fast magnetic switching is also of enormous technological importance for applications in magnetic data storage and spin electronics.

The intrinsic time structure of the synchrotron radiation, providing picosecond light pulses with several hundred MHz repetition rate, recently enabled a unique element-selective approach to magnetodynamics, which has been particularly exploited in time-resolved magnetic imaging experiments. For reasons of convenience, in the following we will distinguish between *magnetodynamics* and *spin dynamics*. Magnetodynamics relates to the dynamic response of the magnetization in a continuum-type picture and is very successfully described within the Landau-Lifshitz-Gilbert framework. In this context also spin waves fall into the regime of magnetodynamics. Spin dynamics, on the other hand, rather denotes the excitation and response of individual spins on an electronic time scale, i.e., in the femtosecond regime.

A. Magnetization Dynamics in Small Elements

The investigation of magnetodynamic processes in thin films has been pioneered by stroboscopic Kerr microscopy [3]. Based on these experiences, recently a time-resolved version of soft X-ray photoemission microscopy has been developed [328], providing an element-selective approach to magnetization dynamics. In the simplest case, time-resolved PEEM involves an accumulated imaging of the magnetic structure, while the system is "pumped" by magnetic field pulses synchronized with the soft X-ray pulses from the synchrotron ("probe"). The time resolution in this mode is mainly determined by the width of the synchrotron light pulse (of the order of 50 ps) and the temporal development of the magnetodynamic process is followed by changing the time delay between the magnetic pump and the photon probe pulse (Fig. 33). More elaborate configurations use image detectors with intrinsic time-resolution [329]. In order to obtain a steep rise time of the magnetic field pulse, the samples are placed onto coplanar waveguides or in the center of a micro-coil. The current through the waveguide can be conveniently controlled by electrical pulse generators or by means of photoconductive switches (fast photodiodes or "Auston switches") triggered by laser pulses. In this way, a rise time down to a few 10 picoseconds can be achieved [330]. A variable delay between magnetic pump and optical probe is realized either by an electrical delay generator or an optical delay stage.

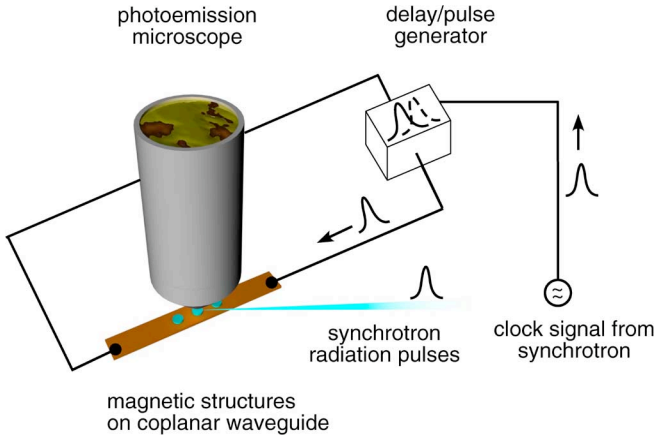

Fig. 33. Schematics of a time-resolved PEEM (TR-PEEM) experiment. The synchronizing clock signal is derived from the high frequency power circuit used to reaccelerate the electrons in the storage ring. A delay generator provides a variable delay between pump (magnetic field) and probe (light) pulses.

Combining the high lateral resolution provided by PEEM with the short timescale defined by the synchrotron radiation pulses give a unique access to magnetodynamics and the experiments carried out so far have revealed a wealth of micromagnetic processes in the nano- and picosecond regime, ranging from nontrivial vortex dynamics to entropy-driven domain wall motion [331]–[337]. In the following, we will discuss only a few selected examples.

The velocity of magnetic domain walls is an important issue, as the nucleation of domains and the motion of domain walls are at the core of most magnetization reversal processes. The speed with which domain walls are moving depends strongly on material, geometry, and the actual reversal process, and may be a limiting factor in novel logic or storage devices based on domain walls [338], [339]. In Fig. 34, we display the example for a Permalloy microstructure, which has been excited with bipolar pulses of about 2 mT total amplitude and 300 ps FWHM at a repetition frequency of 500 MHz. In response to this excitation, the domain wall oscillates around an dynamic equilibrium position. It may be noted that this equilibrium position is considerably displaced from the center of the structure. The latter effect is caused by an entropy-driven mechanism involving the fundamental precessional mode of the domain magnetization and leading to a "self-trapping" of the domain wall [335]. Following

[1]The authors in [278] estimated the FEL pulse of 25 fs duration employed to take the hologram to heat up the sample to a temperature of about 60,000 K. This caused the sample to immediately vaporize after the data had been taken.

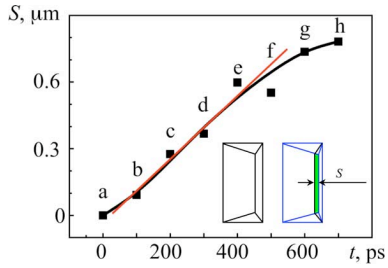

Fig. 34. Domain wall motion in a rectangular Permalloy microstructure ($10\ \mu\mathrm{m} \times 5\ \mu\mathrm{m}$, 10 nm thick). Letters a to h refer to a sequence of individual PEEM images with increasing time delay, from which the displacement $s(t)$ of the wall has been determined (see sketch). From [328].

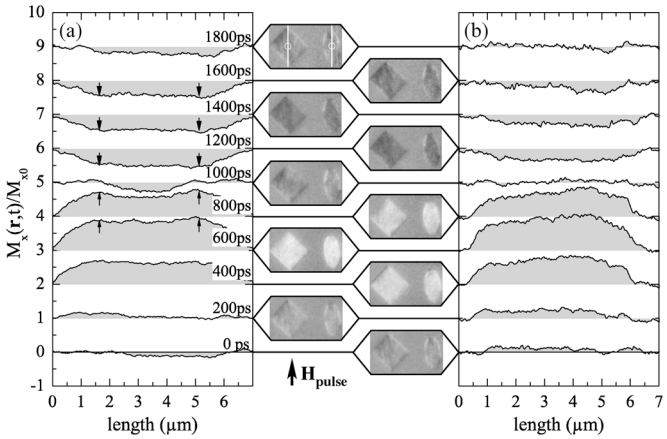

Fig. 35. Time-resolved photoemission microscopy from the magnetodynamics in a spin-valve system. The center part reproduces the temporal development of the soft layer magnetization dynamics in steps of 200 ps responding to field pulses at 500 MHz repetition frequency. Side panels compile line scans of the magnetic contrast level across the diamond (a) and the ellipse (b) along the lines marked in the top image. After [345].

the displacement $s(t)$ of the wall from this equilibrium position as a function of time, we find a characteristic behavior, which to a good approximation can be described by a linear dependence. From this linear dependence we can extract a value for the domain wall velocity $v_{\mathrm{DW}} \sim 10^3\ \mathrm{m/s}$. This is more than an order of magnitude higher than values calculated for a quasi-static reversal process involving a solitary 180° Néel wall [340] in a Permalloy film of similar thickness, but only a factor of 2–3 higher than in other experimental reports [341] and still below the Walker limit [342]. In future experiments, the time-resolved PEEM technique may also be used to determine the wall velocity in other nanomagnetic structures, such as small magnetic rings or nanowires.

Another issue of general importance in magnetodynamics is the non-uniformity of the dynamic response. It is well-known that in some cases this response follows a coherent precessional motion of the magnetization, i.e., it can be described by a simple macrospin model on the basis of the Landau-Lifshitz-Gilbert (LLG) equation [343]. In particular, if microstructured elements are considered, however, we have to take into account the formation of characteristic spin wave modes, the structure and eigen frequencies of which depend on the size and shape of the element [344]. Their quantitative description requires a full micromagnetic simulation of the magnetic system under investigation. For a given sample the general question will thus be how large the role of these modes is or in other words how strongly the system deviates from the macrospin model.

In Fig. 35, we compile the results obtained on the magnetodynamics of the top Permalloy layer of a complex spin valve system [345]. The sample consisting of microstructured elements ($5\times5\ \mu\mathrm{m}^2$ and $6\times3\ \mu\mathrm{m}^2$) has been excited with unipolar field pulses of ~250 ps width at a repetition frequency of 500 MHz. The static ground state of the structure corresponded to a "S" state.

The dynamic response reveals two distinctly different contributions. The first contribution shows up as a homogeneous change of the dichroic contrast in the images (center rows in Fig. 35) as a function of time delay Δt. The change from grey to white up to $\Delta t = 600$ ps is due to an almost coherent rotation of the magnetization into the direction of the applied field. Note that this maximum of the precessional motion is reached long after the pulse field H_{pulse} has been switched off. This transient state is followed by a damped oscillatory relaxation of the system, which is responsible for the black contrast at around $\Delta t = 1300$ ps, indicating the average magnetization to point oppositely to the direction of the driving field H_{pulse}. This behavior is consistent with the expectation from the macrospin model.

In order to separate the second contribution resulting from nonuniform motions of the magnetization, it is necessary to take line scans across the structures along the white lines indicated in Fig. 35. These line scans reveal that the diamond-shaped and elliptical particles behave quite differently. The magnetic contrast in the elliptical particle is almost the same over the center part of the element and decreases sharply at the edges. In the ideal case of a uniform precessional mode the contrast level in the center region of the element should be a plateau, i.e., constant. The small deviations from a constant value leading to a broad maximum in the center of the ellipse may indicate the presence of weak nonuniform precessional modes. These nonuniform excitations show up much more pronounced in the diamond-shaped particle, however, where they lead to clear maxima and minima [indicated by the arrows in Fig. 35(a)] in the line scans. Further analysis shows that these extrema correspond to well-defined standing spin wave modes with two nodes along the direction of H_{pulse}. In the elliptical element this mode is apparently suppressed. This behavior could be also qualitatively reproduced in micromagnetic simulations [345].

This example highlights the complex interplay of uniform and nonuniform motions of the magnetization in small magnetic elements, the understanding of which requires a magnetic imaging technique with both high lateral and high time resolution. The element selectivity will be mandatory, if the influence of magnetic coupling mechanisms on the magnetodynamics in layer stacks is to be addressed.

B. Vortex Dynamics

Both X-ray photoemission and transmission microscopy have been involved in dynamics studies of very fundamental micromagnetic structures in thin film systems. One of these fundamental structures is a so-called vortex. It forms, for example,

in circular micro-and nanostructured magnetic elements of certain thickness and size. The investigations have shown a vortex to have a unique dynamic behavior, which involves processes on a time scale ranging from a several nanoseconds down to a few picoseconds. The vortex core plays a pivotal role in the dynamic response of the entire magnetic system. The core is a peculiar structure on a length scale of the order of 10 nm, in which the magnetization turns perpendicular to the film plane [346], [347]. The direction of the core magnetization—it's polarization—can point up or down and is independent of the rotation sense of the vortex magnetization. This very small perpendicularly magnetized region affects the dynamics of the entire magnetic vortex on a much larger length scale. This becomes already apparent when analyzing the fundamental excitation mode of a magnetic vortex. This is a gyrotropic motion where the position of the vortex core rotates with relatively large amplitude (up to a few 100 nm), but low frequency (several 100 MHz) around the equilibrium position in the center of the element. The sense of the rotation is unanimously determined by the orientation of the core magnetization pointing up or down. This gyrotropic motion has been first theoretically predicted [348] and later confirmed in time-resolved X-PEEM experiments [332]. In addition to this gyrotropic rotation, however, also symmetric precessional modes in the GHz frequency regime have been observed [349] in circular vortex structures. In this latter case, the system has been excited by short magnetic field pulses perpendicular to the film plane. Detailed experiments with time-resolved X-ray transmission microscopy [318] showed for the first time that the core polarization can be switched between the up and down configuration by means of a small oscillatory external field, provided that the resonant excitation of the vortex is sufficiently strong. This observation has been interpreted in terms of a complicated sequence of vortex-antivortex creation and annihilation steps [350]. Extensive micromagnetic simulations have confirmed this microscopic origin of the core switching process [351], [352]. They have also evaluated the time evolution of the vortex core reversal. As a result, the reversal is found to be driven mainly by the exchange interaction and is therefore predicted to take place on a time scale of only a few 10 ps. Further simulations also predict that the same microscopic processes are also involved if the core reversal is initiated by short pulses of a spin-polarized current [353]. The extraordinary speed of the reversal stimulates considerations to use this ultrafast process in vortex core memories (VRAM) [354].

C. Ultrafast Spindynamics

The rapidly increasing information density required of modern magnetic data storage devices raises the question of the fundamental limits in bit size and writing speed. Presently the magnetization reversal of a bit can occur as quickly as 200 ps which is governed by the reversal mechanism and the applied magnetic field pulse shape [355]. A fundamental limit has been explored by using intense magnetic field pulses of 2 ps duration leading to a nondeterministic magnetization reversal [356]. For this process dissipation of spin angular momentum to other degrees of freedom on an ultrafast timescale is crucial [356]. An even faster regime can be reached by heating a magnetic bit with an intense femtosecond (fs) laser pulse. If these processes are understood and controlled this might pave the way for an increase in the writing speed of magnetic data storage systems by a factor of up to 10^3.

When energy is pumped into electronic excitations of a metal via absorbing a fs optical laser pulse it takes time to reestablish thermal equilibrium. This timescale is ultimately determined by energy transfer from the electronic system to the lattice. If for ferromagnetic metals laser excitation should also lead to an ultrafast quenching of the ferromagnetic order [359], [360], angular momentum conservation dictates that an exchange of spin angular momentum with a reservoir such as the lattice has to occur [358], [360]–[363]. However, there is considerable disagreement about the timescale for such spin-lattice relaxation. It was established early that spin-lattice relaxation should proceed on timescales $\sim$100 ps [360], [362]. Such values are also obtained from the damping of magnetization precession [355], [356], [358]. There is growing evidence, although no direct observation, that on the fs timescale the magnetic moment is affected by laser heating [359], [363]–[365]. Even on the fs timescale total energy and angular momentum are conserved. It is debated whether the reduction of the magnetic moment, which corresponds mainly to spin angular momentum, occurs via spin-orbit coupling during coherent laser excitation [357] with an angular momentum transfer from the spins to the electron orbits or via a fs spin-lattice relaxation mechanism [358].

The first experiments in this field [366] aimed at addressing these issues by using circularly polarized soft X-ray pulses of 100 fs duration to determine the temporal evolution of spin and orbital angular momentum in ferromagnetic Ni after optical fs laser excitation. As will be shown in more detail in the following, using X-ray magnetic circular dichroism (XMCD) one observes that the spin angular momentum is quenched on a timescale of 120 ± 70 fs and that electron orbits do not act as a reservoir for angular momentum. These results demonstrate the existence of a novel fs spin-lattice relaxation channel.

The laser-pump—X-ray probe experimental setup is sketched in Fig. 36 [366]. A fs laser (wavelength 780 nm, repetition rate 1 kHz, pulse energy 2.5 mJ) modulates the stored electron bunches in the modulator which subsequently generate fs X-ray pulses in the radiator. The sample is excited by part of each laser pulse (15%) via a variable delay. Transmitted X-rays are detected by an avalanche photodiode behind the sample. The angle between laser and X-ray beams is 1°. During time-resolved measurements a mechanical chopper in the pump beam is used to alternate measuring the X-ray absorption of the laser-excited sample and the sample in thermal equilibrium with a repetition rate of 500 Hz. Inherent pump-probe synchronization is achieved since the same femtosecond laser is used to generate fs X-ray pulses and to excite the sample. Contrary to previous femtoslicing sources [369] a helical undulator enables complete polarization control of X-ray pulses [367], [368]. These are used to stroboscopically probe the electronic and magnetic state by means of XAS and XMCD [50], [370], [371], respectively. The X-ray spot size on the sample (0.5×0.1 mm^2) is smaller that the pump laser spot size (1.5×0.5 mm^2). The sample consists of a 30 nm Ni film evaporated in-situ under ultrahigh vacuum conditions onto a 500 nm thick Al foil of 5×5 mm^2 lateral size. This results in

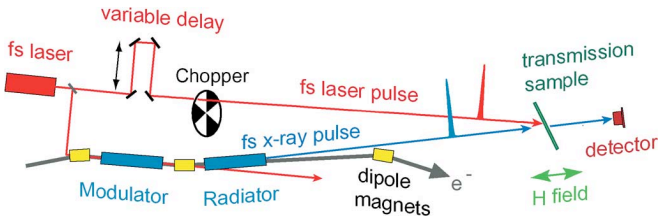

Fig. 36. Sketch of the pump-probe setup as described in the text.

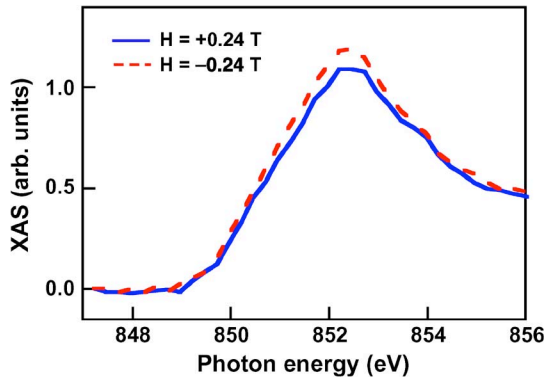

Fig. 37. XAS spectra obtained with circularly polarized femtosecond X-rays at 60° incidence relative to the sample surface. A static magnetic field of ±0.24 Tesla was applied along the X-ray incidence direction, resulting in the dashed red and solid blue curves, respectively. The difference between these curves corresponds to the magnetic circular dichroism.

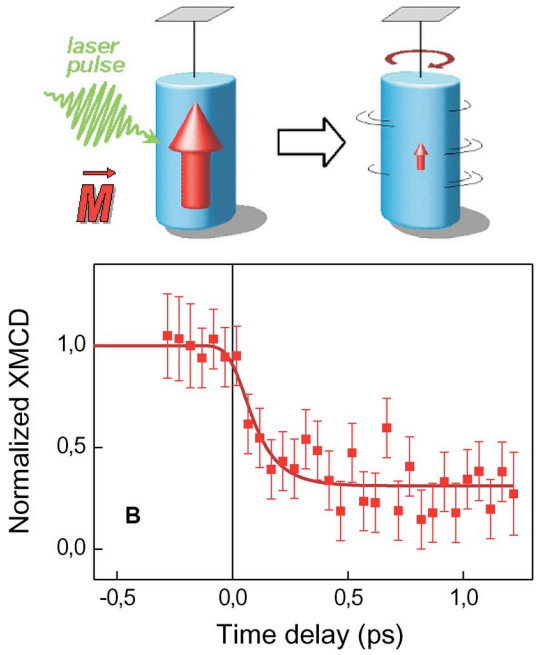

Fig. 38. (Top) Schematic illustration of the laser induced ultrafast spin-lattice relaxation mechanism in analogy to the static Einstein-de-Haas experiment [361]. (Bottom) Time-resolved XMCD signal with circularly polarized X-rays incident at 60° relative to the sample surface versus pump-probe time delay (symbols) measured at the $\mathrm{L_3}$ edge maximum. The photon energy resolution was 3 eV. Lines are fits of the three-temperature mode [359] to the data. The pump laser fluence was 8 $\mathrm{mJ/cm^2}$. The XMCD data shown in this figure are normalized to the corresponding data taken without laser pump pulses. Taken from [366].

an uncontaminated, homogeneous, polycrystalline film which can be magnetically saturated in the film plane by applying a magnetic field of $\mathrm{H} = \pm 0.02$ T as checked with static XMCD measurements.

Fig. 37 shows X-ray spectra of the $\mathrm{L_3}$ absorption recorded with circularly polarized fs X-rays for opposite magnetization directions in thermal equilibrium (at negative time delays). The XMCD (not shown) is the difference between the two spectra. Fig. 38 displays time resolved measurements of the XMCD signal with the photon energy fixed at the Ni $\mathrm{L_3}$ absorption maximum. At this photon energy and with an X-ray bandwidth of 3 eV the XMCD signal essentially corresponds to the integral over the $\mathrm{L_3}$ absorption edge. The XMCD signal measures selectively the Ni magnetic properties [50], [370], [371]. From the curve we find that it takes 120 ± 70 fs to quench the ferromagnetic order as determined from fitting the data to a three-temperature model of energy transfer between electron, spin and lattice reservoirs (line in Fig. 38) [366].

In $3d$ transition metals sum rules relate the integral L_3 XMCD signal to a linear combination of spin, S, and orbital, L, angular momentum components along the magnetization direction as $S + (3/2)L$ [50], [370], [371]. The temporal evolution of $S + (3/2)L$ in Fig. 38 represents the first direct demonstration that S is transferred to the lattice on a 300 fs timescale and not to L. This can be visualized for the following scenario, considering that in thermal equilibrium (at negative time delays in Fig. 38) L is typically only about 20% of S [50], [370], [371]. The 80% decrease of $S + (3/2)L$ during the first ps is then mainly due to the reduction of S. If this change in S were to be completely compensated by L, the quantity $S + (3/2)L$ would actually increase by about 20% in contradiction to the measurements. At present we cannot rule out a partial angular momentum transfer to L cannot be ruled out, but its contribution would have to be below ∼10% of S to keep $S + (3/2)L$ within the statistical uncertainty in Fig. 38. One can therefore conclude that the data in Fig. 38 are only compatible with a substantial femtosecond spin angular momentum transfer to the lattice, i.e., a fs spin-lattice relaxation.

These findings demonstrate that the absorption of an intense fs laser pulse opens up a novel ultrafast spin-lattice relaxation channel. This relaxation process was unambiguously established to proceed on a 120 ± 70 fs timescale by probing the evolution of spin and orbital angular momentum with polarized fs soft X-ray pulses.

VIII. Conclusion and Perspectives

This contribution highlights the versatility of synchrotron radiation to the study of contemporary problems in magnetism. Using the unique properties of synchrotron radiation, it is possible to extract very detailed information about a magnetic system, ranging from the spin structure to the electronic states, and extending from the static magnetization configuration up to excitations on the femtosecond timescale. As a particular feature of the synchrotron radiation approach to magnetism, both ferromagnetic and antiferromagnetic spin orderings can be studied on an equal footing by exploiting circular and linear magnetodichroic phenomena in transmission and reflection, thus providing an unparalleled access to magnetic

heterostructures and hybrid systems. Magnetic proximity effects at interfaces can be addressed nowadays in a very detailed manner. The sensitivity to interfaces may be even increased in future experiments by implementing X-ray standing wave (XSW) techniques [372], [373].

The current microscopy approaches using synchrotron light already offer a lateral resolution down to the 20 nm regime. Very soon this limit may be pushed further down by the use of aberration-corrected electron optics [374], [375] and improved X-ray optical systems [324]. Also alternative concepts are explored, such as the detection of photoexcited electrons with a scanning tunneling microscope [376]. We may therefore expect to be able in the near future to obtain element-specific magnetic information on much smaller length scales than accessible today.

The intrinsic time structure of the synchrotron radiation from storage ring facilities has already enabled a variety of novel spectroscopic and imaging approaches to the high-frequency dynamics in magnetic systems. The current time-resolution for most of the experiments lies in the 10 ps regime and is limited mainly by the width of the probing synchrotron light pulse rather than by other experimental constraints. These experiments usually probe the reversible dynamic processes in the ferromagnet, because the accumulation of many repetitions $(\sim 10^9)$ of the pump-probe cycle is needed to obtain a sufficient signal-to-noise ratio.

A significant improvement of the situation is expected by the use of shorter X-ray pulses, which may be provided by peculiar timing schemes in storage ring facilities (“femtosecond slicing” [377]) or may be generated in free-electron lasers [25]. Provided that the high peak intensity of the pulses can be controlled to avoid sample damage and appropriate detectors are available, even a “one-shot imaging” of a dynamic process may come within reach. This will open a completely new avenue to study fluctuations and space-time correlations in a spin system and to separate deterministic from stochastic processes. A recent experiment on a patterned solid-state sample has demonstrated the feasibility of ultrafast diffractive imaging. The image was successfully captured within the first 25 fs of a single light pulse from the source FLASH (Hamburg), before the sample started to deteriorate due to the large amount of energy absorbed [278]. An additional property of the FEL radiation is the high degree of coherence, which will also enable new concepts for holography experiments.

ACKNOWLEDGMENT

This review is based on the work performed by many groups at various synchrotron radiation sources. Therefore, the authors would first like to thank the following members of their teams: M. Albrecht, E. Amaladass, Z. Bandic, S. Blügel, S. Bornemann, C. Brombacher, L. I. Chelaru, S. Cramm, L. Dobisz, W. Eberhardt, H. Ebert, T. Eichhorn, C. S. Fadley, S. Fiedler, K. Fukumoto, L. Glaser, H. Gomonaj, C. M. Günther, M. W. Haverkort, O. Hellwig, G. Jakob, M. Kallmayer, D. Kercher, J. Kirschner, M. Kotsugi, I. P. Krug, T. Lau, S. Lounis, D. Makarov, P. Mavropoulos, A. Menzel, J. Minar, M. Müller, A. Nevedov, F. Offi, B. Pfau, F. Radu, R. Rick, M. Reif, W. F. Schlotter, A. Tanaka, L.-H. Tjeng, T. Tyliszczak, J. Wang, and H. Yang. They also would like to acknowledge collaborations with the Stanford Synchrotron Radiation Laboratory, Hitachi Global Storage Technologies (HGST, San Jose Research Center, USA), and the University of Konstanz. Thanks are due to the staff members of the ALS (Berkeley), BESSY (Berlin), BNL (Brookhaven), DELTA (Dortmund), ESRF (Grenoble), and SLS (Villingen) for the support during the experiments, and to B. Zada and W. Mahler for technical assistance.

Financial support by the Deutsche Forschungsgemeinschaft through SFB 491 and SFB 668, the German Minister for Education and Research (BMBF) through Grants 05 SL8EF19, 05 KS7PC1, and 05 KS4 KEB/5, as well as by the Landesstiftung Baden-Württemberg and the European Community is gratefully acknowledged. The Advanced Light Source is supported by the Director, Office of Science, Office of Basic Energy Sciences, of the U.S. Department of Energy under Contract DE-AC02-05CH11231.

The authors are indebted to L. Snyders for her help with typesetting the manuscript.

REFERENCES

[1] M. Faraday, “On the magnetization of light and the illumination of magnetic lines of force,” *Phil. Trans. R. Soc. Lond.*, vol. 136, pp. 1–20, 1846.

[2] A. Hubert and R. Schäfer, *Magnetic Domains*. Berlin, Germany: Springer-Verlag, 1998.

[3] M. R. Freeman and W. K. Hiebert, “Stroboscopic microscopy of magnetic dynamics,” in *Spin Dynamics in Confined Magnetic Structures*, B. Hillebrands and K. Ounadjela, Eds. Berlin, Germany: Springer-Verlag, 2002, p. 93.

[4] M. Mansuripur, *The Physical Principles of Magneto-Optical Recording*. Cambridge, U.K.: Cambridge Univ. Press, 1998.

[5] S. F. Alvarado, W. Eib, F. Meier, H. C. Siegmann, and P. Zürcher, “Spin-polarized photoemission,” in *Photoemission and the Electronic Properties of Surfaces*, B. Feuerbacher, B. Fitton, and R. F. Willis, Eds. New York: Wiley, 1978.

[6] R. Clauberg, W. Gudat, E. Kisker, E. Kuhlmann, and G. M. Rothberg, “Nature of the resonant 6-eV satellite in Ni: Photoelectron spin-polarization analysis,” *Phys. Rev. Lett.*, vol. 47, pp. 1314–1317, 1981.

[7] B. T. Thole, G. van der Laan, and G. A. Sawatzky, “Strong magnetic dichroism predicted in the $\mathrm{M}_{4,5}$ X-ray absorption spectra of magnetic rare-earth materials,” *Phys. Rev. Lett.*, vol. 55, pp. 2086–2088, 1985.

[8] G. van der Laan, B. T. Thole, G. A. Sawatzky, J. B. Goedkoop, J. C. Fuggle, J. M. Esteva, R. Karnatak, J. P. Remeika, and H. A. Dabkowska, “Experimental proof of magnetic X-ray dichroism,” *Phys. Rev. B*, vol. 34, pp. 6529–6531, 1986.

[9] G. Schütz, W. Wagner, W. Wilhelm, P. Kienle, R. Zeller, R. Frahm, and G. Materlik, “Absorption of circularly polarized x rays in iron,” *Phys. Rev. Lett.*, vol. 58, pp. 737–740, 1987.

[10] C. T. Chen, F. Sette, Y. Ma, and S. Modesti, “Soft-X-ray magnetic circular dichroism at the $\mathrm{L}_{2,3}$ edges of Nickel,” *Phys. Rev. B*, vol. 42, pp. 7262–7265, 1990.

[11] L. Baumgarten, C. M. Schneider, F. Schäfers, H. Petersen, and J. Kirschner, “Magnetic X-ray dichroism in core-level photoemission from ferromagnets,” *Phys. Rev. Lett.*, vol. 65, pp. 492–495, 1990.

[12] C. M. Schneider, M. S. Hammond, P. Schuster, A. Cebollada, R. Miranda, and J. Kirschner, “Observation of magnetic circular dichroism in uv photoemission from ferromagnetic fcc cobalt films,” *Phys. Rev. B*, vol. 44, pp. 12066–12069, 1991.

[13] W. Kuch and C. M. Schneider, “Magnetic dichroism in valence band photoemission,” *Rep. Prog. Phys.*, vol. 64, pp. 147–203, 2001.

[14] J. Stöhr, Y. Wu, M. G. Samant, B. D. Hermsmeier, G. Harp, S. Koranda, D. Dunham, and B. P. Tonner, “Element-specific magnetic microscopy with circularly polarized X-rays,” *Science*, vol. 259, pp. 658–660, 1993.

[15] C. M. Schneider, K. Holldack, M. Kinzler, M. Grunze, H. P. Oepen, F. Schäfers, H. Petersen, K. Meinel, and J. Kirschner, “Magnetic properties of transition-metal multilayers studied with X-ray magnetic circular dichroism spectroscopy,” *Appl. Phys. Lett.*, vol. 63, pp. 2432–2435, 1993.

[16] P. Fischer, G. Schütz, G. Schmahl, P. Guttmann, and D. Raasch, “Imaging of magnetic domains with the X-ray microscope at BESSY using X-ray magnetic circular dichroism,” *Z. Phys. B*, vol. 101, pp. 313–316, 1996.

[17] C.-C. Kao, C. T. Chen, E. D. Johnson, J. B. Hastings, H. J. Lin, G. H. Ho, G. Meigs, J.-M. Brot, S. L. Hulbert, Y. U. Idzerda, and C. Vettier, "Dichroic interference effects in circularly polarized soft-X-ray resonant magnetic scattering," *Phys. Rev. B*, vol. 50, pp. 9599–9602, 1994.

[18] E. Gerdau, R. Rüffer, H. Winkler, W. Tolksdorf, C. P. Klages, and J. P. Hannon, "Nuclear Bragg diffraction of synchrotron radiation in yttrium iron garnet," *Phys. Rev. Lett.*, vol. 54, pp. 835–838, 1985.

[19] R. Röhlsberger, J. Bansmann, V. Senz, K. L. Jonas, A. Bettac, O. Leupold, R. Rüffer, E. Burkel, and K. H. Meiwes-Broer, "Perpendicular spin orientation in ultrasmall Fe islands on W(110)," *Phys. Rev. Lett.*, vol. 86, pp. 5597–5600, 2001.

[20] R. Röhlsberger, "Nuclear condensed matter physics with synchrotron radiation—Basic principles, methodology and applications," in *Springer Tracts in Modern Physics*. Berlin, Germany: Springer-Verlag, 2004, vol. 208.

[21] S. Eisebitt, J. Lüning, W. F. Schlotter, M. Lörgen, O. Hellwig, W. Eberhardt, and J. Stöhr, "Lensless imaging of magnetic nanostructures by X-ray spectro-holography," *Nature*, vol. 432, pp. 885–888, 2004.

[22] *Handbook on Synchrotron Radiation*, D. Eastman and Y. Farge, Eds. Amsterdam, The Netherlands: North-Holland, 1983.

[23] F. Schäfers, W. Peatman, A. Eyers, C. Heckenkamp, G. Schönhense, and U. Heinzmann, "High-flux normal incidence monochromator for circularly polarized synchrotron radiation," *Rev. Sci. Instrum.*, vol. 57, pp. 1032–1041, 1985.

[24] D. Attwood, K. Halbach, and K.-J. Kim, "Tunable coherent X-rays," *Science*, vol. 228, pp. 1265–1272, 1985.

[25] V. Ayvazyan, N. Baboi, J. Bähr, V. Balandin, B. Beutner, A. Brandt, I. Bohnet, A. Bolzmann, R. Brinkmann, O. I. Brovko, J. P. Carneiro, S. Casalbuoni, M. Castellano, P. Castro, L. Catani, E. Chiadroni, S. Choroba, A. Cianchi, H. Delsim-Hashemi, G. Di Pirro, M. Dohlus, S. Düsterer, H. T. Edwards, B. Faatz, A. A. Fateev, J. Feldhaus, K. Flöttmann, J. Frisch, L. Fröhlich, T. Garvey, U. Gensch, N. Golubeva, H. J. Grabosch, B. Grigoryan, O. Grimm, U. Hahn, J. H. Han, M. V. Hartrott, K. Honkavaara, M. Hüning, R. Ischebeck, E. Jaeschke, M. Jablonka, R. Kammering, V. Katalev, B. Keitel, S. Khodyachykh, Y. Kim, V. Kocharyan, M. Körfer, M. Kollewe, D. Kostin, D. Krämer, M. Krassilnikov, G. Kube, L. Lilje, T. Limberg, D. Lipka, F. Löhl, M. Luong, C. Magne, J. Menzel, P. Michelato, V. Miltchev, M. Minty, W. D. Möller, L. Monaco, W. Müller, M. Nagl, O. Napoly, P. Nicolosi, D. Nölle, T. Nuñez, A. Oppelt, C. Pagani, R. Paparella, B. Petersen, B. Petrosyan, J. Pflüger, P. Piot, E. Plönjes, L. Poletto, D. Proch, D. Pugachov, K. Rehlich, D. Richter, S. Riemann, M. Ross, J. Rossbach, M. Sachwitz, E. L. Saldin, W. Sandner, H. Schlarb, B. Schmidt, M. Schmitz, P. Schmüser, J. R. Schneider, E. A. Schneidmiller, H. J. Schreiber, S. Schreiber, A. V. Shabunov, D. Sertore, S. Setzer, S. Simrock, E. Sombrowski, L. Staykov, B. Steffen, F. Stephan, F. Stulle, K. P. Sytchev, H. Thom, K. Tiedtke, M. Tischer, R. Treusch, D. Trines, I. Tsakov, A. Vardanyan, R. Wanzenberg, T. Weiland, H. Weise, M. Wendt, I. Will, A. Winter, K. Wittenburg, M. V. Yurkov, I. Zagorodnov, P. Zambolin, and K. Zapfe, "First operation of a free-electron laser generating GW power radiation at 32 nm wavelength," *Eur. Phys. J. D*, vol. 37, pp. 297–304, 2006.

[26] W. Ackermann, G. Asova, V. Ayvazyan, A. Azima, N. Baboi, J. Bähr, V. Balandin, B. Beutner, A. Brandt, A. Bolzmann, R. Brinkmann, O. I. Brovko, M. Castellano, P. Castro, L. Catani, E. Chiadroni, S. Choroba, A. Cianchi, J. T. Costello, D. Cubaynes, J. Dardis, W. Decking, H. Delsim-Hashemi, A. Delserieys, G. D. Pirro, M. Dohlus, S. Düsterer, A. Eckhardt, H. T. Edwards, B. Faatz, J. Feldhaus, K. Flöttmann, J. Frisch, L. Fröhlich, T. Garvey, U. Gensch, C. Gerth, M. Görler, N. Golubeva, H.-J. Grabosch, M. Grecki, O. Grimm, K. Hacker, U. Hahn, J. H. Han, K. Honkavaara, T. Hott, M. Hüning, Y. Ivanisenko, E. Jaeschke, W. Jalmuzna, T. Jezynski, R. Kammering, V. Katalev, K. Kavanagh, E. T. Kennedy, S. Khodyachykh, K. Klose, V. Kocharyan, M. Körfer, M. Kollewe, W. Koprek, S. Korepanov, D. Kostin, M. Krassilnikov, G. Kube, M. Kuhlmann, C. L. S. Lewis, L. Lilje, T. Limberg, D. Lipka, F. Löhl, H. Luna, M. Luong, M. Martins, M. Meyer, P. Michelato, V. Miltchev, W. D. Möller, L. Monaco, W. F. O. Müller, O. Napieralski, O. Napoly, P. Nicolosi, D. Nölle, T. Nuñez, A. Oppelt, C. Pagani, R. Paparella, N. Pchalek, J. Pedregosa-Gutierrez, B. Petersen, B. Petrosyan, G. Petrosyan, L. Petrosyan, J. Pflüger, E. Plönjes, L. Poletto, K. Pozniak, E. Prat, D. Proch, P. Pucyk, P. Radcliffe, H. Redlin, K. Rehlich, M. Richter, M. Roehrs, J. Roensch, R. Romaniuk, M. Ross, J. Rossbach, V. Rybnikov, M. Sachwitz, E. L. Saldin, W. Sandner, H. Schlarb, B. Schmidt, M. Schmitz, P. Schmüser, J. R. Schneider, E. A. Schneidmiller, S. Schnepp, S. Schreiber, M. Seidel, D. Sertore, A. V. Shabunov, C. Simon, S. Simrock, E. Sombrowski, A. A. Sorokin, P. Spanknebel, R. Spesyvtsev, L. Staykov, B. Steffen, F. Stephan, F. Stulle, H. Thom, K. Tiedtke, M. Tischer, S. Toleikis, R. Treusch, D. Trines, I. Tsakov, E. Vogel, T. Weiland, H. Weise, M. Wellhöfer, M. Wendt, I. Will, A. Winter, K. Wittenburg, W. Wurth, P. Yeates, M. V. Yurkov, I. Zagorodnov, and K. Zapfe, "Peak brilliance of X-ray FELs in comparison with third-generation synchrotron-radiation light sources," *Nature Photon.*, vol. 1, pp. 336–342, 2007.

[27] S. S. P. Parkin, C. Kaiser, A. Panchula, P. M. Rice, B. Hughes, M. Samant, and S.-H. Yang, "Giant tunneling magnetoresistance at room temperature with MgO(100) tunnel barriers," *Nature Mater.*, vol. 3, pp. 862–867, 2004.

[28] S. Yuasa, T. Nagahama, A. Fukushima, Y. Suzuki, and K. Ando, "Giant room-temperature magnetoresistance in single-crystal Fe/MgO/Fe magnetic tunnel junctions," *Nature Mater.*, vol. 3, pp. 868–871, 2004.

[29] W. H. Butler, X.-G. Zhang, T. C. Schulthess, and J. M. MacLaren, "Spin-dependent tunneling conductance of Fe-MgO-Fe sandwiches," *Phys. Rev. B*, vol. 63, pp. 054416-1–054416-12, 2001.

[30] J. Mathon and A. Umerski, "Theory of tunneling magnetoresistance of an epitaxial Fe/MgO/Fe(001) junction," *Phy. Rev. B*, vol. 63, pp. 220403-1–220403-4, 2001.

[31] M. Bowen, V. Cros, F. Petroff, A. Fert, C. M. Boubeta, J. L. Costa-Kramer, J. V. Anguita, A. Cebollada, F. Briones, J. M. de Teresa, L. Morellon, M. R. Ibarra, F. Guell, F. Peiro, and A. Cornet, "Large magnetoresistance in Fe/MgO/FeCo(001) epitaxial tunnel junctions on GaAs(001)," *Appl. Phys. Lett.*, vol. 79, pp. 1655–1657, 2001.

[32] J. Faure-Vincent, C. Tiusan, E. Jouguelet, F. Canet, M. Sajieddine, C. Bellouard, E. Popova, M. Hehn, F. Montaigne, and A. Schuhl, "High tunnel magnetoresistance in epitaxial Fe/MgO/Fe tunnel junctions," *Appl. Phys. Lett.*, vol. 82, pp. 4507–4509, 2003.

[33] S. Yuasa, A. Fukushima, T. Nagahama, K. Ando, and Y. Suzuki, "High tunnel magnetoresistance at room temperature in fully epitaxial Fe/MgO/Fe tunnel junctions due to coherent spin-polarized tunneling.," *Jpn. J. Appl. Phys.*, vol. 43, pp. L588–L590, 2004.

[34] M. Müller, F. Matthes, and C. M. Schneider, "Spin polarization at ferromagnet-insulator interfaces: The important role of stoichiometry in MgO/Fe(001)," *EPL*, vol. 80, pp. 17007-1–17007-6, 2007.

[35] V. E. Henrich and P. A. Cox, *The Surface Science of Metal Oxides*. Cambridge, U.K.: Cambridge Univ. Press, 1994.

[36] M. Sterrer, M. Heyde, M. Novicki, N. Nilius, T. Risse, H. P. Rust, G. Pacchioni, and H. J. Freund, *J. Phys. Chem. B*, vol. 110, pp. 46–49, 2006.

[37] A. Gibson, R. Haydock, and J. LaFemina, "Stability of vacancy defects in MgO: The role of charge neutrality," *Phys. Rev. B.*, vol. 50, pp. 2582–2592, 1994.

[38] B. M. Klein, W. E. Pickett, L. L. Boyer, and R. Zeller, "Theory of F centers in the alkaline-earth oxides MgO and CaO," *Phys. Rev. B.*, vol. 35, pp. 5802–5815, 1986.

[39] X.-G. Zhang and W. H. Butler, "Large magnetoresistance in bcc Co/MgO/Co and FeCo/MgO/FeCo tunnel junctions," *Phys. Rev. B*, vol. 70, pp. 172407-1–172407-4, 2004.

[40] C. Roth, F. U. Hillebrecht, H. Rose, and E. Kisker, "Linear magnetic dichroism in angular resolved Fe 3p core level photoemission," *Phys. Rev. Lett.*, vol. 70, pp. 3479–3482, 1993.

[41] M. Getzlaff, C. Ostertag, G. H. Fecher, N. A. Cherepkov, and G. Schönhense, "Magnetic dichroism in photoemission with unpolarized light," *Phys. Rev. Lett.*, vol. 73, pp. 3030–3033, 1994.

[42] L. Plucinski, Y. Zhao, B. Sinkovic, and E. Vescovo, "MgO/Fe(100) interface: A study of the electronic structure," *Phys. Rev. B*, vol. 75, pp. 214411-1–214411-8, 2007.

[43] B. Sinkovic, P. D. Johnson, N. B. Brookes, A. Clarke, and N. V. Smith, "Spin-polarized core-level photoemission of oxidized Fe(001)," *J. Appl. Phys.*, vol. 70, pp. 5918–5920, 1991.

[44] M. Kurth, P. C. J. Graat, and E. J. Mittemeijer, "Determination of the intrinsic bulk and surface plasmon intensity of XPS spectra of magnesium," *Appl. Surf. Sci.*, vol. 220, pp. 60–78, 2003.

[45] [Online]. Available: http://www.nobelprize.org/nobel_prizes/physics/laureates/2007/

[46] G. Binasch, P. Grünberg, F. Saurenbach, and W. Zinn, "Enhanced magnetoresistance in layered magnetic structures with antiferromagnetic interlayer exchange," *Phys. Rev. B*, vol. 39, pp. 4828–4830, 1989.

[47] M. N. Baibich, J. M. Broto, A. Fert, F. Nguyen van Dau, F. Petroff, P. Eitenne, G. Creuzet, A. Friederich, and J. Chazelas, "Giant magnetoresistance of (001)Fe/(001)Cr magnetic superlattices," *Phys. Rev. Lett.*, vol. 61, pp. 2472–2475, 1988.

[48] P. Grünberg, R. Schreiber, Y. Pang, M. B. Brodsky, and H. Sowers, "Layered magnetic structures: Evidence for antiferromagnetic coupling of Fe layers across Cr interlayers," *Phys. Rev. Lett.*, vol. 57, pp. 2442–2445, 1986.

[49] J. L. Erskine and E. A. Stern, "Calculation of the M_{23} magneto-optical absorption spectrum of ferromagnetic nickel," *Phys. Rev. B*, vol. 12, pp. 5016–5024, 1975.

[50] B. T. Thole, P. Carra, F. Sette, and G. van der Laan, "X-ray circular dichroism as a probe of orbital magnetization," *Phys. Rev. Lett.*, vol. 68, pp. 1943–1946, 1992.

[51] P. Carra, B. T. Thole, M. Altarelli, and X. Wang, "X-ray circular dichroism and local magnetic fields," *Phys. Rev. Lett.*, vol. 70, pp. 694–697, 1993.

[52] R. Wienke, G. Schütz, and H. Ebert, "Determination of local magnetic moments of 5d impurities in Fe detected via spin-dependent absorption," *J. Appl. Phys.*, vol. 69, pp. 6147–6149, 1991.

[53] G. Schütz, M. Knülle, and H. Ebert, "Magnetic circular X-ray dichroism and its relation to local moments," *Phys. Scr.*, vol. T49A, pp. 302–306, 1993.

[54] P. Strange, "Magnetic absorption dichroism and sum rules in itinerant magnets," *J. Phys.: Condens. Mater.*, vol. 6, pp. L491–L495, 1994.

[55] C. T. Chen, Y. U. Idzerda, H.-J. Lin, N. V. Smith, G. Meigs, E. Chaban, G. H. Ho, E. Pellegrin, and F. Sette, "Experimental confirmation of the X-ray magnetic circular dichroism sum rules for iron and cobalt," *Phys. Rev. Lett.*, vol. 75, pp. 152–155, 1995.

[56] A. L. Ankudinov and J. J. Rehr, "Sum rules for polarization-dependent X-ray absorption," *Phys. Rev. B*, vol. 51, pp. 1282–1285, 1995.

[57] Y. Teramura, A. Tanaka, and T. Jo, "Effect of Coulomb interaction on the X-ray magnetic circular dichroism spin sum rule in $3d$ transition elements," *J. Phys. Soc. Jpn.*, vol. 65, pp. 1053–1055, 1996.

[58] A. L. Ankudinov, J. J. Rehr, H. Wende, A. Scherz, and K. Baberschke, "Spin-dependent sum rules for X-ray absorption spectra," *Europhys. Lett.*, vol. 66, pp. 441–447, 2004.

[59] H. Ebert, "Circular magnetic X-ray dichroism in transition metal systems," in *Spin-Orbit-Influenced Spectroscopies of Magnetic Solids*, H. Ebert and G. Schütz, Eds. New York: Springer, 1996, pp. 159–178.

[60] H. Ebert, "Magneto-optical effects in transition metal systems," *Rep. Prog. Phys.*, vol. 59, pp. 1665–1735, 1996.

[61] J. Stöhr and H. König, "Determination of spin- and orbital-moment anisotropies in transition metals by angle-dependent X-ray magnetic circular dichroism," *Phys. Rev. Lett.*, vol. 75, pp. 3748–3751, 1995.

[62] A. I. Nesvizhskii, A. L. Ankudinov, and J. J. Rehr, "Normalization and convergence of X-ray absorption sum rules," *Phys. Rev. B*, vol. 63, pp. 094412-1–094412-5, 2001.

[63] C. Kittel, "On the gyromagnetic ratio and spectroscopic splitting factor of ferromagnetic substances," *Phys. Rev.*, vol. 76, pp. 743–748, 1949.

[64] C. Kittel, "Ferromagnetic resonance," *J. Phys. Rad.*, vol. 12, pp. 291–302, 1951.

[65] H. Wende, "Recent advances in X-ray absorption spectroscopy," *Rep. Prog. Phys.*, vol. 67, pp. 2105–2181, 2004.

[66] G. van der Laan, "Line shape of 2p magnetic-X-ray-dichroism spectra in 3D metallic systems," *Phys. Rev B*, vol. 55, pp. 8086–8089, 1997.

[67] H. Wende, M. Bernien, J. Luo, C. Sorg, N. Ponpandian, J. Kurde, J. Miguel, M. Piantek, X. Xu, P. Eckhold, W. Kuch, K. Baberschke, P. M. Panchmatia, B. Sanyal, P. M. Oppeneer, and O. Eriksson, "Substrate-induced magnetic ordering and switching of iron porphyrin molecules," *Nature Mater.*, vol. 6, pp. 516–520, 2007.

[68] M. Bernien, X. Xu, J. Miguel, M. Piantek, P. Eckhold, J. Luo, J. Kurde, W. Kuch, K. Baberschke, H. Wende, and P. Srivastava, "Fe-porphyrin monolayers on ferromagnetic substrates: Electronic structure and magnetic coupling strength," *Phys. Rev. B*, vol. 76, pp. 214406-1–214406-6, 2007.

[69] H. Wende, A. Scherz, C. Sorg, K. Baberschke, E. K. U. Gross, H. Appel, K. Burke, J. Minár, H. Ebert, A. L. Ankudinov, and J. J. Rehr, "XMCD analysis beyond standard procedures," in *Proc. AIP Conf.*, 2007, vol. 882, pp. 78–82.

[70] A. Scherz, H. Wende, and K. Baberschke, "Fine structure of X-ray magnetic circular dichroism for early 3 d transition metals," *Appl. Phys. A*, vol. 78, pp. 843–846, 2004.

[71] A. Scherz, H. Wende, C. Sorg, K. Baberschke, J. Minár, D. Benea, and H. Ebert, "Limitations of integral XMCD sum-rules for the early 3d elements," *Physica Scripta*, vol. T115, pp. 586–588, 2005.

[72] A. Scherz, E. K. U. Gross, H. Appel, C. Sorg, K. Baberschke, H. Wende, and K. Burke, "Measuring the Kernel of time-dependent density functional theory with X-ray absorption spectroscopy of 3d transition metals," *Phys. Rev. Lett.*, vol. 95, pp. 253006-1–253006-4, 2005.

[73] F. Heusler, W. Starck, and E. Haupt, "Über die ferromagnetischen Eigenschaften von Legierungen unmagnetischer Metalle," *Verh. Deutsch. Phys. Ges.*, vol. 5, p. 220, 1903.

[74] I. Galanakis, P. Mavropoulos, and P. H. Dederichs, "Electronic structure and Slater-Pauling behaviour in half-metallic Heusler alloys calculated from first principles," *J. Phys. D: Appl. Phys.*, vol. 39, pp. 765–775, 2006.

[75] H. C. Kandpal, G. H. Fecher, and C. Felser, "Calculated electronic and magnetic properties of the half-metallic transition metal based Heusler compounds," *J. Phys. D: Appl. Phys.*, vol. 40, pp. 1507–1523, 2007.

[76] J. M. D. Coey, M. Venkatesan, and M. A. Bari, "Half-metallic ferromagnets," in *Lecture Notes in Physics*, C. Berthier, L. P. Levy, and G. Martinez, Eds. Heidelberg, Germany: Springer, 2002, vol. 595.

[77] N. Tezuka, N. Ikeda, S. Sugimoto, and K. Inomata, "175% tunnel magnetoresistance at room temperature and high thermal stability using $Co_2FeAl_{2FeAl0.5Si0.5}Si_{0.5}$ full-Heusler alloy electrodes," *Appl. Phys. Lett.*, vol. 89, pp. 252508-1–252508-3, 2006.

[78] K. Inomata, S. Okamura, A. Miyazaki, M. Kikuchi, N. Tezuka, M. Wojcik, and E. Jedryka, "Structural and magnetic properties and tunnel magnetoresistance for $Co_2(Cr, Fe)Al$ and Co_2FeSi full-Heusler alloys," *J. Phys. D: Appl. Phys.*, vol. 39, pp. 816–823, 2006.

[79] D. Ebke, J. Schmalhorst, N. N. Liu, A. Thomas, G. Reiss, and A. Hütten, "Large tunnel magnetoresistance in tunnel junctions with Co_2MnSi/Co_2FeSi multilayer electrode," *Appl. Phys. Lett.*, vol. 89, pp. 162506-1–162506-3, 2006.

[80] T. Marukame, T. Ishikawa, S. Hakamata, K. Matsuda, T. Uemura, and M. Yamamoto, "Highly spin-polarized tunneling in fully epitaxial $Co_2Cr_{0.6}Fe_{0.4}Al/MgO/Co_{50}Fe_{50}$ magnetic tunnel junctions with exchange biasing," *Appl. Phys. Lett.*, vol. 90, pp. 012508-1–012508-3, 2007.

[81] A. D. Rata, H. Braak, D. E. Bürgler, and C. M. Schneider, "Large inverse tunneling magnetoresistance in $Co_2Cr_{0.6}Fe_{0.4}Al/MgO/Co_{80}Fe_{20}$ magnetic tunnel junctions," *Appl. Phys. Lett.*, vol. 90, p. 162512, 2007.

[82] A. Conca, M. Jourdan, and H. Adrian, "Epitaxy of thin films of the Heusler compound $Co_2Cr_{0.6}Fe_{0.4}Al$," *J. Phys. D: Appl. Phys.*, vol. 40, pp. 1534–1538, 2007.

[83] K. Ullakko, J. K. Huang, C. Kantner, R. C. O'Handley, and V. V. Kokorin, "Large magnetic-field-induced strains in Ni_2MnGa single crystals," *Appl. Phys. Lett.*, vol. 69, pp. 1966–1968, 1996.

[84] A. Sozinov, A. A. Likhachev, N. Lanska, and K. Ullakko, "Giant magnetic-field-induced strain in NiMnGa seven-layered martensitic phase," *Appl. Phys. Lett.*, vol. 80, pp. 1746–2748, 2002.

[85] H. Morito, A. Fujita, K. Oikawa, K. Ishida, K. Fukamichi, and R. Kainuma, "Stress-assisted magnetic-field-induced strain in NiFeGaCo ferromagnetic shape memory alloys," *Appl. Phys. Lett.*, vol. 90, pp. 062505-1–062505-3, 2007.

[86] Z. D. Han, D. H. Wang, C. L. Zhang, S. L. Tang, B. X. Gu, and Y. W. Du, "Large magnetic entropy changes in the $Ni_{45.4}Mn_{41.5}In_{13.1}$ ferromagnetic shape memory alloy," *Appl. Phys. Lett.*, vol. 89, pp. 182507-1–182507-3, 2006.

[87] J. Grabis, A. Bergmann, A. Nefedov, K. Westerholt, and H. Zabel, "Element-specific characterization of the interface magnetism in $(Co_2MnGe/Au)n$ multilayers by X-ray resonant magnetic scattering," *Phys. Rev. B*, vol. 72, pp. 024438-1–024438-11, 2005.

[88] M. Kallmayer, H. Schneider, G. Jakob, H. Elmers, K. Kroth, H. Kandpal, U. Stumm, and C. Cramm, "Reduction of surface magnetism of $Co_2Cr_{0.6}Fe_{0.4}Al$ Heusler alloy films," *Appl. Phys. Lett.*, vol. 88, pp. 072506-1–072506-3, 2006.

[89] M. Kallmayer, H. Schneider, G. Jakob, H. Elmers, B. Balke, and S. Cramm, "Interface magnetization of ultrathin epitaxial $Co_2FeSi(110)/Al_2O_3$ films," *J. Phys. D: Appl. Phys.*, vol. 40, pp. 1552–1557, 2007.

[90] M. Kallmayer, K. Hild, T. Eichhorn, H. Schneider, G. Jakob, A. Conca, M. Jourdan, H. Elmers, A. Gloskovskii, S. Schuppler, and P. Nagel, "Solid state reaction at the interface between Heusler alloys and Al cap accelerated by elevated temperature and rough surface," *Appl. Phys. Lett.*, vol. 91, pp. 192501-1–192501-3, 2007.

[91] G. Jakob, T. Eichhorn, M. Kallmayer, and H. J. Elmers, "Correlation of electronic structure and martensitic transition in epitaxial Ni_2MnGa films," *Phys. Rev. B*, vol. 76, pp. 174407-1–174407-6, 2007.

[92] H. J. Elmers, G. H. Fecher, D. Valdaitsev, S. A. Nepijko, A. Gloskovskii, G. Jakob, G. Schönhense, S. Wurmehl, T. Block, C. Felser, P.-C. Hsu, W.-L. Tsai, and S. Cramm, "Element-specific magnetic moments from core-absorption magnetic circular dichroism of the doped Heusler alloy $Co_2Cr_{0.6}Fe_{0.4}Al$," *Phys. Rev. B*, vol. 67, pp. 104412-1–104412-8, 2003.

[93] A. Conca, M. Jourdan, and H. Adrian, "Epitaxy of thin films of the Heusler compound," *J. Crystal Growth*, vol. 299, pp. 299–302, 2007.

[94] G. A. Botton, G. Y. Guo, W. M. Temmerman, and C. J. Humphreys, "Experimental and theoretical study of the electronic structure of Fe, Co, and Ni aluminides with the B2 structure," *Phys. Rev. B*, vol. 54, pp. 1682–1691, 1996.

[95] Y. S. Lee, C. H. Lee, K. W. Kim, H. J. Shin, and Y. P. Lee, "Hybridization effects and charge transfer in ordered and disordered Co_xAl_{1-x} alloy films," *J. Magn. Magn. Mater.*, vol. 272–276, pp. 2151–2153, 2004.

[96] O. Söderberg, Y. Ge, A. Sozinov, S.-P. Hannula, and V. K. Lindroos, "Recent breakthrough development of the magnetic shape memory effect in NiMnGa alloys," *Smart Mater. Struct.*, vol. 14, pp. S223–S235, 2005.

[97] P. Entel, V. D. Bucheinikov, V. V. Khovaillo, A. T. Zayak, W. A. Adeagbo, M. E. Gruner, H. C. Herper, and E. F. Wassermann, "Modelling the phase diagram of magnetic shape memory Heusler alloys," *J. Phys. D-Appl. Phys.*, vol. 39, pp. 865–889, 2006.

[98] S. R. Barman, S. Banik, and A. Chakrabarti, "Structural and electronic properties of Ni_2MnGa," *Phys. Rev. B*, vol. 72, pp. 184410-1–184410-5, 2005.

[99] A. T. Zayak, P. Entel, J. Enkovaara, and R. M. Nieminen, "First-principles investigations of homogeneous lattice-distortive strain and shuffles in Ni_2MnGa," *J. Phys.: Condens. Matter*, vol. 15, pp. 159–164, 2003.

[100] A. Ayuela, J. Enkovaara, and R. M. Nieminen, "Ab initio study of tetragonal variants in Ni_2MnGa alloy," *J. Phys.: Condens. Matter*, vol. 14, pp. 5325–5336, 2002.

[101] P. Bruno, "Tight-binding approach to the orbital magnetic moment and magnetocrystalline anisotropy of transition-metal monolayers," *Phys. Rev. B*, vol. 39, pp. 865–868, 1989.

[102] D. Weller, J. Stöhr, R. Nakajima, A. Carl, M. G. Samant, C. Chappert, R. Megy, P. Beauvillain, P. Veillet, and G. A. Held, "Microscopic origin of magnetic anisotropy in Au/Co/Au probed with X-ray magnetic circular dichroism," *Phys. Rev. Lett.*, vol. 75, pp. 3752–3755, 1995.

[103] H. A. Dürr and G. van der Laan, "Magnetic circular X-ray dichroism in transverse geometry: A new tool to study the magnetocrystalline anisotropy," *J. Appl. Phys.*, vol. 81, pp. 5355–5357, 1997.

[104] P. Ghigna, A. Campana, A. Lascialfari, A. Caneschi, D. Gatteschi, A. Tagliaferri, and F. Borgatti, "X-ray magnetic-circular-dichroism spectra on the superparamagnetic transition-metal ion clusters Mn_{12} and Fe_8," *Phys. Rev. B*, vol. 64, pp. 132413-1–132413-4, 2001.

[105] R. Moroni, C. Cartier dit Moulin, G. Champion, M. A. Arrio, P. Sainctavit, M. Verdaguer, and D. Gatteschi, "X-ray magnetic circular dichroism investigation of magnetic contributions from Mn(III) and Mn(IV) ions in $Mn_{12} - ac$," *Phys. Rev. B*, vol. 68, pp. 064407-1–064407-7, 2003.

[106] I. Letard, P. Sainctavit, C. C. d. Moulin, J.-P. Kappler, P. Ghigna, D. Gatteschi, and B. Doddi, "Remnant magnetization of Fe_8 high-spin molecules: X-ray magnetic circular dichroism at 300 mK," *J. Appl. Phys.*, vol. 101, pp. 113920-1–113920-6, 2007.

[107] V. Corradini, F. Moro, R. Biagi, U. del Pennino, V. De Renzi, S. Carretta, P. Santini, M. Affronte, J. C. Cezar, G. Timco, and R. E. P. Winpenny, "X-ray magnetic circular dichroism investigation of spin and orbital moments in Cr_8 and Cr_7Ni antiferromagnetic rings," *Phys. Rev. B*, vol. 77, pp. 014402-1–014402-8, 2008.

[108] A. Shavel, B. Rodríguez-González, M. Spasova, M. Farle, and L. M. Liz-Marzán, "Synthesis and characterization of iron/iron oxide core/shell nanocubes," *Adv. Funct. Mater.*, vol. 17, pp. 3870–3876, 2007.

[109] U. Wiedwald, J. Lindner, M. Spasova, Z. Frait, and M. Farle, "Effect of an oxidic overlayer on the magnetism of Co nanoparticles," *Phase Transitions*, vol. 78, pp. 85–104, 2005.

[110] M. Spasova, T. Radetic, N. S. Sobal, M. Hilgendorff, U. Wiedwald, M. Farle, M. Giersig, and U. Dahmen, "Structure and magnetism of Co and CoAg nanocrystals," in *Mat. Res. Soc. Symp. Proc.*, 2002, vol. 721, pp. 195–200.

[111] V. Salgueiriño-Maceira, M. A. Correa-Duarte, A. Hucht, and M. Farle, "One-dimensional assemblies of silica-coated cobalt nanoparticles: Magnetic pearl necklaces," *J. Magn. Magn. Mater.*, vol. 303, pp. 163–166, 2006.

[112] V. Salgueiriño-Maceira, M. A. Correa-Duarte, M. Spasova, L. M. Liz-Marzán, and M. Farle, "Composite silica spheres with magnetic and luminescent functionalities," *Adv. Funct. Mater.*, vol. 16, pp. 509–514, 2006.

[113] S. Kalele, S. W. Gosavi, J. Urban, and S. K. Kulkarni, "Nanoshell particles: Synthesis, properties and applications," *Current Sci.*, vol. 91, pp. 1038–1052, 2006.

[114] B. Lei, S. Han, C. Li, D. Zhang, Z. Liu, and C. Zhou, "Synthesis and electronic properties of transition metal oxide core-shell nanowires," *Nanotechnol.*, vol. 18, pp. 044019-1–044019-8, 2007.

[115] S. J. Rosenthal, J. McBride, S. J. Pennycook, and L. C. Feldman, "Synthesis, surface studies, composition and structural characterization of CdSe, core/shell and biologically active nanocrystals," *Surf. Sci. Rep.*, vol. 62, pp. 111–157, 2007.

[116] D. Dorfs and A. Eychmüller, "Multishell semiconductor nanocrystals," *Z. Phys. Chem.*, vol. 220, pp. 1539–1552, 2006.

[117] D. Ciuculescu, C. Amiens, M. Respaud, A. Falqui, P. Lecante, R. E. Benfield, L. Jiang, K. Fauth, and B. Chaudret, "One-pot synthesis of core-shell FeRh nanoparticles," *Chem. Mater.*, vol. 19, pp. 4624–4626, 2007.

[118] E. L. Bizdoaca, M. Spasoya, M. Farle, M. Hilgendorff, L. M. Liz-Marzán, and F. Caruso, "Self-assembly and magnetism in core-shell microspheres," *J. Vac. Sci. Technol. A*, vol. 21, pp. 1515–1518, 2003.

[119] V. Salgueiriño-Maceira, M. Spasova, and M. Farle, "Water-stable, magnetic silica-cobalt/cobalt oxide-silica multishell submicrometer spheres," *Adv. Funct. Mater.*, vol. 15, pp. 1036–1040, 2005.

[120] M. Spasova, V. Salgueiriño-Maceira, A. Schlachter, M. Hilgendorff, M. Giersig, L. M. Liz-Marzán, and M. Farle, "Magnetic and optical tunable microspheres with a magnetite/gold nanoparticle shell," *J. Mater. Chem.*, vol. 15, pp. 2095–2098, 2005.

[121] Z. Zhang, "Magnetic nanocapsules," *J. Mater. Sci. Technol.*, vol. 23, pp. 1–14, 2007.

[122] Y. Yin, C. K. Erdonmez, A. Cabot, S. Hughes, and A. P. Alivisatos, "Colloidal synthesis of hollow cobalt sulfide nanocrystals," *Adv. Funct. Mater.*, vol. 16, pp. 1389–1399, 2006.

[123] M. Chen, J. Kim, J. P. Liu, H. Fan, and S. Sun, "Synthesis of FePt nanocubes and their oriented self-assembly," *J. Amer. Chem. Soc.*, vol. 128, pp. 7132–7133, 2006.

[124] M. Sastry, A. Swami, S. Mandal, and P. R. Selvakannan, "New approaches to the synthesis of anisotropic, core-shell and hollow metal nanostructures," *J. Mater. Chem.*, vol. 15, pp. 3161–3174, 2005.

[125] M. Chen, J. P. Liu, and S. Sun, "One-step synthesis of FePt nanoparticles with tunable size," *J. Amer. Chem. Soc.*, vol. 126, pp. 8394–8395, 2004.

[126] M. Chen, T. Pica, Y. Jiang, P. Li, K. Yano, J. P. Liu, A. K. Datye, and H. Fan, "Synthesis and self-assembly of fcc phase FePt nanorods," *J. Amer. Chem. Soc.*, vol. 129, pp. 6348–6349, 2007.

[127] V. F. Puntes, D. Zanchet, C. K. Erdonmez, and A. P. Alivisatos, "Synthesis of hcp-Co nanodisks," *J. Amer. Chem. Soc.*, vol. 124, pp. 12874–12880, 2002.

[128] V. Salgueiriño-Maceira, M. A. Correa-Duarte, and M. Farle, "Manipulation of chemically synthesized FePt nanoparticles in water: Core-shell silica/FePt nanocomposites," *Small*, vol. 1, pp. 1073–1076, 2005.

[129] V. Salgueiriño-Maceira, M. A. Correa-Duarte, M. Farle, A. López-Quintela, K. Sieradzki, and R. Diaz, "Bifunctional gold-coated magnetic silica spheres," *Chem. Mater.*, vol. 18, pp. 2701–2706, 2006.

[130] C. Xu and S. Sun, "Monodisperse magnetic nanoparticles for biomedical applications," *Polymer Int.*, vol. 56, pp. 821–826, 2007.

[131] L. Li, M. Fan, R. C. Brown, J. Van Leeuwen, J. Wang, W. Wang, Y. Song, and P. Zhang, "Synthesis, properties, and environmental applications of nanoscale iron-based materials: A review," *Crit. Rev. Environ. Sci. Technol.*, vol. 36, pp. 405–431, 2006.

[132] S. Sun, "Recent advances in chemical synthesis, self-assembly, and applications of FePt nanoparticles," *Adv. Mater.*, vol. 18, pp. 393–403, 2006.

[133] M. Farle, "Ferromagnetic resonance of ultrathin metallic layers," *Rep. Prog. Phys.*, vol. 61, pp. 755–826, 1998.

[134] C. Antoniak, J. Lindner, V. Salgueiriño-Maceira, and M. Farle, "Multifrequency magnetic resonance and blocking behavior of Fe_xPt_{1-x} nanoparticles," *Phys. Stat. Sol. A*, vol. 203, pp. 2968–2973, 2006.

[135] K. Fauth, "How well does total electron yield measure X-ray absorption in nanoparticles?," *Appl. Phys. Lett.*, vol. 85, pp. 3271–3273, 2004.

[136] K. Fauth, E. Goering, and L. Theil Kuhn, "Spatially resolved magnetic response in core shell nanoparticles," *Mod. Phys. Lett. B*, vol. 21, pp. 1197–1200, 2007.

[137] U. Wiedwald, M. Spasova, E. L. Salabas, M. Ulmeanu, M. Farle, Z. Frait, A. Fraile Rodriguez, D. Arvanitis, N. S. Sobal, M. Hilgendorff, and M. Giersig, "Ratio of orbital-to-spin magnetic moment in Co core-shell nanoparticles," *Phys. Rev. B*, vol. 68, pp. 644241–644245, 2003.

[138] U. Wiedwald, K. Fauth, M. Heßler, H. G. Boyen, F. Weigl, M. Hilgendorff, M. Giersig, G. Schütz, P. Ziemann, and M. Farle, "From colloidal Co/CoO core/shell nanoparticles to arrays of metallic nanomagnets: Surface modification and magnetic properties," *ChemPhysChem*, vol. 6, pp. 2522–2526, 2005.

[139] C. Antoniak and M. Farle, "Magnetism at the nanoscale: The case of FePt," *Mod. Phys. Lett. B*, vol. 21, pp. 1111–1131, 2007.

[140] O. Dmitrieva, M. Acet, G. Dumpich, J. Kästner, C. Antoniak, M. Farle, and K. Fauth, "Enhancement of $L1_0$ phase formation in FePt nanoparticles by nitrogenization," *J. Phys. D: Appl. Phys.*, vol. 39, pp. 4741–4745, 2006.

[141] A. Ethirajan, U. Wiedwald, H. G. Boyen, B. Kern, L. Han, A. Klimmer, F. Weigl, G. Kästle, P. Ziemann, K. Fauth, J. Cai, R. J. Behm, A. Romanyuk, P. Oelhafen, P. Walther, J. Biskupek, and U. Kaiser, "A micellar approach to magnetic ultrahigh-density data-storage media: Extending the limits of current colloidal methods," *Adv. Mater.*, vol. 19, pp. 406–410, 2007.

[142] H. G. Boyen, G. Kästle, K. Zürn, T. Herzog, F. Weigl, P. Ziemann, O. Mayer, C. Jerome, M. Möller, J. P. Spatz, M. G. Garnier, and P. Oelhafen, "A micellar route to ordered arrays of magnetic nanoparticles: From size-selected pure cobalt dots to cobalt-cobalt oxide core-shell systems," *Adv. Funct. Mater.*, vol. 13, pp. 359–364, 2003.

[143] M. Cerchez, U. Wiedwald, and M. Farle, "Using hysteresis behaviour to determine the anisotropy and interactions in complex self-assembled Co metallic nanoparticle systems," *J. Magn. Magn. Mater.*, vol. 290–291, pt. 1, pp. 161–164, 2005.

[144] C. Antoniak, J. Lindner, M. Spasova, D. Sudfeld, M. Acet, M. Farle, K. Fauth, U. Wiedwald, H. G. Boyen, P. Ziemann, F. Wilhelm, A. Rogalev, and S. Sun, "Enhanced orbital magnetism in $\mathrm{Fe_{50}Pt_{50}}$ nanoparticles," *Phys. Rev. Lett.*, vol. 97, 2006.

[145] A. Fraile Rodríguez, F. Nolting, J. Bansmann, A. Kleibert, and L. J. Heyderman, "X-ray imaging and spectroscopy of individual cobalt nanoparticles using photoemission electron microscopy," *J. Magn. Magn. Mater.*, vol. 316, pp. 426–428, 2007.

[146] J. R. Jinschek, K. J. Batenburg, H. A. Calderon, R. Kilaas, V. Radmilovic, and C. Kisielowski, "3-D reconstruction of the atomic positions in a simulated gold nanocrystal based on discrete tomography: Prospects of atomic resolution electron tomography," *Ultramicroscopy*, vol. 108, pp. 589–604, 2008.

[147] X. Xu, S. P. Beckman, P. Specht, E. R. Weber, D. C. Chrzan, R. P. Erni, I. Arslan, N. Browning, A. Bleloch, and C. Kisielowski, "Distortion and segregation in a dislocation core region at atomic resolution," *Phys. Rev. Lett.*, vol. 95, pp. 1–4, 2005.

[148] R. Wang, O. Dmitrieva, M. Farle, G. Dumpich, H. Ye, H. Poppa, R. Kilaas, and C. Kisielowski, "Layer resolved relaxation and Pt enrichment at the surface of magnetic FePt icosahedral nanoparticles," *Phys. Rev. Lett.*, vol. 100, pp. 017205-1–017205-4, 2008.

[149] P. Schattschneider, S. Rubino, C. Hébert, J. Rusz, J. Kunes, P. Novák, E. Carlino, M. Fabrizioli, G. Panaccione, and G. Rossi, "Detection of magnetic circular dichroism using a transmission electron microscope," *Nature*, vol. 441, pp. 486–488, 2006.

[150] C. Hébert, S. Rubino, P. Schattschneider, J. Rusz, P. Novak, C. Hurm, and J. Zweck, "Observation of magnetic circular dichroism in the electron microscope," *Microscop. Microanal.*, vol. 12, pp. 960–961, 2006.

[151] R. Meckenstock, I. Barsukov, O. Posth, J. Lindner, A. Butko, and D. Spoddig, "Locally resolved ferromagnetic resonance in Co stripes," *Appl. Phys. Lett.*, vol. 91, p. 142507, 2007.

[152] G. Boero, S. Rusponi, P. Bencok, R. S. Popovic, H. Brune, and P. Gambardella, "X-ray ferromagnetic resonance spectroscopy," *Appl. Phys. Lett.*, vol. 87, pp. 1–3, 2005.

[153] J. Goulon, A. Rogalev, F. Wilhelm, N. Jaouen, C. Goulon-Ginet, and C. Brouder, "X-ray detected ferromagnetic resonance in thin films: Uniform precession in a steady-state foldover regime," *Eur. Phys. J. B*, vol. 53, pp. 169–184, 2006.

[154] J. Goulon, A. Rogalev, F. Wilhelm, N. Jaouen, C. Goulon-Ginet, G. Goujon, J. Ben Youssef, and M. V. Indenbom, "Element selective X-ray detected magnetic resonance," *J. Electron Spectr. Rel. Phen.*, vol. 156–158, pp. 38–44, 2007.

[155] J. Goulon, A. Rogalev, F. Wilhelm, N. Jaouen, C. Goulon-Ginet, G. Goujon, J. B. Youssef, and M. V. Indenbom, "Element selective X-ray detected magnetic resonance," in *Proc. AIP Conf.*, 2007, vol. 879, pp. 1663–1666.

[156] J. Goulon, A. Rogalev, F. Wilhelm, C. Goulon-Ginet, and G. Goujon, "Element-selective X-ray detected magnetic resonance: A novel application of synchrotron radiation," *J. Syn. Rad.*, vol. 14, pp. 257–271, 2007.

[157] G. van der Laan, "Sum rules and beyond," *J. Electron Spectr. Rel. Phen.*, vol. 103, pp. 859–868, 1999.

[158] J. T. Lau, U. Langenbuch, A. Achleitner, H.-U. Ehrke, M. Reif, and W. Wurth, "Ultrahigh vacuum cluster deposition source for spectroscopy with synchrotron radiation," *Rev. Sci. Instrum.*, vol. 76, pp. 063902-1–063902-8, 2005.

[159] J. T. Lau, W. Wurth, H.-U. Ehrke, and A. Achleitner, "Soft landing of size-selected clusters in rare gas matrices," *Low Temp. Phys.*, vol. 29, pp. 223–227, 2003.

[160] K. Bromann, C. Félix, H. Brune, W. Harbich, R. Monot, J. Buttet, and K. Kern, "Controlled deposition of size-selected silver nanoclusters," *Science*, vol. 274, pp. 956–958, 1996.

[161] J. T. Lau, A. Föhlisch, R. Nietubyc, M. Reif, and W. Wurth, "X-ray magnetic dichroism of small size selected Fe clusters," *Phys. Rev. Lett.*, vol. 89, pp. 057201-1–057201-4, 2002.

[162] J. T. Lau, A. Föhlisch, M. Martins, R. Nietubyc, M. Reif, and W. Wurth, "Spin and orbital magnetic moments of deposited small iron clusters studied by X-ray magnetic circular dichroism spectroscopy," *New J. Phys.*, vol. 4, pp. 98.1–98.12, 2002.

[163] P. Mavropoulos, S. Lounis, R. Zeller, and S. Blügel, "Fe clusters on Ni and Cu: Size and shape dependence of the spin moment," *Appl. Phys. A*, vol. 82, pp. 103–107, 2006.

[164] A. Shick, A. Lichtenstein, M. Martins, and W. Wurth, unpublished.

[165] S. Lounis, M. Reif, P. Mavropoulos, L. Glaser, P. H. Dederichs, M. Martins, S. Blügel, and W. Wurth, "Non-collinear magnetism of Cr nanostructures on $\mathrm{Fe}_{3ML}/\mathrm{Cu}(001)$: First-principles and experimental investigations," *Europhys. Lett.*, vol. 81, p. 47004-1, 2008, 47004-1.

[166] P. Gambardella, S. Rusponi, M. Veronese, S. S. Dhesi, C. Grazioli, A. Dallmeyer, I. Cabria, R. Zeller, P. H. Dederichs, K. Kern, C. Carbone, and H. Brune, "Giant magnetic anisotropy of single cobalt atoms and nanoparticles," *Science*, vol. 300, pp. 1130–1133, 2003.

[167] M. Martins, S. Fiedler, L. Glaser, P. Imperia, W. Wurth, S. Bornemann, J. Minar, and H. Ebert, unpublished.

[168] M. Martins, S. Fiedler, L. Glaser, P. Imperia, and W. Wurth, unpublished.

[169] C. Kao, J. Hastings, E. Johnson, D. Siddons, G. Smith, and G. Prinz, "Magnetic-resonance exchange scattering at the iron L_{II} and L_{III} edges," *Phys. Rev. Lett.*, vol. 65, pp. 373–376, 1990.

[170] L. Seve, N. Jaouen, J. M. Tonnerre, D. Raoux, F. Bartolome, M. Arend, W. Felsch, A. Rogalev, J. Goulon, and C. Gautier *et al.*, "Profile of the induced 5d magnetic moments in Ce/Fe and La/Fe multilayers probed by X-ray magnetic-resonant scattering," *Phys. Rev. B*, vol. 60, pp. 9662–9674, 1999.

[171] T. P. A. Hase, I. Pape, B. K. Tanner, H. Dürr, E. Dudzik, G. van der Laan, C. H. Marrows, and B. J. Hickey, "Soft X-ray magnetic scattering evidence for biquadratic coupling in Co/Cu multilayers," *Phys. Rev. B*, vol. 61, pp. 15331–15337, 1994.

[172] J. Geissler, E. Goering, M. Justen, F. Weigand, G. Schütz, J. Langer, D. Schmitz, H. Maletta, and R. Mattheis, "Pt magnetization profile in a Pt/Co bilayer studied by resonant magnetic X-ray reflectometry," *Phys. Rev. B*, vol. 65, pp. 020405.1–020405.4, 2002.

[173] N. Jaouen, J. Tonnerre, D. Raoux, E. Bontempi, L. Ortega, M. Müenzenberg, W. Felsch, A. Rogalev, H. Dürr, and E. Dudzik *et al.*, "Ce 5d magnetic profile in Fe/Ce multilayers for the α and γ-like Ce phases by X-ray resonant magnetic scattering," *Phys. Rev. B*, vol. 66, pp. 134420.1–134420.14, 2002.

[174] G. van der Laan, K. Chesnel, M. Belakhovsky, A. Marty, F. Livet, S. P. Collins, E. Dudzik, A. Haznar, and J. P. Attan, "Magnetic anisotropy of aligned magnetic stripe domains in FePd studied by soft X-ray resonant magnetic scattering, magnetic force microscopy and micromagnetic modeling," *Superlatt. Microstruct.*, vol. 34, pp. 107–126, 2003.

[175] G. van der Laan, "Studying spintronics materials with soft X-ray resonant scattering," *Current Opinion Solid State Mater. Sci.*, vol. 10, pp. 120–127, 2006.

[176] G. Srajer, L. H. Lewis, S. D. Bader, A. J. Epstein, C. S. Fadley, E. E. Fullerton, A. Hoffmann, J. B. Kortright, K. M. Krishnan, S. A. Majetich, T. S. Rahman, C. A. Ross, M. B. Salamon, I. K. Schuller, T. C. Schulthess, and J. Z. Sun, "Advances in nanomagnetism via X-ray techniques," *J. Magn. Magn. Mater.*, vol. 307, pp. 1–31, 2006.

[177] A. Bergmann, J. Grabis, A. Nefedov, K. Westerholt, and H. Zabel, "X-ray resonant magnetic scattering study of $[\mathrm{Co_2MnGe/Au}]_n$ and $[\mathrm{Co_2MnGe/V}]_n$ multilayers," *J. Phys. D: Appl. Phys.*, vol. 39, pp. 842–850, 2006.

[178] J. M. Tonnerre, L. Seve, D. Raoux, G. Soullie, B. Rodmacq, and P. Wolfers, "Soft X-ray resonant magnetic scattering from a magnetically coupled Ag/Ni multilayer," *Phys. Rev. Lett.*, vol. 75, pp. 740–743, 1995.

[179] J. Zak, E. R. Moog, C. Liu, and S. D. Bader, "Universal approach to magneto-optics," *J. Magn. Magn. Mater.*, vol. 89, pp. 107–123, 1990.

[180] J. Zak, E. R. Moog, C. Liu, and S. D. Bader, "Magneto-optics of multilayers with arbitrary magnetization directions," *Phys. Rev. B*, vol. 43, pp. 6423–6429, 1991.

[181] J. Zak, E. R. Moog, C. Liu, and S. D. Bader, "Erratum: Magneto-optics of multilayers with arbitrary magnetization directions," *Phys. Rev. B*, vol. 46, p. 5883(E), 1992.

[182] D. R. Lee, S. K. Sinha, D. Haskel, Y. Choi, J. C. Lang, S. A. Stepanov, and G. Srajer, "X-ray resonant magnetic scattering from structurally and magnetically rough interfaces in multilayered systems. I. Specular reflectivity," *Phys. Rev. B*, vol. 68, pp. 224409.1–224409.19, 2003.

[183] D. R. Lee, S. K. Sinha, C. S. Nelson, J. C. Lang, C. T. Venkataraman, G. Srajer, and R. M. Osgood, III, "X-ray resonant magnetic scattering from structurally and magnetically rough interfaces in multilayered systems. II. Diffuse scattering," *Phys. Rev. B*, vol. 68, pp. 224410. 1–224410.14, 2003.

[184] J. Grabis, A. Bergmann, A. Nefedov, K. Westerholt, and H. Zabel, "Element-specific X-ray circular magnetic dichroism of Co_2MnGe Heusler thin films," *Phys. Rev. B*, vol. 72, pp. 024437.1–024437.4, 2005.

[185] M. Kallmayer, A. Conca, M. Jourdan, H. Schneider, G. Jakob, B. Balke, A. Gloskovskii, and H. Elmers, "Correlation of local disorder and electronic properties in the Heusler alloy $Co_2Cr_{0.6}Fe_{0.4}Al$," *J. Phys. D: Appl. Phys.*, vol. 40, pp. 1539–1543, 2007.

[186] S. Picozzi, A. Continenza, and A. J. Freeman, "Role of structural defects on the half-metallic character of Co_2MnGe and Co_2MnSi Heusler alloys," *Phys. Rev. B*, vol. 69, pp. 094423.1–094423.7, 2004.

[187] J. Grabis, A. Nefedov, and H. Zabel, "A diffractometer for soft X-ray resonant magnetic scattering," *Rev. Sci. Instr.*, vol. 74, pp. 4048–4051, 2003.

[188] J. B. Kortright and S.-K. Kim, "Resonant magneto-optical properties of Fe near its 2p levels: Measurement and applications," *Phys. Rev. B*, vol. 62, pp. 12216–12228, 2000.

[189] M. Vadalà, A. Nefedov, M. Wolff, K. N. Zhernenkov, K. Westerholt, and H. Zabel, "Structure and magnetism of Co_2MnGe-Heusler multilayers with V, Au and AlOx spacer layers," *J. Phys. D: Appl. Phys.*, vol. 40, pp. 1289–1292, 2007.

[190] A. Schreyer, K. Brhl, J. F. Ankner, C. F. Majkrzak, T. Zeidler, P. Bdeker, N. Metoki, and H. Zabel, "Oscillatory exchange coupling in Co/Cu(111) superlattices," *Phys. Rev. B*, vol. 47, pp. 15334–15337, 1993.

[191] P. Mangin, C. Dufour, and B. Rodmacq, "Neutron investigations of magnetic multilayers," *Phys. B*, vol. 192, pp. 122–136, 1993.

[192] C. Spezzani, P. Torelli, M. Sacchi, R. Delaunay, C. F. Hague, F. Salmassi, and E. M. Gullikson, "Hysteresis curves of ferromagnetic and antiferromagnetic order in metallic multilayers by resonant X-ray scattering," *Phys. Rev. B*, vol. 66, pp. 052408.1–052408.4, 2002.

[193] M. Hecker, S. Valencia, P. M. Oppeneer, H.-C. Mertins, and C. M. Schneider, "Polarized soft-X-ray reflection spectroscopy of giant magnetoresistive Co/Cu multilayers," *Phys. Rev. B*, vol. 72, pp. 054437. 1–054437.6, 2005.

[194] A. Nefedov, J. Grabis, A. Bergmann, F. Radu, and H. Zabel, "X-ray resonant magnetic scattering of Fe/Cr superlattices," *Superlatt. Microstruct.*, vol. 37, pp. 99–106, 2005.

[195] A. Nefedov, J. Grabis, and H. Zabel, "X-ray resonant magnetic scattering on noncollinearly coupled Fe/Cr superlattices," *Phys. B*, vol. 357, pp. 22–26, 2005.

[196] A. Nefedov, N. Akdogan, H. Zabel, R. I. Khaibullin, and L. R. Tagirov, "Spin polarization of oxygen atoms in ferromagnetic Co-doped rutile TiO_2," *Appl. Phys. Lett.*, vol. 89, pp. 182509.1–182509.3, 2006.

[197] F. Radu and H. Zabel, "Fundamental aspects of exchange bias," in *Springer Tracts in Modern Physics*, H. Zabel and S. D. Bader, Eds. Berlin: Springer, 2007, vol. 227, Magnetic Heterostructures, Advances and Perspectives in Spinstructures and Spintransport.

[198] S. Roy, M. R. Fitzsimmons, S. Park, M. Dorn, O. Petracic, I. V. Roshchin, Z.-P. Li, X. Batlle, R. Morales, A. Misra, X. Zhang, K. Chesnel, J. B. Kortright, S. K. Sinha, and I. K. Schuller, "Depth profile of uncompensated spins in an exchange bias system," *Phys. Rev. Lett.*, vol. 95, pp. 047201.1–047201.4, 2005.

[199] F. Radu, A. Nefedov, J. Grabis, G. Nowak, A. Bergmann, and H. Zabel, "Soft X-ray resonant magnetic scattering studies on Fe/CoO exchange bias system," *J. Magn. Magn. Mater.*, vol. 300, pp. 206–210, 2006.

[200] J. M. Tonnerre, M. De Santis, S. Grenier, H. C. N. Tolentino, V. Langlais, E. Bontempi, M. Garcia-Fernandez, and U. Staub, "Depth magnetization profile of a perpendicular exchange coupled system by soft-X-ray resonant magnetic reflectivity," *Phys. Rev. Lett.*, vol. 100, pp. 157202.1–157202.4, 2008.

[201] T. Dietl, H. Ohno, F. Matsukura, J. Cibert, and D. Ferrand, "Zener model description of ferromagnetism in Zinc-Blende magnetic semiconductors," *Science*, vol. 287, pp. 1019–1022, 2000.

[202] O. Hellwig, D. T. Margulies, B. Lengsfield, E. E. Fullerton, and J. B. Kortright, "Role of B on grain sizes and magnetic correlation lengths in recording media as determined by soft X-ray scattering," *Appl. Phys. Lett.*, vol. 80, pp. 1234–1236, 2002.

[203] J. B. Kortright, O. Hellwig, D. T. Margulies, and E. E. Fullerton, "Resolving magnetic and chemical correlations in CoPtCr films using soft X-ray resonant scattering," *J. Magn. Magn. Mater.*, vol. 240, pp. 325–330, 2002.

[204] J. B. Kortright, J. S. Jiang, S. D. Bader, O. Hellwig, D. T. Marguiles, and E. E. Fullerton, "Magnetism in heterogeneous thin film systems: Resonant X-ray scattering studies," *Nucl. Instrum. Meth. Phys. Res. B*, vol. 199, pp. 301–307, 2003.

[205] J. B. Kortright, S.-K. Kim, G. P. Denbeaux, G. Zeltzer, K. Takano, and E. E. Fullerton, "Soft X-ray small-angle scattering as a sensitive probe of magnetic and charge heterogeneity," *Phys. Rev. B*, vol. 64, pp. 092401.1–092401.4, 2001.

[206] J. B. Kortright, O. Hellwig, K. Chesnel, S. Sun, and E. E. Fullerton, "Interparticle magnetic correlations in dense Co nanoparticle assemblies," *Phys. Rev. B*, vol. 71, pp. 012402.1–012402.4, 2005.

[207] O. Hellwig, G. P. Denbeaux, J. B. Kortright, and E. E. Fullerton, "X-ray studies of aligned magnetic stripe domains in perpendicular multilayers," *J. Magn. Magn. Mater.*, vol. 336, pp. 136–144, 2003.

[208] O. Hellwig, S. Eisebitt, J. Grabis, A. Nefedov, and H. Zabel, Scattering from magnetic nanostructures in transmission geometry Ruhr Univ., Bochum, Germany, 2004, p. 42.

[209] O. Hellwig, A. Berger, J. B. Kortright, and E. E. Fullerton, "Domain structure and magnetization reversal of antiferromagnetically coupled perpendicular anisotropy films," *J. Magn. Magn. Mater.*, vol. 319, pp. 13–55, 2007.

[210] L.-A. Michez, C. H. Marrows, P. Steadman, B. J. Hickey, D. A. Arena, J. Dvorak, H.-L. Zhang, D. G. Bucknall, and S. Langridge, "Resonant X-ray scattering from a magnetic multilayer reflection grating," *Appl. Phys. Lett.*, vol. 86, pp. 112502.1–112502.3, 2005.

[211] K. Chesnel, M. Belakhovsky, S. Landis, J. C. Toussaint, S. P. Collins, G. van der Laan, E. Dudzik, and S. S. Dhesi, "X-ray resonant magnetic scattering study of the magnetic coupling in Co/Pt nanolines and its evolution under magnetic field," *Phys. Rev. B.*, vol. 66, pp. 024435. 1–024435.9, 2002.

[212] A. Remhof., C. Bircan, A. Westphalen, J. Grabis, A. Nefedov, and H. Zabel, "Shining light on magnetic microstructures," *Superlatt. Microstruct.*, vol. 37, pp. 353–363, 2005.

[213] M. van Kampen, I. L. Soroka, R. Brucas, B. Hjörvarsson, R. Wieser, K. D. Usadel, M. Hanson, O. Kazakova, J. Grabis, H. Zabel, C. Jozsa, and B. Koopmans, "On the realization of artificial XY spin chains," *J. Phys.: Condens. Mater.*, vol. 17, pp. L27–L33, 2005.

[214] J. W. Freeland, V. Chakarian, K. Bussmann, Y. U. Idzerda, H. Wende, and C.-C. Kao, "Exploring magnetic roughness in CoFe thin films," *J. Appl. Phys.*, vol. 83, pp. 6290–6292, 1998.

[215] J. W. Freeland, K. Bussmann, Y. U. Idzerda, and C.-C. Kao, "Understanding correlations between chemical and magnetic interfacial roughness," *Phys. Rev. B*, vol. 60, pp. R9923–R9926, 1999.

[216] R. M. Osgood, III, S. K. Sinha, J. W. Freeland, Y. U. Idzerda, and S. D. Bader, "X-ray scattering from magnetic, rough surfaces," *J. Appl. Phys.*, vol. 85, pp. 4619–4621, 1999.

[217] C. S. Nelson, G. Srajer, J. C. Lang, C. T. Venkataraman, S. K. Sinha, H. Hashizume, N. Ishimatsu, and N. Hosoito, "Charge-magnetic roughness correlations in an Fe/Gd multilayer," *Phys. Rev. B*, vol. 60, pp. 12234–12238, 1999.

[218] E. D. Palik, "A brief survey of magnetooptics," *Appl. Opt.*, vol. 6, pp. 597–597, 1967.

[219] J. B. Kortright, M. Rice, S.-K. Kim, C. C. Walton, and T. Warwick, "Optics for element-resolved soft X-ray magneto-optical studies," *J. Magn. Magn. Mater.*, vol. 191, pp. 79–89, 1999.

[220] H.-C. Mertins, P. M. Oppeneer, J. Kunes, A. Gaupp, D. Abramsohn, and F. Schäfers, "Observation of the X-ray magneto-optical Voigt effect," *Phys. Rev. Lett.*, vol. 87, pp. 047401.1–047401.4, 2001.

[221] H.-C. Mertins, F. Schäfers, and X. Le Cann, "Faraday rotation at the $2p$ edges of Fe, Co, and Ni," *Phys. Rev. B*, vol. 61, pp. R874–R877, 2000, A. Gaupp, and W. Gudat.

[222] D. S. Kliger, J. W. Lewis, and C. E. Randall, *Polarized Light in Optics and Spectroscopy*. New York: Academic Press, 1990.

[223] F. Schäfers, H.-C. Mertins, A. Gaupp, W. Gudat, M. Mertin, I. Packe, F. Schmolla, S. Di Fonzo, G. Soullié, W. Jark, R. Walker, X. Le Cann, M. Eriksson, and R. Nyholm, "Soft-X-ray polarimeter with multilayer optics: Complete analysis of the polarization state of light," *Appl. Opt.*, vol. 38, pp. 4074–4088, 1999.

[224] K. Starke, F. Heigl, A. Vollmer, M. Weiss, G. Reichardt, and G. Kaindl, "X-Ray magneto-optics in lanthanides," *Phys. Rev. Lett.*, vol. 86, pp. 3415–3418, 2001.

[225] D. P. Siddons, M. Hart, Y. Amemiya, and J. B. Hastings, "X-ray optical activity and the Faraday effect in cobalt and its compounds," *Phys. Rev. Lett.*, vol. 64, pp. 1967–1970, 1990.

[226] Q. Shen, S. Shastri, and K. D. Finkelstein, "Stokes polarimetry for X-rays using multiple-beam diffraction," *Rev. Sci. Instrum.*, vol. 66, pp. 1610–1613, 1995.

[227] S. Valencia, A. Gaupp, W. Gudat, H.-C. Mertins, P. M. Oppeneer, D. Abramsohn, and C. M. Schneider, "Faraday rotation spectrum at shallow core levels: 3p edges of Fe, Co, and Ni," *New J. Phys.*, vol. 8, pp. 254.1–254.11, 2006.

[228] J. Kunes, P. M. Oppeneer, H.-C. Mertins, F. Schäfers, and A. Gaupp, "X-ray Faraday effect at the $L_{2,3}$ edges of Fe, Co, and Ni: Theory and experiment," *Phys. Rev. B*, vol. 64, pp. 174417.1–174417.10, 2001, W. Gudat, and P. Novák.

[229] H.-C. Mertins, S. Valencia, D. Abramsohn, A. Gaupp, W. Gudat, and P. M. Oppeneer, "X-ray Kerr rotation and ellipticity spectra at the 2p edges of Fe, Co, and Ni," *Phys. Rev. B*, vol. 69, pp. 064407.1–064407.6, 2004.

[230] P. M. Oppeneer, "Magneto-optical Kerr spectra," in *Handbook of Magnetic Materials*, K. H. J. Buschow, Ed. Amsterdam, The Netherlands: Elsevier, 2001, vol. 13, pp. 229–422.

[231] J. Kunes and P. M. Oppeneer, "Anisotropic X-ray magnetic linear dichroism at the $L_{2,3}$ edges of cubic Fe, Co, and Ni: Ab initio calculations and model theory," *Phys. Rev. B*, vol. 67, pp. 024431.1–024431.9, 2003.

[232] H.-C. Mertins, P. M. Oppeneer, S. Valencia, W. Gudat, F. Senf, and P. R. Bressler, "X-ray natural birefringence in reflection from graphite," *Phys. Rev. B*, vol. 70, pp. 235106.1–235106.8, 2004.

[233] H.-C. Mertins, D. Abramsohn, A. Gaupp, F. Schäfers, W. Gudat, O. Zaharko, H. Grimmer, and P. M. Oppeneer, "Resonant magnetic reflection coefficients at the Fe 2p edge obtained with linearly and circularly polarized soft x rays," *Phys. Rev. B*, vol. 66, pp. 184404.1–184404.8, 2002.

[234] P. M. Oppeneer, H.-C. Mertins, D. Abramsohn, A. Gaupp, W. Gudat, J. Kunes, and C. M. Schneider, "Buried antiferromagnetic films investigated by X-ray magneto-optical reflection spectroscopy," *Phys. Rev. B*, vol. 67, pp. 052401.1–052401.4, 2003.

[235] H.-C. Mertins, S. Valencia, W. Gudat, P. M. Oppeneer, O. Zaharko, and H. Grimmer, "Direct observation of local ferromagnetism on carbon in C/Fe multilayers," *Europhys. Lett.*, vol. 66, pp. 743–748, 2004.

[236] S. N. Piramanayagama, "Perpendicular recording media for hard disk drives," *J. Appl. Phys.*, vol. 102, pp. 011301.1–011301.22, 2007.

[237] A. Moser1, K. Takano, D. T. Margulies, M. Albrecht, Y. Sonobe, Y. Ikeda, S. Sun, and E. E. Fullerton, "Magnetic recording: Advancing into the future," *J. Phys. D: Appl. Phys.*, vol. 35, pp. R157–R167, 2002.

[238] B. D. Terris and T. Thomson, "Nanofabricated and self-assembled magnetic structures as data storage media," *J. Phys. D: Appl. Phys.*, vol. 38, pp. R199–R222, 2005.

[239] T. W. McDaniel, "Ultimate limits to thermally assisted magnetic recording," *J. Phys.: Condens. Mater.*, vol. 17, pp. R315–R332, 2005.

[240] R. E. Rottmayer, S. Batra, D. Buechel, W. A. Challener, J. Hohlfeld, Y. Kubota, L. Li, B. Lu, C. Mihalcea, K. Mountfield, K. Pelhos, C. Peng, T. Rausch, M. A. Seigler, D. Weller, and X. Yang, "Heat-assisted magnetic recording," *IEEE Trans. Magn.*, vol. 42, pp. 2417–2421, 2006.

[241] J. Åkerman, "Towards a universal memory," *Science*, vol. 308, pp. 508–510, 2005.

[242] L. Thomas, M. Hayashi, X. Jiang, R. Moriya, C. Rettner, and S. Parkin, "Resonant amplification of magnetic domain-wall motion by a train of current pulses," *Science*, vol. 315, pp. 1553–1555, 2007.

[243] *The Physics of Ultrahigh-Density Magnetic Recording*, Plummer and W. van Ek, Eds. New York: Springer, 2001.

[244] W. Kuch, R. Frömter, J. Gilles, D. Hartmann, C. Ziethen, C. M. Schneider, G. Schönhense, W. Swiech, and J. Kirschner, "Element-selective magnetic imaging in exchange-coupled systems by magnetic photoemission microscopy," *Surf. Rev. Lett.*, vol. 5, pp. 1241–1248, 1998.

[245] W. Kuch, "Layer-resolved microscopy of magnetic domains in multilayered systems," *Appl. Phys. A*, vol. 76, pp. 665–671, 2003.

[246] L. I. Chelaru, "Microscopic Studies of Interlayer Magnetic Coupling Across Nonmagnetic and Antiferromagnetic Spacer Layers" Ph.D. dissertation, Martin-Luther-Universität Halle-Wittenberg, Halle, 2003 [Online]. Available: http://www.sundoc.bibliothek.uni-halle.de/diss-online/03/04H051

[247] W. Kuch, L. I. Chelaru, F. Offi, M. Kotsugi, and J. Kirschner, "Magnetic dichroisms in absorption and photoemission for the magnetic characterization in X-ray photoelectron emission microscopy," *J. Vac. Sci. Technol. B*, vol. 20, pp. 2543–2549, 2002.

[248] M. Kotsugi, W. Kuch, F. Offi, L. I. Chelaru, and J. Kirschner, "Microspectroscopic two-dimensional Fermi surface mapping using a photoelectron emission microscope," *Rev. Sci. Instrum.*, vol. 74, pp. 2754–2758, 2003.

[249] W. Kuch, L. I. Chelaru, K. Fukumoto, F. Porrati, F. Offi, M. Kotsugi, and J. Kirschner, "Layer-resolved imaging of magnetic interlayer coupling by domain-wall stray fields," *Phys. Rev. B*, vol. 67, pp. 214403–214419, 2003.

[250] J. A. C. Bland and B. Heinrich, *Ultrathin Magnetic Structures*. New York: Springer, 1994, vol. 1.

[251] P. Bruno and C. Chappert, "Oscillatory coupling between ferromagnetic layers separated by a nonmagnetic metal spacer," *Phys. Rev. Lett.*, vol. 67, pp. 1602–1605, 1991.

[252] P. Bruno, "Theory of interlayer magnetic coupling," *Phys. Rev. B*, vol. 52, pp. 411–415, 1995.

[253] J. Nogués and I. K. Schuller, "Exchange bias," *J. Magn. Magn. Mater.*, vol. 192, pp. 203–232, 1999.

[254] R. L. Stamps, "Mechanisms for exchange bias," *J. Phys. D: Appl. Phys.*, vol. 33, pp. R247–R268, 2000.

[255] W. H. Meiklejohn and C. P. Bean, "New magnetic anisotropy," *Phys. Rev.*, vol. 102, pp. 1413–1414, 1956.

[256] B. Dieny, V. S. Speriosu, S. S. P. Parkin, B. A. Gurney, D. R. Wilhoit, and D. Mauri, "Giant magnetoresistive in soft ferromagnetic multilayers," *Phys. Rev. B*, vol. 43, pp. 1297–1300, 1991.

[257] J. C. S. Kools, "Exchange-biased spin-valves for magnetic storage," *IEEE Trans. Magn.*, vol. 32, pp. 3165–3184, 1996.

[258] W. Kuch, J. Gilles, F. Offi, S. S. Kang, S. Imada, S. Suga, and J. Kirschner, "Imaging microspectroscopy of Ni/Fe/Co/Cu(001) using a photoemission microscope," *J. Electron Spectrosc. Relat. Phenom.*, vol. 109, pp. 249–265, 2000.

[259] W. Kuch, L. I. Chelaru, F. Offi, J. Wang, M. Kotsugi, and J. Kirschner, "Tuning the magnetic coupling across ultrathin antiferromagnetic films by controlling atomic-scale roughness," *Nature Mater.*, vol. 5, pp. 128–133, 2006.

[260] J. C. Slonczewski, "Fluctuation mechanism for biquadratic exchange coupling in magnetic multilayers," *Phys. Rev. Lett.*, vol. 67, pp. 3172–3175, 1991.

[261] F. Nolting, A. Scholl, J. Stöhr, J. Fompeyrine, H. Siegwart, J.-P. Locquet, S. Anders, J. Lüning, E. E. Fullerton, M. F. Toney, M. R. Scheinfein, and H. A. Padmore, "Direct observation of the alignment of ferromagnetic spins by antiferromagnetic spins," *Nature*, vol. 405, pp. 767–769, 2000.

[262] A. Recnik, D. L. Carroll, K. A. Shaw, D. M. Lind, and M. Ruhle, "Structural characterization of Fe_3O_4-NiO superlattices using high-resolution transmission electron microscopy," *J. Mater. Res.*, vol. 12, pp. 2143–2151, 1997.

[263] H. Q. Wang, W. Gao, E. I. Altman, and V. E. Henrich, "Studies of the electronic structure at the Fe_3O_4/NiO interface," *J. Vac. Sci. Technol. A*, vol. 22, pp. 1675–1681, 2004.

[264] T. J. Regan, H. Ohldag, C. Stamm, F. Nolting, J. Luning, J. Stohr, and R. L. White, "Chemical effects at metal/oxide interfaces studied by X-ray-absorption spectroscopy," *Phys. Rev. B*, vol. 64, pp. 214422–214433, 2001.

[265] C. Tusche, H. L. Meyerheim, F. U. Hillebrecht, and J. Kirschner, "Evidence for a mixed CoNiO layer at the Co/NiO(001) interface from surface X-ray diffraction," *Phys. Rev. B*, vol. 73, pp. 125401–125407, 2006.

[266] M. Finazzi, M. Portalupi, A. Brambilla, L. Duo, G. Ghiringhelli, F. Parmigiani, M. Zacchigna, M. Zangrando, and F. Ciccacci, "Magnetic anisotropy of NiO epitaxial thin films on Fe(001)," *Phys. Rev. B*, vol. 69, pp. 014410–014414, 2004.

[267] I. P. Krug, F. U. Hillebrecht, H. Gomonaj, M. W. Haverkort, A. Tanaka, L. H. Tjeng, and C. M. Schneider, "Magnetic coupling in highly ordered $NiO/Fe_3O_4(110)$: Ultrasharp magnetic interfaces vs. long-range magnetoelastic interactions," *Europhys. Lett.*, vol. 81, pp. 17005–17010, 2008.

[268] H. Ohldag, T. J. Regan, J. Stöhr, A. Scholl, F. Nolting, J. Lüning, C. Stamm, S. Anders, and R. L. White, "Spectroscopic identification and direct imaging of interfacial magnetic spins," *Phys. Rev. Lett.*, vol. 87, no. 24, pp. 247201–247204, 2001.

[269] N. C. Koon, "Calculations of exchange bias in thin films with ferromagnetic/antiferromagnetic interfaces," *Phys. Rev. Lett.*, vol. 78, no. 25, pp. 4865–4848, 1997.

[270] I. P. Krug, F. U. Hillebrecht, M. W. Haverkort, A. Tanaka, L. H. Tjeng, H. Gomonaj, A. Fraile-Rodríguez, F. Nolting, S. Cramm, and C. M. Schneider, "Impact of the interface orientation on the magnetic coupling in highly ordered systems—A case study of the low-indexed Fe_3O_4/NiO interfaces," *Phys. Rev. B*, submitted for publication.

[271] E. Arenholz, G. van der Laan, R. V. Chopdekar, and Y. Suzuki, "Angle-dependent Ni^{2+} X-ray manetic linear dichroism: Interfacial coupling revisited," *Phys. Rev. Lett.*, vol. 98, pp. 197201-1–197201-4, 2007.

[272] G. van der Laan, C. M. B. Henderson, R. A. D. Pattrick, S. S. Dhesi, P. F. Schofield, E. Dudzik, and D. J. Vaughan, "Orbital polarization of $NiFe_2O_4$ measured by Ni-2p X-ray magnetic circular dichroism," *Phys. Rev. B*, vol. 59, pp. 4314–4321, 1999.

[273] H. Q. Wang, W. Gao, E. I. Altman, and V. E. Henrich, "Studies of the electronic structure at the Fe_3O_4–NiO interface," *J. Vac. Sci. Technol. A*, vol. 22, pp. 1675–1681, 2004.

[274] D. Alders, L. H. Tjeng, F. C. Voogt, T. Hibma, G. A. Sawatzky, C. T. Chen, J. Vogel, M. Sacchi, and S. Iacobucci, "Temperature and thickness dependence of magnetic moments in NiO epitaxial films," *Phys. Rev. B*, vol. 57, pp. 11623–11631, 1998.

[275] S. Eisebitt, J. Lüning, W. F. Schlotter, M. Lörgen, O. Hellwig, W. Eberhardt, and J. Stöhr, "Lensless imaging of magnetic nanostructures by X-ray spectro-holography," *Nature*, vol. 432, pp. 885–888, 2004.

[276] P. Fischer, D.-H. Kim, W. Chao, J. A. Liddle, E. H. Anderson, and D. T. Attwood, "Imaging nanomagnetism with X-ray microscopy," *Mater. Today*, vol. 9, pp. 26–33, 2006.

[277] T. Hauet, C. M. Günther, B. Pfau, M. E. Schabes, J.-U. Thiele, R. L. Rick, P. Fischer, S. Eisebitt, and O. Hellwig, "Direct observation of field and temperature induced domain replication in dipolar coupled perpendicular anisotropy films," *Phys. Rev. B*, vol. 77, pp. 184421–184425, 2008.

[278] H. N. Chapman, A. Barty, M. J. Bogan, S. Boutet, M. Frank, S. P. Hau-Riege, S. Marchesini, B. W. Woods, S. Bajt, W. H. Benner, R. A. London, E. Pönjes, M. Kuhlmann, R. Treusch, S. Düsterer, T. Tschentscher, J. R. Schneider, E. Spiller, T. Müller, C. Bostedt, M. Hoener, D. A. Shapiro, K. O. Hodgson, D. van der Spoel, F. Burmeister, M. Bergh, C. Caleman, G. Huldt, M. M. Seibert, F. R. N. C. Maia, R. W. Lee, A. Szöke, N. Timneanu, and J. Hajdu, "Femtosecond diffractive imaging with a soft-X-ray free-electron laser," *Nature Phys.*, vol. 2, pp. 839–843, 2006.

[279] W. F. Schlotter, R. Rick, K. Chen, A. Scherz, J. Stöhr, J. Lüning, S. Eisebitt, C. Günther, and W. Eberhardt, "Multiple reference Fourier transform holography with soft x rays," *Appl. Phys. Lett.*, vol. 89, pp. 163112.1–163112.3, 2006.

[280] W. F. Schlotter, J. Lüning, R. Rick, K. Chen, A. Scherz, S. Eisebitt, C. M. Günther, W. Eberhardt, O. Hellwig, and J. Stöhr, "Extended field of view soft X-ray fourier transform holography: Towards imaging ultrafast evolution in a single shot," *Opt. Lett.*, vol. 32, pp. 3110–3112, 2007.

[281] J. P. Hannon, G. T. Trammell, M. Blume, and D. Gibbs, "X-ray resonance exchange scattering," *Phys. Rev. Lett.*, vol. 61, pp. 1245–1248, 1988.

[282] A. Scherz, W. F. Schlotter, K. Chen, R. Rick, J. Stöhr, J. Lüning, S. Eisebitt, C. Günther, F. Radu, W. Eberhardt, O. Hellwig, and I. McNulty, "Phase imaging of magnetic nanostructures using resonant soft X-ray holography," *Phys. Rev. B*, vol. 76, pp. 214410–214414, 2007.

[283] O. Hellwig, S. Eisebitt, W. Eberhardt, W. F. Schlotter, J. Lüning, and J. Stöhr, "Magnetic imaging with soft X-ray spectroholography," *J. Appl. Phys.*, vol. 99, p. 08H307, 2006.

[284] M. Albrecht, G. H. Hu, I. L. Guhr, T. C. Ulbrich, J. Boneberg, P. Leiderer, and G. Schatz, "Magnetic multilayers on nanospheres," *Nature Mater.*, vol. 4, p. 203, 2005.

[285] T. C. Ulbrich, D. Makarov, G. Hu, I. L. Guhr, D. Suess, T. Schrefl, and M. Albrecht, "Magnetization reversal in a novel gradient nanomaterial," *Phys. Rev. Lett.*, vol. 96, pp. 077202-1–077202-4, 2006.

[286] S. Eisebitt, O. Hellwig, C. Günther, W. F. Schlotter, J. Lüning, J. Stöhr, D. Marakov, and M. Albrecht, unpublished.

[287] O. Hellwig, C. Günther, B. Pfau, R. Ramon, W. F. Schlotter, J. Stöhr, W. Eberhardt, and S. Eisebitt, unpublished.

[288] M. Farle, K. Baberschke, U. Stetter, A. Aspelmeier, and F. Gerhardter, "Thickness-dependent Curie temperature of Gd(0001)/W(110) and its dependence on the growth conditions," *Phys. Rev. B*, vol. 47, pp. 11571–11574, 1993.

[289] C. H. Back, C. Würsch, D. Kerkmann, and D. Pescia, "Giant magnetic susceptibility in Fe and Co epitaxial films," *Z. Phys. B*, vol. 96, pp. 1–3, 1994.

[290] O. G. Shpyrko, E. D. Isaacs, J. M. Logan, Y. Feng, G. Aeppli, R. Jaramillo, H. C. Kim, T. F. Rosenbaum, P. Zschack, M. Sprung, S. Narayanan, and A. R. Sandy, "Direct measurement of antiferromagnetic domain fluctuations," *Nature*, vol. 447, pp. 68–71, 2007.

[291] P. Fischer, G. Schütz, G. Schmahl, P. Guttmann, and D. Raasch, "Imaging of magnetic domains with the X-ray microscope at BESSY using X-ray magnetic circular dichroism," *Z. f. Phys. B*, vol. 101, pp. 313–316, 1996.

[292] P. Fischer, T. Eimüller, G. Schütz, P. Guttmann, G. Schmahl, K. Prügl, and G. Bayreuther, "Imaging of magnetic domains by transmission X-ray microscopy," *J. Phys. D: Appl. Physics*, vol. 31, pp. 649–655, Mar. 1998.

[293] T. Eimüller, P. Fischer, G. Schütz, P. Guttmann, G. Schmahl, K. Pruegl, and G. Bayreuther, "Magnetic transmission X-ray microscopy: Imaging magnetic domains via the X-ray magnetic circular dichroism," *J. Alloys Comp.*, vol. 286, pp. 20–25, May 1999.

[294] T. Eimüller, M. Scholz, P. Guttmann, P. Fischer, M. Köhler, G. Bayreuther, G. Schmahl, and G. Schütz, "Magnetization reversal of a multilayered FeGd dot array imaged by transmission X-ray microscopy," *J. Appl. Phys.*, vol. 89, pp. 7162–7164, Jun. 2001.

[295] T. Eimüller, M. Scholz, P. Guttmann, P. Fischer, M. Köhler, G. Bayreuther, G. Schmahl, and G. Schütz, "Undulation instabilities in laterally structured magnetic multilayers," *J. Appl. Phys.*, vol. 91, pp. 7334–7336, May 2002.

[296] W. Meyer-Ilse, G. Denbeaux, L. E. Johnson, W. Bates, A. Lucero, and E. H. Anderson, "The high resolution X-ray microscope XM-1," in *X-Ray Microscopy*, W. Meyer-Ilse, T. Warwick, and D. Attwood, Eds. Melville, NY: American Institute of Physics, 2000, vol. 507, pp. 129–134.

[297] A. L. Pearson, W. Chao, G. Denbeaux, T. Eimuller, P. Fischer, L. Johnson, M. Köhler, C. Larabell, M. Le Gros, D. Yager, and D. Attwood, "XM-1, the high-resolution soft X-ray microscope at the advanced light source," in *Soft X-ray and EUV Imaging Systems*, W. M. Kaiser and R. H. Stulen, Eds. Philadelphia, PA: SPIE, 2000, vol. 4146, pp. 54–59.

[298] P. Fischer, T. Eimüller, G. Schütz, M. Köhler, G. Bayreuther, G. Denbeaux, and D. Attwood, "Study of in-plane magnetic domains with magnetic transmission X-ray microscopy," *J. Appl. Phys.*, vol. 89, pp. 7159–7161, Jun. 2001.

[299] P. Fischer, T. Eimüller, G. Schütz, G. Bayreuther, S. Tsunashima, N. Takagi, G. Denbeaux, and D. Attwood, "Magnetic domains in nanostructured media studied with M-TXM," *J. Synchr. Rad.*, vol. 8, pp. 325–327, 2001.

[300] J. B. Kortright, S.-K. Kim, P. Denbeaux, G. Zeltzer, K. Takano, and E. E. Fullerton, "Soft X-ray small-angle scattering as a sensitive probe of magnetic and charge heterogeneity," *Phys. Rev. B*, vol. 64, pp. 092401–092405, 2001.

[301] P. Fischer, T. Eimüller, G. Schütz, G. Denbeaux, A. Pearson, L. Johnson, D. Attwood, S. Tsunashima, M. Kumazawa, N. Takagi, M. Köhler, and G. Bayreuther, "Element-specific imaging of magnetic domains at 25 nm spatial resolution using soft X-ray microscopy," *Rev. Sci. Instrum.*, vol. 72, pp. 2322–2324, 2001.

[302] T. Eimüller, P. Fischer, M. Köhler, M. Scholz, P. Guttmann, G. Denbeaux, S. Glück, G. Bayreuther, G. Schmahl, D. Attwood, and G. Schütz, "Transmission X-ray microscopy using X-ray magnetic circular dichroism," *Appl. Phys. A*, vol. 73, pp. 697–701, Dec. 2001.

[303] P. Fischer, G. Denbeaux, T. Ono, T. Okuno, T. Eimüller, D. Goll, and G. Schütz, "Study of magnetic domains with magnetic soft X-ray transmission microscopy," *J. Phys. D*, vol. 35, pp. 2391–2397, Oct. 7, 2002.

[304] O. Hellwig, G. P. Denbeaux, J. B. Kortright, and E. E. Fullerton, "X-ray studies of aligned magnetic stripe domains in perpendicular multilayers," *Phys. B*, vol. 336, pp. 136–144, 2001.

[305] M.-Y. Im, P. Fischer, T. Eimüller, G. Denbeaux, and S.-C. Shin, "Magnetization reversal study of CoCrPt alloy thin films on a nanogranular-length scale using magnetic transmission soft X-ray microscopy," *Appl. Phys. Lett.*, vol. 83, pp. 4589–4591, Dec. 2003.

[306] P. Fischer, "Magnetic soft X-ray transmission microscopy," *Curr. Opin. Solid State Mater. Sci.*, vol. 7, pp. 173–179, 2003.

[307] J. E. Davies, O. Hellwig, E. E. Fullerton, G. Denbeaux, J. B. Kortright, and K. Liu, "Magnetization reversal of Co/Pt multilayers: Microscopic origin of high field magnetic irreversibility," *Phys. Rev. B*, vol. 70, pp. 224434–114442, 2004.

[308] G. Meier, R. Eiselt, M. Bolte, M. Barthelmess, T. Eimüller, and P. Fischer, "Comparative study of magnetization reversal in isolated and stray-field coupled microcontacts," *Appl. Phys. Lett.*, vol. 85, pp. 1193–1195, Aug. 2004.

[309] H. Stoll, A. Puzic, B. V. Waeyenberge, P. Fischer, J. Raabe, M. Buess, T. Haug, R. Höllinger, C. H. Back, D. Weiss, and G. Denbeau, "High-resolution imaging of fast magnetization dynamics in magnetic nanostructures," *Appl. Phys. Lett.*, vol. 84, pp. 3328–3330, Apr. 2004.

[310] P. Fischer, D. H. Kim, W. Chao, J. A. Liddle, E. H. Anderson, and D. T. Attwood, "Soft X-ray microscopy of nanomagnetism," *Mater. Today*, vol. 9, pp. 26–33, Jan.–Feb. 2006.

[311] G. Meier, M. Bolte, R. Eiselt, B. Krüger, D.-H. Kim, and P. Fischer, "Direct imaging of stochastic domain-wall motion driven by nanosecond current pulses," *Phys. Rev. Lett.*, vol. 98, pp. 187202-1–187202-4, May 2, 2007.

[312] I. Guhr, S. van Dijken, G. Malinowski, P. Fischer, F. Springer, O. Hellwig, and M. Albrecht, "Magnetization reversal in exchange biased nanocap arrays," *J. Phys. D*, vol. 40, pp. 3005–3010, May 4, 2007.

[313] M. S. Pierce, C. R. Buechler, L. B. Sorensen, S. D. Kevan, E. A. Jagla, J. M. Deutsch, T. Mai, O. Narayan, J. E. Davies, K. Liu, G. T. Zimanyi, H. G. Katzgraber, O. Hellwig, E. E. Fullerton, P. Fischer, and J. B. Kortright, "Disorder-induced magnetic memory: Experiments and theories," *Phys. Rev. B*, vol. 75, pp. 144406–144429, 2007.

[314] S. K. Kim, J. B. Kortright, and S. C. Shin, "Vector magnetization imaging in ferromagnetic thin films using soft X-rays," *Appl. Phys. Lett.*, vol. 78, pp. 2742–2744, 2001.

[315] A. L. D. Kilcoyne, T. Tyliszczak, W. F. Steele, S. Fakra, P. Hitchcock, K. Franck, E. Anderson, B. Harteneck, E. G. Rightor, G. E. Mitchell, A. P. Hitchcock, L. Yang, T. Warwick, and H. Ade, "Interferometer-controlled scanning transmission X-ray microscopes at the Advanced Light Source," *J. Synchrotron Rad.*, vol. 10, pp. 125–136, 2003.

[316] A. Puzic, B. Van Waeyenberge, K. W. Chou, P. Fischer, H. Stoll, G. Schütz, T. Tyliszczak, K. Rott, H. Brückl, G. Reiss, I. Neudecker, T. Haug, M. Buess, and C. H. Back, "Spatially resolved ferromagnetic resonance: Imaging of ferromagnetic eigenmodes," *J. Appl. Phys.*, vol. 97, pp. 10E704-1–10E704-3, May 2005.

[317] Y. Acremann, J. P. Strachan, V. Chembrolu, S. D. Andrews, T. Tyliszczak, J. A. Katine, M. J. Carey, B. M. Clemens, H. C. Siegmann, and J. Stöhr, "Time-resolved imaging of spin transfer switching: Beyond the macrospin concept," *Phys. Rev. Lett.*, vol. 96, pp. 217202-1–217202-4, June 2006.

[318] B. Van Waeyenberge, A. Puzic, H. Stoll, K. W. Chou, T. Tyliszczak, R. Hertel, M. Fähnle, H. Brückl, K. Rott, G. Reiss, I. Neudecker, D. Weiss, C. H. Back, and G. Schütz, "Magnetic vortex core reversal by excitation with short bursts of an alternating field," *Nature*, vol. 444, pp. 461–464, Nov. 2006.

[319] K. W. Chou, A. Puzic, H. Stoll, D. Dolgos, G. Schütz, B. Van Waeyenberge, A. Vansteenkiste, T. Tyliszczak, G. Woltersdorf, and C. H. Back, "Direct observation of the vortex core magnetization and its dynamics," *Appl. Phys. Lett.*, vol. 90, pp. 202505-1–202505-3, May 2007.

[320] K. Kuepper, L. Bischoff, C. Akhmadaliev, J. Fassbender, H. Stoll, K. W. Chou, A. Puzic, K. Fauth, D. Dolgos, G. Schütz, B. Van Waeyenberge, T. Tyliszczak, I. Neudecker, G. Woltersdorf, and C. H. Back, "Vortex dynamics in Permalloy disks with artificial defects: Suppression of the gyrotropic mode," *Appl. Phys. Lett.*, vol. 90, pp. 062506-1–062506-3, 2007.

[321] H. Ohldag, T. Tyliszczak, R. Höhne, D. Spemann, P. Esquinazi, M. Ungureanu, and T. Butz, "π-electron ferromagnetism in metal-free carbon probed by soft X-ray dichroism," *Phys. Rev. Lett.*, vol. 98, pp. 187204-1–187204-4, 2007.

[322] E. Amaladass, B. Ludescher, G. Schütz, T. Tyliszczak, and T. Eimüller, "Size dependence in the magnetization reversal of Fe/Gd multilayers on self assembled arrays of nanospheres," unpublished.

[323] T. Eimüller, B. Niemann, P. Guttmann, P. Fischer, U. Englisch, R. Vatter, C. Wolter, S. Seiffert, G. Schmahl, and G. Schütz, "The magnetic transmission X-ray microscopy project at BESSY II," *J. Phys. IV France*, vol. 104, pp. 91–94, 2003.

[324] W. Chao, B. H. Harteneck, J. A. Liddle, E. H. Anderson, and D. T. Attwood, "Soft X-ray microscopy at a spatial resolution better than 15 nm," *Nature*, vol. 435, pp. 1210–1213, June 2005.

[325] Y. Acremann, V. Chembrolu, J. P. Strachan, T. Tyliszczak, and J. Stöhr, "Software defined photon counting system for time resolved X-ray experiments," *Rev. Sci. Instrum.*, vol. 78, pp. 014702-1–014702-4, 2007.

[326] The XMCD contrast is calculated by the relation $[ln(I^+) - ln(I^-)]/[ln(I^+) + ln(I^-)]$, were I^+ and I^- are the integrated signals from the images obtained with right and left circularly polarized X-ray, respectively.

[327] J. Raabe and F. Luo, *Private Communication.* [Online]. Available: http://www.chemie.uni-erlangen.de/fink/Fink_polluxhome.html

[328] G. Schönhense, H. J. Elmers, S. A. Nepijko, and C. M. Schneider, "Time-resolved photoemission electron microscopy," *Adv. Imag. Electron Phys.*, vol. 142, pp. 159–323, 2006.

[329] A. Oelsner, A. Krasyuk, S. A. Nepijko, C. M. Schneider, and G. Schönhense, "Spatially resolved observation of dynamics in electrical and magnetic field distributions by means of a delayline detector and PEEM," *J. Electron Spectr. Rel. Phen.*, vol. 144–147, pp. 771–776, 2005.

[330] U. D. Keil, H. J. Gerritsen, J. E. M. Haverkort, and J. H. Wolter, "Generation of ultrashort electrical pulses with variable pulse widths," *Appl. Phys. Lett.*, vol. 66, pp. 1629–1631, 1995.

[331] J. Vogel, W. Kuch, M. Bonfim, J. Camarero, Y. Pennec, F. Offi, K. Fukumoto, J. Kirschner, A. Fontaine, and S. Pizzini, "Time-resolved magnetic domain imaging by X-ray photoemission electron microscopy," *Appl. Phys. Lett.*, vol. 82, pp. 2299-1–2299-3, 2003.

[332] S.-B. Choe, Y. Acremann, A. Scholl, A. Bauer, A. Doran, J. Stöhr, and H. A. Padmore, "Vortex core-driven magnetization dynamics," *Science*, vol. 304, pp. 420–422, 2004.

[333] C. M. Schneider, A. Kuksov, A. Krasyuk, A. Oelsner, D. Neeb, S. A. Nepijko, G. Schönhense, J. Morais, I. Mönch, R. Kaltofen, C. D. Nadaï, and N. B. Brookes, "Incoherent magnetization rotation observed in subnanosecond time-resolving X-ray photoemission electron microscopy," *Appl. Phys. Lett.*, vol. 85, pp. 2562-1–2562-3, 2004.

[334] J. Raabe, C. Quitmann, C. H. Back, F. Nolting, S. Johnson, and C. Buehler, "Quantitative analysis of magnetic excitations in landau flux-closure structures using synchrotron-radiation microscopy," *Phys. Rev. Lett.*, vol. 94, pp. 217204-1–217204-4, 2005.

[335] A. Krasyuk, F. Wegelin, S. A. Nepijko, H. J. Elmers, G. Schönhense, M. Bolte, and C. M. Schneider, "Self-trapping of magnetic oscillation modes in Landau flux-closure structures," *Phys. Rev. Lett.*, vol. 95, pp. 207201-1–207201-4, 2005.

[336] K. Fukumoto, W. Kuch, J. Vogel, F. Romanens, S. Pizzini, J. Camarero, M. Bonfim, and J. Kirschner, "Dynamics of magnetic domain wall motion after nucleation: Dependence on the wall energy," *Phys. Rev. Lett.*, vol. 96, pp. 097204-1–097204-4, 2006.

[337] K. Kuepper, M. Buess, J. Raabe, C. Quitmann, and J. Fassbender, "Dynamic vortex-antivortex interaction in a single cross-tie wall," *Phys. Rev. Lett.*, vol. 99, pp. 167202-1–167202-4, 2007.

[338] R. P. Cowburn and D. A. Allwood, "Multiple Layer Magnetic Logic Memory Device," U.K. patent GB2.430.318A, 2007.

[339] S. S. P. Parkin, "Shiftable Magnetic Shift Register and Method Using the Same," U.S. patent 6.834.005B1, 2004.

[340] M. Redjdal, J. Giusti, M. F. Ruane, and F. B. Humphrey, "Thickness dependent wall mobility in thin permalloy films," *J. Appl. Phys.*, vol. 91, pp. 7547–7549, 2002.

[341] S. Konishi, S. Yamada, and T. Kusuda, "Domain-wall velocity, mobility, and mean-free-path in permalloy films," *IEEE Trans. Magn.*, vol. 7, pp. 722–724, 1971.

[342] N. L. Schryer and L. R. Walker, "The motion of 180 ° domain walls in uniform dc magnetic fields," *J. Appl. Phys.*, vol. 45, pp. 5406–5421, 1974.

[343] J. Miltat, G. Albuquerque, and A. Thiaville, "An introduction to micromagnetics in the dynamic regime," in *Spin Dynamics in Confined Magnetic Structures Vol. 1*, B. Hillebrands and K. Ounadjela, Eds. New York: Springer-Verlag, 2002.

[344] W. K. Hiebert, A. Stankiewicz, and M. R. Freeman, "Direct observation of magnetic relaxation in a small permalloy disk by time-resolved scanning kerr microscopy," *Phys. Rev. Lett.*, vol. 79, pp. 1134–1137, 1997.

[345] F. Wegelin, D. Valdaitsev, A. Krasyuk, S. A. Nepijko, G. Schönhense, H. J. Elmers, I. Krug, and C. M. Schneider, "Magnetization dynamics in microscopic spin-valve elements: Shortcomings of the macrospin picture," *Phys. Rev. B*, vol. 76, pp. 134410-1–134410-4, 2007.

[346] E. Feldtkeller and H. Thomas, "Struktur und Energie von Blochlinien in dünnen ferromagnetischen Schichten," *Phys. Kondens. Mater.*, vol. 4, pp. 8–14, 1965.

[347] A. Wachowiak, J. Wiebe, M. Bode, O. Pietzsch, M. Morgenstern, and R. Wiesendanger, "Direct observation of internal spin structure of magnetic vortex cores," *Science*, vol. 298, pp. 577–580, 2002.

[348] A. A. Thiele, "Steady-state motion of magnetic domains," *Phys. Rev. Lett.*, vol. 30, pp. 230–233, 1973.

[349] M. Buess, R. Höllinger, T. Haug, K. Perzlmaier, U. Krey, D. Pescia, M. R. Scheinfein, D. Weiss, and C. H. Back, "Fourier transform imaging of spin vortex eigenmodes," *Phys. Rev. Lett.*, vol. 93, pp. 077207-1–077207-4, 2004.

[350] R. Hertel and C. M. Schneider, "Exchange explosions: Magnetization dynamics during vortex-antivortex annihilation," *Phys. Rev. Lett.*, vol. 97, pp. 177202-1–177202-4, 2006.

[351] R. Hertel, S. Gliga, M. Fähnle, and C. M. Schneider, "Ultrafast nanomagnetic toggle switching of vortex cores," *Phys. Rev. Lett.*, vol. 98, pp. 117201-1–117201-4, 2007.

[352] S. Gliga, R. Hertel, and C. M. Schneider, "Flipping magnetic vortex cores on the picosecond time scale," *Phys. B*, vol. 403, pp. 334–337, 2008.

[353] Y. Liu, S. Gliga, R. Hertel, and C. M. Schneider, "Current-induced magnetic vortex core switching in a Permalloy nanodisk," *Appl. Phys. Lett.*, vol. 91, pp. 112501-1–112501-4, 2007.

[354] S.-K. Kim, K.-S. Lee, Y.-S. Yu, and Y.-S. Choi, "Reliable low-power control of ultrafast vortex-core switching with the selectivity in an array of vortex states by in-plane circular-rotational magnetic fields and spin-polarized currents," *Appl. Phys. Lett.*, vol. 92, pp. 022509-1–022509-4, 2008.

[355] T. Gerrits, H. A. M. van den Berg, J. Hohlfeld, L. Bär, and T. Rasing, "Ultrafast precessional magnetization reversal by picosecond magnetic field pulse shaping," *Nature*, vol. 418, pp. 509–512, 2002.

[356] I. Tudosa, C. Stamm, A. B. Kashuba, F. King, H. C. Siegmann, J. Stöhr, G. Ju, B. Lu, and D. Weller, "The ultimate speed of magnetic switching in granular recording media," *Nature*, vol. 428, pp. 831–833, 2004.

[357] G. P. Zhang and W. Hübner, "Laser-induced ultrafast demagnetization in ferromagnetic metals," *Phys. Rev. Lett.*, vol. 85, pp. 3025–3028, 2000.

[358] B. Koopmans, J. J. M. Ruigrok, F. D. Longa, and W. J. M. de Jonge, "Unifying ultrafast magnetization dynamics," *Phys. Rev. Lett.*, vol. 95, pp. 267207-1–267207-4, 2005.

[359] E. Beaurepaire, J.-C. Merle, A. Daunoise, and J.-Y. Bigot, "Ultrafast spin dynamics in ferromagnetic nickel," *Phys. Rev. Lett.*, vol. 76, pp. 4250–4253, 1996.

[360] A. Vaterlaus, T. Beutler, D. Guarisco, M. Lutz, and F. Meier, "Spin-lattice relaxation in ferromagnets studied by time-resolved spin-polarized photoemission," *Phys. Rev. B*, vol. 46, pp. 5280–5286, 1992.

[361] A. Einstein and W. J. de Haas, "Experimenteller Nachweis der Ampereschen Molekularströme," *Verhandl. Deut. Phys. Ges.*, vol. 17, pp. 152–170, 1915.

[362] W. Hübner and K. H. Bennemann, "Simple theory for spin-lattice relaxation in metallic rare-earth ferromagnets," *Phys. Rev. B*, vol. 53, pp. 3422–3427, 1996.

[363] A. Scholl, L. Baumgarten, R. Jacquemin, and W. Eberhardt, "Ultrafast spin dynamics of ferromagnetic thin films observed by fs spin-resolved two-photon photoemission," *Phys. Rev. Lett.*, vol. 79, pp. 5146–5149, 1997.

[364] H.-S. Rhie, H. A. Dürr, and W. Eberhardt, "Femtosecond electron and spin dynamics in Ni/W(110) films," *Phys. Rev. Lett.*, vol. 90, pp. 247201-1–247201-4, 2003.

[365] B. Koopmans, M. van Kampen, J. T. Kohlhepp, and W. J. M. de Jonge, "Ultrafast magneto-optics in nickel: Magnetism or optics?," *Phys. Rev. Lett.*, vol. 85, pp. 844–847, 2000.

[366] C. Stamm, T. Kachel, N. Pontius, R. Mitzner, T. Quast, K. Holldack, S. Khan, C. Lupulescu, E. F. Aziz, M. Wietstruk, H. A. Dürr, and W. Eberhardt, "Femtosecond modification of electron localization and transfer of angular momentum in nickel," *Nat. Mater.*, vol. 6, pp. 740–743, 2007.

[367] K. Holldack, S. Khan, R. Mitzner, and T. Quast, "Characterization of laser-electron interaction at the BESSY II femtoslicing source," *Phys. Rev. ST Accel. Beams*, vol. 8, p. 040704-7, 2005.

[368] K. Holldack, S. Khan, R. Mitzner, and T. Quast, "Femtosecond terahertz radiation from femtoslicing at BESSY," *Phys. Rev. Lett.*, vol. 96, pp. 054801-1–054801-4, 2006.

[369] R. W. Schoenlein, S. Chattopadhyay, H. H. W. Chong, T. E. Glover, P. A. Heimann, C. V. Shank, A. A. Zholents, and M. S. Zolotorev, "Generation of femtosecond pulses of synchrotron radiation," *Science*, vol. 287, pp. 2237–2240, 2000.

[370] P. Carra, B. T. Thole, M. Altarelli, and X. Wang, "X-ray circular dichroism and local magnetic fields," *Phys. Rev. Lett.*, vol. 70, pp. 694–697, 1993.

[371] J. Stöhr and H. König, "Determination of spin- and orbital-moment anisotropies in transition metals by angle-dependent X-ray magnetic circular dichroism," *Phys. Rev. Lett.*, vol. 75, pp. 3748–3751, 1995.

[372] S.-K. Kim and J. B. Kortright, "Modified magnetism at Co/Pd interfaces resolved with X-ray standing waves," *Phys. Rev. Lett.*, vol. 86, pp. 1347–1350, 2001.

[373] B. C. Sell, S. B. Ritchey, S. H. Yang, S. S. P. Parkin, M. Watanabe, B. S. Mun, L. Plucinski, N. Mannella, A. Nambu, J. Guo, M. W. West, F. Salmassi, J. B. Kortright, and C. S. Fadley, "Determination of buried interface composition and magnetism profiles using standing-wave excited soft X-ray emission and inelastic scattering," *J. Appl. Phys.*, vol. 103, pp. 083515.1–083515.8, 2008.

[374] T. Schmidt, U. Groh, R. Fink, E. Umbach, O. Schaff, W. Engel, B. Richter, H. Kuhlenbeck, R. Schlögl, H.-J. Freund, A. M. Bradshaw, D. Preikszas, P. Hartel, R. Spehr, H. Rose, G. Lilienkamp, E. Bauer, and G. Benner, "XPEEM with energy-filtering: Advantages and first results from the SMART project," *Surf. Rev. Lett.*, vol. 9, pp. 223–232, 2002.

[375] J. Feng, E. Forest, A. A. MacDowell, M. Marcus, H. Padmore, S. Raoux, D. Robin, A. Scholl, R. Schlueter, P. Schmid, S. J. hr, W. Wan, D. H. Wei, and Y. Wu, "An X-ray photoemission electron microscope using an electron mirror aberration corrector for the study of complex materials," *J. Phys.: Condens. Matt.*, vol. 17, pp. S1339–S1350, 2005.

[376] T. Matsushima, T. Okuda, T. Eguchi, M. Ono, A. Harasawa, T. Wakita, A. Kataoka, M. Hamada, A. Kamoshida, Y. Hasegawa, and T. Kinoshita, "Development and trial measurement of synchrotron-radiation-light-illuminated scanning tunneling microscope," *Rev. Sci. Instrum.*, vol. 75, pp. 2149–2153, 2004.

[377] R. W. Schoenlein, S. Chattopadhyay, H. H. W. Chong, T. E. Glover, P. A. Heimann, C. V. Shank, A. A. Zholents, and M. S. Zolotorev, "Generation of femtosecond pulses of synchrotron radiation," *Science*, vol. 287, pp. 2237–2240, 2000.